PSFC/RR-08-1

Propulsion Mechanisms in a Helicon Plasma Thruster

N. Sinenian

Plasma Science and Fusion Center
Massachusetts Institute of Technology
Cambridge MA 02139 USA

This work was supported by MIT-AFRL/ERC Grant No. RS060213. Reproduction, translation, publication, use and disposal, in whole or in part, by or for the United States government is permitted.

Propulsion Mechanisms in a Helicon Plasma Thruster

by

Nareg Sinenian

B.S. Physics (2005)
University of California, San Diego

Submitted to the Department of Nuclear Science and Engineering
and the Department of Electrical Engineering and Computer Science
in partial fulfillment of the requirements for the degrees of

MASTER OF SCIENCE IN NUCLEAR SCIENCE & ENGINEERING

and

MASTER OF SCIENCE IN ELECTRICAL ENGINEERING

at the

MASSACHUSETTS INSTITUTE OF TECHNOLOGY

February 2008

Author .....
Department of Nuclear Science and Engineering
and the Department of Electrical Engineering and Computer Science
February, 2008

Certified by .....
Ronald R. Parker
Professor of Nuclear Science and Engineering
Professor of Electrical Engineering and Computer Science
Thesis Supervisor

Certified by .....
Oleg V. Batishchev
Principal Research Scientist, Department of Aeronautics and Astronautics
Thesis Supervisor

Accepted by .....
Terry P. Orlando
Chairman, Department Committee on Graduate Students (EECS)

Accepted by .....
Jacquelyn Yanch
Chairman, Department Committee on Graduate Students (NSE)

Propulsion Mechanisms in a Helicon Plasma Thruster

by

Nareg Sinenian

Submitted to the Department of Nuclear Science and Engineering
and the Department of Electrical Engineering and Computer Science
on February, 2008, in partial fulfillment of the
requirements for the degrees of
MASTER OF SCIENCE IN NUCLEAR SCIENCE & ENGINEERING
and
MASTER OF SCIENCE IN ELECTRICAL ENGINEERING

Abstract

Electric thrusters offer an attractive option for various in-space propulsion tasks due to their high thrust efficiencies. The performance characteristics of a compact electric thruster utilizing a helicon plasma source is investigated with the goal of identifying potential thrust mechanisms. Performance characteristics such as thrust, specific impulse, ion cost and thrust efficiency are discussed and related to plasma parameters. The design and fabrication of a prototype compact helicon thruster is presented, including design of a radio-frequency power delivery system, electromagnets and a propellant flow system. The design of plasma diagnostics and associated measurement techniques are discussed including a retarding potential analyzer, mach probes and langmuir probes. These diagnostics are used to measure plasma properties such as electron temperature, plasma density, and ion flow velocities. Thruster performance characteristics are then derived from these measurement results. Significant ion acceleration is demonstrated in both Argon and Nitrogen plasmas and potential mechanisms for this are discussed.

Thesis Supervisor: Ronald R. Parker
Title: Professor of Nuclear Science and Engineering
Professor of Electrical Engineering and Computer Science

Thesis Supervisor: Oleg V. Batishchev
Title: Principal Research Scientist, Department of Aeronautics and Astronautics

Acknowledgments

The author would like to thank Dr. Oleg Batishchev for support and for his leadership throughout the project and Prof. Ron Parker for his general guidance, advice and valuable discussions throughout the endeavor. The author is also grateful to Prof. Manuel Martinez-Sanchez and Prof. Paulo Lozano for helpful suggestions and for allowing use of their facilities for experimentation, to Prof. Ian Hutchinson and Dr. Brian Labombard of the Plasma Science and Fusion Center for imparting their knowledge and insight with regard to probe physics and to Dr. Murat Celik for assistance and guidance in acquiring and understanding data.

This work was supported by MIT-AFRL/ERC/Edwards Contract # RS060213 "Experimental Study of the Mini-Helicon Thruster"

Contents

List of Figures

C-3 Propellant flow control. The propellant gas flow may be selected (in standard cubic centimeters per minute, or sccm) while the actual flow rate is monitored in real time. The type of gas used may be specified to apply a correction factor to the flow control.106

List of Tables

Chapter 1

Introduction

Electric rockets[1] offer several advantages over conventional chemical rocket engines for in-space propulsion, including higher thrust efficiency, lower propellant mass for any given mission, and larger plume exhaust velocities[2]. Several advanced electric propulsion concepts are currently in development, and this thesis investigates performance characteristics of a compact electric thruster with the goal of identifying which mechanisms might be responsible for those characteristics.

1.1 Helicon Waves and Electric Propulsion

The compact helicon plasma thruster under consideration utilizes an antenna to weakly ionize injected propellant gas and then to excite helicon waves within the created plasma. An externally applied axial magnetic field serves to confine plasma ions and allow for helicon wave propagation which in turn is responsible for efficient full ionization of the propellant gas and energy deposition in the form of electron heating. The high density plasma is then accelerated into a convergent plasma jet and ejected from the thruster through a diverging magnetic field, known as a magnetic nozzle. The use of helicon waves to fully ionize the propellant is desirable as helicon plasma sources have been shown to produce high-density uniform plasmas efficiently[3]. Furthermore, it will be shown in the following sections that compact sources are capable of producing higher density plasmas. Knowledge of helicon wave physics and thruster performance metrics as they relate to plasma parameters is essential to understanding and optimizing thruster operation; that is the focus of

[1] The terms "rocket" and "thruster" are used interchangeably

the ensueing sections. Discussion of thruster design and implementation details are reserved for Chapter 2. For the purposes of the following sections it is sufficient to state that the plasma geometry of interest is cylindrical with neutral gas injected at one end, ionized within the cylinder, confined radially by a magnetic field and finally accelerated outward axially.

The helicon wave dispersion relationship obtained in the following section relates plasma parameters to various physical parameters, including the external applied magnetic flux density, the plasma radius and the specific wave modes excited within the plasma column. Of these physical parameters, the first indicates the field strength and geometry of the magnetic field source for a particular design, the second sets the geometry of the neutral gas injector while the third dictates the design of the optimal antenna. Although the wave dispersion relationship captures essential helicon physics and allows for a first-order thruster design based on desired plasma parameters, the presence of secondary effects with regard to helicon wave propagation may either enhance or deteriorate plasma performance and will be discussed to some extent. The end result is an efficient plasma source with known plasma characteristics; these must be related to important rocket characteristics such as thrust and specific impulse. The plasma mechanisms which convert electron energy into axial ion acceleration thereby producing thrust must be considered. The design must be optimized for these parameters if a high-performance helicon plasma rocket is to be viable. In addition to thrust and specific impulse there exist several other electric rocket performance measures which must be considered. A brief summary of pertinent rocket performance metrics and their relation to plasma parameters is presented in what follows.

Thrust

The thrust force generated by a rocket occurs as a result of the conservation of linear momentum. This condition may be expressed as

$$\mathbf{F_{ext}} = \frac{d}{dt}(m\mathbf{v}) \tag{1.1}$$

where $\mathbf{F_{ext}}$ is any external force such as gravity in the case of a vertically ascending rocket. For the case of in-space propulsion (whether chemical or electric) gravitational forces may be neglected and the rocket equation is then expanded to obtain the total thrust, $\mathbf{T}$,

$$\mathbf{T} = \dot{m}\mathbf{v} + (\mathbf{p_e} - \mathbf{p_a}) \cdot \mathbf{A_n} = \dot{m}\mathbf{c} \tag{1.2}$$

where $\dot{m}$ is the propellant mass flow rate, p_e the fluid pressure at the rocket nozzle's exit, p_a the ambient pressure, A_e the nozzle area, and $\mathbf{c}$ the *effective exhaust velocity*, as measured downstream of the nozzle where the local pressure is equal to that of the ambient. The first term in 1.2 is the *momentum thrust* obtained directly from the expansion of the right hand side of equation 1.1 and the second term is the *pressure thrust* or the thrust produced as a result of the pressure difference between the rocket nozzle's exit and the ambient[4]. In the case of the helicon plasma rocket under consideration, the dominant contribution to the momentum thrust term is the motion of ions; $\dot{m}$ is the propellant mass flow rate for the ion species in question and $\mathbf{v}$ is the plasma jet speed or the exhaust velocity of ions at the nozzle's exit. It is assumed that the product $\dot{m}\mathbf{v}$ is negligible for electrons and neutrals; the former's mass is insignificant compared to that of the propellant ion species utilized and the latter's velocity is assumed to be thermal (fast neutrals as a result of charge-exchange are presently not considered). The pessure thrust term in a helicon plasma rocket is small in comparison to the momentum term and may be neglected in most cases. The pressure at the nozzle exhaust may be expressed in terms of the plasma temperature and density using the ideal gas law ($p_e = nKT$), and the ambient pressure is that of a high vacuum environment ($p_a \approx 1 \times 10^{-5}$ Torr). Note that equation 1.2 is a vector equation and as a consequence in typical axisymmetric electric thrusters radial components of $\mathbf{c}$ will not give rise to thrust and will lead to less efficient operation; a collimated plasma jet is therefore desirable as it is generally indicative of efficient operation.

Specific impulse

Specific impulse (I_s) is defined as the jet speed of the propellant gas normalized to the gravitational acceleration at sealevel; it is a measure of the specific kinetic energy of the plasma jet in units of seconds. Assuming negligible pressure thrust, the relation between the specific impulse and thrust is given as[4]

$$P/T = \frac{1}{2}\dot{m}c^2/\dot{m}c = \frac{1}{2}g_0 I_s \tag{1.3}$$

where P/T is the *jet* power-to-thrust ratio, $\dot{m}$ the propellant mass flow rate, g_0 the gravitational acceleration at sealevel and c the plasma jet speed. For a fixed input power specific impulse and thrust are inversely proportional. Typical values of I_s for chemical rockets are in the range of a few hundred seconds, and for electric propulsion a few thousand seconds. The specific impulse will generally depend on the ion species; for a fixed plasma power input and plasma density, lighter species will have a greater exhaust velocity.

Ionization fraction and ionization cost

Ionization fraction (α_i) is the ratio of the plasma density to the sum of the plasma and neutral densities; it is a measure of the effectiveness of the ionizing agent. Large electric fields across the antenna initially ionize the neutral gas to a small degree. Bulk ionziation of the plasma occurs due to fast primary electrons, which undergo several elastic collisions before they ionize a neutral atom[3]. The amount of energy needed to ionize a single atom is therefore effectively greater than the ionization energy of the propellant species; this quantity is referred to as the ionization cost per ion (α_c). The ionization cost may be expressed as

$$\alpha_c = \frac{P_{in}\eta_{rf}\eta_a}{eA_p\Gamma_i} \tag{1.4}$$

where P_{in} is the input power, η_{rf} the efficiency of the RF generator, η_a the antenna coupling efficiency, $\Gamma_i = n_i v_i$ the ion flux, A_p the cross sectional area of the plasma where Γ_i is measured and α_c the ionization cost per ion in units of electron volts. Note that $eA_p\Gamma_i$ is just the ion current and the above expression is hence a balance between the input power (after antenna and RF losses are accounted for) and the ion beam power. The ion flux in the above expression is the total flux of ions as they are born; if one were to consider a control volume around the ionization region then the ratio of the number of ions leaving that volume to the surface area of the volume would be Γ_i. The equation of continuity may be used to express the ion flux in terms of the input mass flow rate of neutrals; it is written as

$$\frac{\partial n_i}{\partial t} + \nabla \cdot \Gamma_i = S \tag{1.5}$$

In steady state the density will not vary in time and the first term may be neglected. Since the ion

flux is strictly outward (i.e. leaving the control volume), $\nabla \cdot \mathbf{\Gamma_i}$ must be positive, and this outward flux is balanced by the ion source term on the right hand side of 1.5. The collision frequency for ionizing electron-neutral encounters determines the magntiude of the source term, making that term proportional to density; with constant density in steady state it is assumed that S is constant with a value of

$$S = \frac{\dot{m}\alpha_i}{m_i l_i A_i} \tag{1.6}$$

where l_i and A_i are the respective length and area of the ionization region, m_i the ion mass and the other symbols have their usual meanings. Integrating both sides of 1.5 over the control volume gives

$$\int_V \nabla \cdot \mathbf{\Gamma_i} dV = \int_S \mathbf{\Gamma_i} \cdot \mathbf{dA} = \int_V S dV \tag{1.7}$$

where the first equality holds true by virtue of Gauss' Law. Evaluation of the above integrals leads to the expression

$$\Gamma_i = \frac{\dot{m}\alpha_i}{m_i A_i} \tag{1.8}$$

The above expression is just a statement of the conservation of mass; the particles leaving the control volume which defines the ionization region (left hand side) must equal the particles born in that region (right hand side). The ion flux downstream of the ionization region will be anisotropic due to the magnetic field and may be broken up into components parallel and perpendicular to the field. It is then useful to define a *utilization efficiency*

$$\eta_u \equiv \Gamma_{i\parallel} / \left(\frac{\dot{m}}{m_i A_i} \right) \tag{1.9}$$

where $\Gamma_{i\parallel}$ is the axial ion flux leaving the thruster. This allows 1.4 to be rewritten with the use of 1.8 and 1.9 as

$$\alpha_c = \frac{P_{in}\eta_{rf}\eta_a\eta_u}{eA_p\alpha_i\Gamma_{i\parallel}} \tag{1.10}$$

The above formulation is convenient as it is often easier to experimentally measure the ionization

fraction as well the axial ion flux; the latter is the ion flux out of the thruster, which is readily accesible.

Utilization efficiency and nozzle efficiency

Utilization efficiency (η_u) is defined by 1.9 as the ratio of axial ion flux at the nozzle to the total particle flux at the inlet. The thruster topology under consideration is unique from its electrostatic counterparts in that a magnetic field is used to confine ions radially. Accordingly η_u is defined here to not only penalize for neutral flux at the nozzle (unspent fuel) but for radial ion flux (wasted fuel) as well. Utilization efficiency is sometimes referred to as fuel efficiency. Nozzle efficiency (η_n) is the fraction of the propellant flow ($\dot{m}$) which detaches from the magnetic nozzle. Since the plasma jet consists of both ions and electrons a small fraction of the ionized propellant will recombine in the plume region and escape at a rate determined by the cross-section for recombination. The larger fraction of the jet however must stretch the magnetic field lines along the direction of flow in order to detach. Ions which fail to detach will follow closed magnetic field lines and contribute no net momentum change to the system; they consequently generate no useful thrust. Plasma jet power and thrust are both directly proportional to $\dot{m}$ and are directly affected by nozzle efficiency.

Efficiency

The total input power to the thruster is lost to several plasma mechanisms including ionization and radiation as a result of recombination and excitation. The RF power amplifier and antenna combination as well as the magnets (if electromagnets or superconducting magnets are used) will have an efficiency and will dissipate some fraction of the input power as well. The remainder of the power is then available for the plasma jet to generate useful thrust. The overall efficiency may be expressed as the ratio of the jet power to the input power

$$\eta = \frac{\frac{1}{2}\dot{m}c^2}{P_{in}} = \frac{T^2/2\dot{m}}{P_{in}} \tag{1.11}$$

The jet power is of course being used a measure of useful work and thus must use the component of **c** normal to the direction of thrust, per the aforementioned discussion regarding plume or plasma jet collimation. The jet power may be expressed in terms of the total input power; this results in

an overall efficiency given by

$$\eta = \eta_{rf}\eta_a\eta_n\frac{m_i c^2}{\alpha_c} \tag{1.12}$$

This expression is somewhat misleading; a larger propellant mass (m_i) does not necessarily lead to higher efficiency as the ionization cost (α_c) will necessarily grow accordingly; the formulation is nevertheless useful as the efficiency is expressed in terms of simple measureable quantities. Efficiency may thus be determined by knoweldge of the input power and thrust per 1.11, or input power, ion flux and I_{sp} per 1.12. The aforementioned performance parameters are clearly not independent although they are convenient metrics for various aspects of space mission design and analysis. From the stand point of plasma physics, many of these parameters may be deduced by measuring the plasma jet ion speed, density, and electron temperature for a given input power, propellant flow rate and magnetic field strength; that is the primary focus of this thesis.

The rocket concept under consideration has several advantages over existing and in some cases relatively well adopted in-space propulsion topologies. The plasma jet is inherently neutral - ions and electrons are accelerated through a magnetic nozzle preventing space-charge buildup on the thruster. Ion engines and hall-effect thrusters accelerate ions exclusively and require an external cathode for beam neutralization; electrodes in direct contact with the working plasma are susceptible to erosion and in general limit the lifetimes of those engines. Moreover, magnetic confinement of the plasma and proper neutral gas injector design in a helicon thruster minimize wall losses and surface erosion, allowing for increased efficiency and lifetimes.

Once an experimental configuration has been found to produce the desired thruster characteristics at a level of efficiency adequate for space propulsion applications, several engineering issues must be addressed - the design of thermal systems, power electronics, magnets, and electromagnetic interference (EMI) shielding. Of particular interest is radio-frequency (RF) power generation and control of the dynamic plasma load, which adds to the complexity of the thruster's power processing unit (PPU).

1.2 Helicon Wave Physics

Helicon waves are cylindrically bounded low-frequency whistler waves and thus propagate between the ion cyclotron (ω_{ci}) and electron cyclotron (ω_{ce}) frequencies. The wave may have left or right circular polarization and propagates parallel or anti-parallel to an external applied magnetic field. Several treatments of helicon waves may be found in literature[5, 6, 7, 8, 9, 10]; this section presents a literature review of the physics of helicon wave propagation in the physical limits which are relevant to the application under consideration.

1.2.1 Dispersion Relation

The helicon wave dispersion relationship is derived from first principles in the most direct manner in this section. The relevant physical configuration is that of a bound cylindrical plasma with an externally applied axial magnetic field $\mathbf{B_0}$ along the $\hat{\mathbf{z}}$ direction; equilibrium quantities are hereon denoted with a subscript (e.g. $\mathbf{B_0}$). The presence of the equilibrium magnetic field enables the helicon wave (hereon denoted the H-wave with propagation frequency ω_H) to propagate deep into the plasma column; this is in contrast to a purely capacitively or inductively coupled discharge, where the skin effect prevents electromagnetic waves from penetrating into the core of the plasma. Wave perturbed quantities vary as $\exp[\mathrm{i}(m\theta + kz - \omega t)]$ in a cylindrical geometry and with the equilibrium magnetic field, Maxwell's equations take on the following form

$$\nabla \cdot \mathbf{B} = 0 \tag{1.13}$$

$$\nabla \times \mathbf{E} = -\frac{\partial \mathbf{B}}{\partial t} = i\omega \mathbf{B} \tag{1.14}$$

$$\nabla \times \mathbf{B} = \mu_0 \mathbf{j} + \mu_0 \epsilon_0 \frac{\partial \mathbf{E}}{\partial t} = \mu_0 \mathbf{j} - i\mu_0 \omega \epsilon_0 \mathbf{E} \tag{1.15}$$

Ion motions are momentarily neglected; the plasma current is then given by

$$\mathbf{j} = -e n_0 \mathbf{v_e} \tag{1.16}$$

where plasma quasineutrality implies that $n_0 = n_e = n_i$. The electron velocity in 1.16 is found using the electron fluid equation

$$-in_0\omega m_e\mathbf{v_e} = -en_0(\mathbf{E}+\mathbf{v_e}\times\mathbf{B_0}) - n_0m_e\nu(\mathbf{v_e}-\mathbf{v_i}) + \nabla\mathbf{p} + \nabla\cdot\pi \tag{1.17}$$

The collision term $-n_0m_e\nu(\mathbf{v_e}-\mathbf{v_i})$ is dropped; it may be accounted for at any time by replacing the electron mass with with an effective mass $m_e^* = m_e(1+i\nu/\omega)$ in the usual way. The assumption will be made *a priori* that the electron larmor radius is much smaller than the transverse wavelength, and that the electron viscosity term $\nabla\cdot\pi$ may be consequently neglected. The nonlinear pressure term $\nabla\mathbf{p}$ in equation 1.17 can be expanded using the ideal gas law

$$\nabla\mathbf{p} = \nabla nKT_e = \nabla[(n_0+n)(KT_{e0}+KT_e)] \tag{1.18}$$

KT_e is of order $5eV$ while typical antenna wave potentials are well in excess of 100V; then KT_e is small in comparison to the eE term in 1.17. The pressure term is negligible in the limit of a cold plasma. The electron fluid equation simplifies to

$$-in_0\omega m_e\mathbf{v_e} = -en_0(\mathbf{E}+\mathbf{v_e}\times\mathbf{B_0}) \tag{1.19}$$

which is then combined with equation 1.16 to yield

$$\mathbf{E} = -\frac{B_0}{en_0}\left(i\frac{\omega}{\omega_{ce}}\mathbf{j} - \mathbf{j}\times\hat{\mathbf{z}}\right) \tag{1.20}$$

The above result may be alternatively obtained using the cold plasma dielectric tensor[5]. In the high-density plasma modes of interest capacitive coupling is weak and the displacement current in 1.15 may be neglected[11]. Maxwell's equations and 1.20 are then combined to obtain a vector equation for $\mathbf{B}$

$$i\omega\mathbf{B} = -\frac{B_0}{en_0\mu_0}\left[\frac{i\omega}{\omega_{ce}}\nabla\times(\nabla\times\mathbf{B}) - \nabla\times\{(\nabla\times\mathbf{B})\times\hat{\mathbf{z}}\}\right] \tag{1.21}$$

Application of the following vector identity and $\nabla\cdot\mathbf{B}=0$ simplifies the last term in 1.21 to

$$\begin{aligned}\nabla\times\{(\nabla\times\mathbf{B})\times\hat{\mathbf{z}}\} &= (\nabla\times\mathbf{B})(\nabla\cdot\hat{\mathbf{z}}) - \hat{\mathbf{z}}(\nabla\cdot\nabla\times\mathbf{B})) + (\hat{\mathbf{z}}\cdot\nabla)(\nabla\times\mathbf{B}) - \{(\nabla\times\mathbf{B})\cdot\nabla\}\hat{\mathbf{z}} \\ &= (\hat{\mathbf{z}}\cdot\nabla)(\nabla\times\mathbf{B}) \\ &= -ik\nabla\times\mathbf{B}\end{aligned} \tag{1.22}$$

the vector equation for $\mathbf{B}$ may then be written as

$$\frac{\omega}{\omega_{ce}}\nabla\times\nabla\times\mathbf{B}-k\nabla\times\mathbf{B}+\frac{en_0\mu_0\omega}{B_0}\mathbf{B}=0 \tag{1.23}$$

which can be factored into[12]

$$(\beta_1-\nabla\times)(\beta_2-\nabla\times)\mathbf{B}=0 \tag{1.24}$$

with the solution $\mathbf{B}=\mathbf{B_1}+\mathbf{B_2}$ where $\mathbf{B_1}$ and $\mathbf{B_2}$ are given by the zeroes of 1.24 above

$$\nabla\times\mathbf{B_1}=\beta_1\mathbf{B_1} \tag{1.25}$$

$$\nabla\times\mathbf{B_2}=\beta_2\mathbf{B_2} \tag{1.26}$$

The curl of both sides of the above expressions and $\nabla\cdot\mathbf{B}=0$ results in a pair of Helmholtz equations

$$\nabla^2\mathbf{B_1}+\beta_1^2\mathbf{B_1}=0 \tag{1.27}$$

$$\nabla^2\mathbf{B_2}+\beta_2^2\mathbf{B_2}=0 \tag{1.28}$$

The eigenvalues β_1 and β_2 are total wavenumbers for two different waves; they are the roots of the following characteristic equation

$$\frac{\omega}{\omega_{ce}}\beta^2-k\beta+\frac{en_0\mu_0\omega}{B_0}=0 \tag{1.29}$$

and are found to be

$$\beta=\frac{k\omega_{ce}}{2\omega}\left[1\mp\left(1-\frac{4\omega k_w^2}{\omega_{ce}k^2}\right)^{1/2}\right] \tag{1.30}$$

where $k_w=(\omega n_0\mu_0 e/B_0)^{1/2}$, the whistler wavenumber in free space.

It is noted at this point that there exist upper and lower bounds on the axial wavenumber for any set of fixed physical parameters. Solving the characteristic equation 1.29 for k and differentiating with respect to β yields a minimum k of

$$k_{min} = 2\frac{\omega_p \omega}{\omega_{ce} c} \tag{1.31}$$

and a maximum k of

$$k_{max} = \frac{\omega_p}{c}\left[\frac{\omega/\omega_{ce}}{1-\omega/\omega_{ce}}\right]^{1/2} \tag{1.32}$$

Envelopes of allowed k are shown as a function of operating frequency for several magnetic fields in figure 1-2. It is clear that a broader spectrum of k is allowed for larger magnetic fields; for an insulating boundary that spectrum is continous within the envelope[5].

The two roots in 1.30 are well separated when the axial helicon wavelength in the plasma is small in comparison to the free space whistler wavelength for all frequencies of interest; in this limit of $\omega k_w^2 \ll \omega_{ce} k^2$ the roots become

$$\beta_1 \quad = k_w^2/k \tag{1.33}$$

$$\beta_2 \quad = k\omega_{ce}/\omega \tag{1.34}$$

It has been shown that β_1 corresponds to the classical H-wave whereas β_2 is associated with electrostatic electron cyclotron waves (Trivelpiece-Gould modes hereon referred to as TG-waves)[5]. The mode coupling is thought to play a role in plasma energy deposition[13].

Of relevance is the eigenvalue problem in the limit of $\omega/\omega_{ce} \approx 0$; this corresponds to wave solutions for large magnetic fields (for Argon plasmas with $B = 1000G$ and $f = 13.56$Mhz, $\omega/\omega_{ce} = .036$). In this limit β_2 approaches infinity and the total wave solution $\mathbf{B}$ is essentially that of a pure H-wave; TG-wave contribution is small since that wave's amplitudes are small in comparison to H-wave amplitudes (and consequently difficult to detect using conventional diagnostics). The $\hat{\mathbf{z}}$ component of equation 1.27 (note that $\nabla^{\mathbf{2}}$ is the *vector* Laplacian in cylindrical coordinates[2]) is given by

$$\frac{\partial^2 B_z}{\partial \bar{r}^2} + \frac{1}{\bar{r}}\frac{\partial B_z}{\partial \bar{r}} + \left[1 - \frac{m^2}{\bar{r}^2}\right] = 0 \tag{1.35}$$

which has a finite solution $B_z = C_1 J_m(\bar{r})$ with $\bar{r} \equiv (\beta_1^2 - k^2)^{1/2} r \equiv k_\perp r$; where $k_\perp$ is the transverse

[2]The vector Laplacian is obtained from the identity $\nabla^{\mathbf{2}}\mathbf{B} = \nabla(\nabla \cdot \mathbf{B}) - \nabla \times (\nabla \times \mathbf{B})$

wavenumber. The $\hat{\mathbf{r}}$ and $\hat{\theta}$ components of equation 1.25 are

$$im\frac{B_z}{r} - ikB_\theta = \beta_1 B_r \tag{1.36}$$

$$ikB_r - \frac{\partial B_z}{\partial r} = \beta_1 B_\theta \tag{1.37}$$

The above equations form a closed set and may be solved for B_r and B_θ in terms of the solution for B_z above.

$$B_r = \frac{iC_1}{k_\perp^2}\left[\frac{m\beta_1}{r}J_m + k\frac{\partial J_m}{\partial r}\right] \tag{1.38}$$

$$B_\theta = \frac{C_1}{k_\perp^2}\left[\frac{mk}{r}J_m + \beta_1\frac{\partial J_m}{\partial r}\right] \tag{1.39}$$

which may be simplified using the Bessel recursion relations

$$\frac{2m}{\bar{r}}J_m = J_{m+1} + J_{m-1} \tag{1.40}$$

$$-2\frac{\partial J_m}{\partial \bar{r}} = J_{m+1} - J_{m-1} \tag{1.41}$$

The general solution for the r dependence of $\mathbf{B}$ is then given by

$$B_r = \frac{iC_1}{2k_\perp}\left[(\beta_1 - k)J_{m+1} + (\beta_1 + k)J_{m-1}\right] \tag{1.42}$$

$$B_\theta = \frac{C_1}{2k_\perp}\left[(\beta_1 - k)J_{m+1} - (\beta_1 + k)J_{m-1}\right] \tag{1.43}$$

$$B_z = C_1 J_m \tag{1.44}$$

the solution for the r dependence of $\mathbf{E}$ is found from equation 1.14

$$E_r = \frac{\omega}{k}B_\theta \tag{1.45}$$

$$E_\theta = -\frac{\omega}{k}B_r \tag{1.46}$$

$$E_z = 0 \tag{1.47}$$

Note that $E_z = 0$ is a consequence of neglecting electron mass in 1.19 or equivalently considering the limiting case of $\omega_{ce}/\omega \approx 0$; application of either of these conditions implies that collisional damping is neglected as well. The scalar constant C_1 in the above solutions will depend on the operating conditions (i.e. antenna-plasma coupling and power absorbed). For an insulating boundary the solutions for $\mathbf{E}$ and $\mathbf{B}$ are subject to the condition that $j_r = 0$ at $r = a$. Equations 1.15 and 1.25 may be combined to get

$$j_r = 1/\mu_0(\nabla \times \mathbf{B})_r = \beta_1 B_r \tag{1.48}$$

then $B_r(a) = 0$ is an equivalent boundary condition. Application of this condition yields

$$(\beta_1 - k)J_{m+1} = -(\beta_1 + k)J_{m-1} \tag{1.49}$$

This expression together with 1.33 yields the dispersion relationship. For any given axial and azimuthal wavenumber, equation 1.49 may be numerically solved for β_1 where the nth solution to this equation (corresponding to the nth Bessel zero) is the radial mode number. A closed form solution may be obtained by simplifying 1.49 with the use of the Bessel recursion relations with the result

$$J_m(\bar{r}) = \frac{ka}{2m\beta_1}\left[J_{m1}(\bar{r}) - J_{m-1}(\bar{r})\right] \tag{1.50}$$

The only finite solution for $m = 0$ occurs when $J_{+1}(\bar{r}) - J_{-1}(\bar{r}) = 0$ or equivalently $J_1(\bar{r}) = 0$. The solution for $m = 1$ shows weak dependence on the right hand side of the above expression in the limit of long, thin cylindrical geometries ($ka \ll 1$ and $k_\perp \approx \beta_1$) appropriate for the application under consideration. The aforementioned constraints together with 1.33 yield an expression for the disperion relation which is exact for $m = 0$ and approximate for $m = 1$[7]

$$\frac{\omega}{k} = \frac{3.83B_0}{e\mu_0 n_0 a} \tag{1.51}$$

where the symbols have their usual meanings and the numerical factor is just the first zero of J_1, corresponding to the lowest radial mode. The lowest radial mode is chosen since one would expect a low-order solution to be the dominant contribution to the total solution (certainly true

far from the source). Note that the density and source radius are inversely proportional when all other parameters are fixed, illustrating the advantage of compact helicon sources. The azimuthal mode of interest is the $m = +1$ since it has been experimentally demonstrated that this mode is preferentially excited over $m = -1$ [8]. Figure 1-1 shows the linear variation of plasma density as a function the applied magnetic field for $n = 0, m = 1, 10 < k < 85$, $f = 13.56$MHz and $a = 1$cm. It has been experimentally demonstrated that the density does indeed vary linearly but saturates at a critical magnetic field with a dependence experimentally determined to vary as $A^{1/5}$ where A is the atomic number of the gas species[14]; the critical field for Ar was observed to be approximately 760G. The source under present consideration is significantly more compact than its counterparts in the literature and it is consequently difficult to apply quantitative experimental results to the application at hand without some knowledge of scaling laws. It is sufficient to note that for large enough fields ($>$ 1000G) one will achieve the highest density possible for a given discharge.

It is appropriate at this point to verify the the validity of the assumptions made in the derivation of the dispersion relation. It may be deduced from figure 1-1 and equation 1.33 that the traverse helicon wavelength $k_\perp^2 \equiv \beta_1^2 - k^2$ is much greater than the electron larmor radius. For typical helicon plasmas under consideration, $B \approx 1500G, T_e \approx 5$eV and $f = 13.56$MHz, yielding an electron larmor radius on the order of .1mm and a transverse helicon wavelength ($\lambda \equiv 2\pi/k_\perp \equiv 2\pi(\beta_1^2 - k^2)^{-1/2}$) of approximately 2cm. Electrons do not see a spatial variation in the perturbed fields during any given gyration and therefore experience no shear stress; the earlier assumption of negligible viscosity is justified.

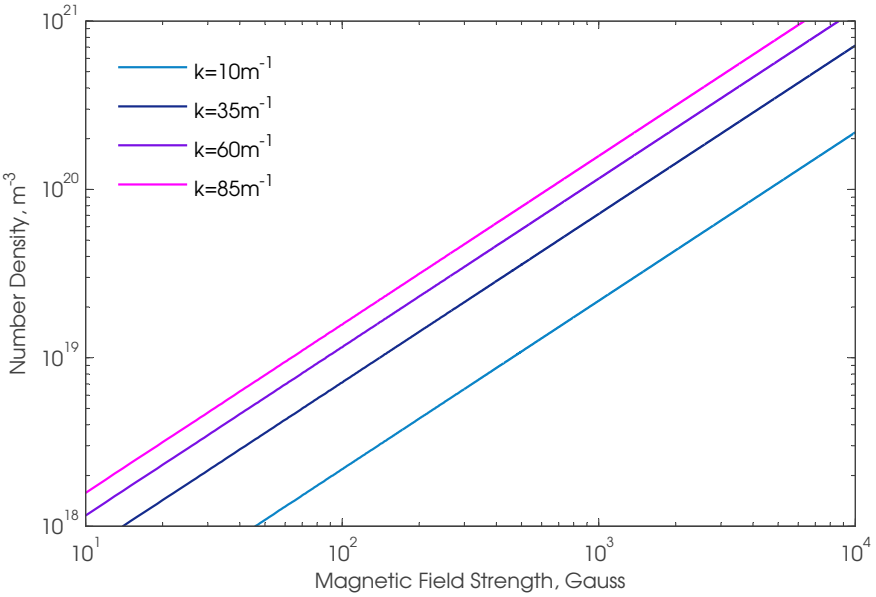

Figure 1-1: Density vs. magnetic field strength for $a = 1$cm, $f = 13.56$MHz and typical values of k from the approximate dispersion relation for $m = +1$; density increases with k.

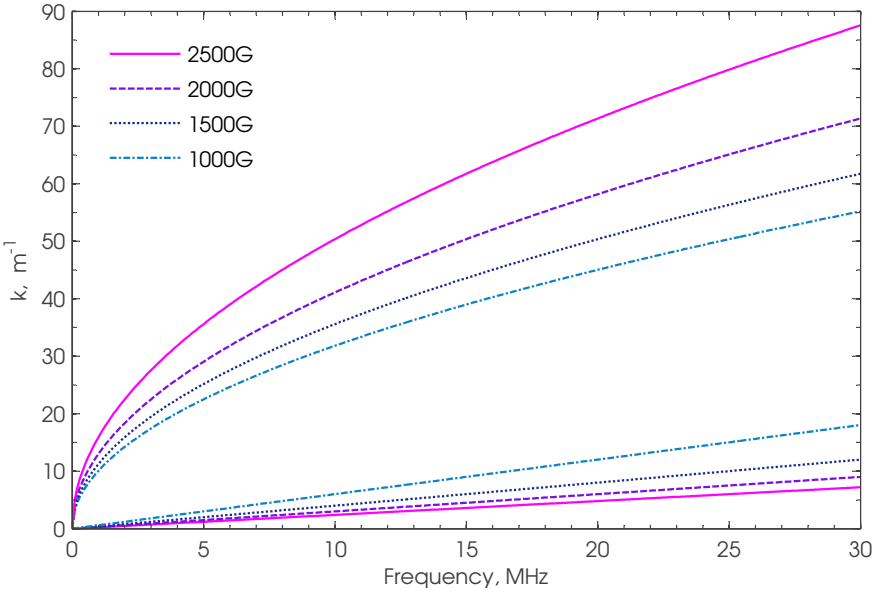

Figure 1-2: k_{min} and k_{max} vs. frequency for $a = 1$cm, $n = 2 \times 10^{19} m^{-3}$ and typical magnetic fields; a larger spectrum of k is allowed for higher fields.

1.2.2 Effect of Ion Motions

The effect of ion motions may be considered by adding an second term to 1.16

$$\mathbf{j} = -en_0(\mathbf{v_e} - \mathbf{v_i}) \tag{1.52}$$

where the ion and electron velocities are found from the fluid equations

$$-in_0\omega m_i\mathbf{v_i} = en_0(\mathbf{E} + \mathbf{v_i} \times \mathbf{B_0}) \tag{1.53}$$

$$-in_0\omega m_e\mathbf{v_e} = -en_0(\mathbf{E} + \mathbf{v_e} \times \mathbf{B_0}) \tag{1.54}$$

The fluid equations may separated into components parallel and perpendicular to the applied magnetic field. The solution for $\mathbf{v_{i,e\|}}$ is straightforward; the $\mathbf{v} \times \mathbf{B}$ terms vanish and the parallel electric field accelerates ions (and electrons) in the absence of collisions. In the limit of negligible electron inertia and absence of collisions, this field must vanish, per the formulation of the preceding section. The effective parallel electric field seen by particles however, may nevertheless be non-zero due to collisionless damping. Taking the cross product of both sides of 1.53 and 1.54 with $\hat{\mathbf{z}}$ and backsubstituting into the original equations yields the perpendicular velocities

$$\mathbf{v_{i\perp}} = \frac{\omega_{ci}/\omega}{1-(\omega_{ci}/\omega)^2}\frac{i}{B_0}\left(\mathbf{E} + i\frac{\omega_{ci}}{\omega}\mathbf{E} \times \hat{\mathbf{z}}\right) \tag{1.55}$$

$$\mathbf{v_{e\perp}} = \frac{\omega/\omega_{ce}}{1-(\omega/\omega_{ce})^2}\frac{i}{B_0}\left(\mathbf{E} - i\frac{\omega_{ce}}{\omega}\mathbf{E} \times \hat{\mathbf{z}}\right) \tag{1.56}$$

which may then be combined with 1.52 and solved for the electric field, yielding[7]

$$\mathbf{E}_\perp = \frac{B_0}{en_0}\left[\left(\frac{1-\omega_{ci}/\omega_{ce}}{1+\omega_{ci}/\omega_{ce}}\right)\mathbf{j} \times \hat{\mathbf{z}} + i\frac{\omega_{ci}/\omega - \omega/\omega_{ce}}{1+\omega_{ci}/\omega_{ce}}\mathbf{j}\right] \tag{1.57}$$

the above result may then be substituted in place of 1.20 and the formulation developed as before, yielding the vector equation for $\mathbf{B}$ as before[3]

$$\left(\frac{\omega_{ci}/\omega - \omega/\omega_{ce}}{1+\omega_{ci}/\omega_{ce}}\right)\nabla \times \nabla \times \mathbf{B} - k\nabla \times \mathbf{B} + \frac{en_0\mu_0\omega}{B_0}\mathbf{B} = 0 \tag{1.58}$$

Note that both 1.57 and 1.58 reduce to 1.20 and 1.23 respectively, in the limit

$$\omega \gg (\omega_{ci}\omega_{ce})^{1/2} \equiv \omega_{lh} \tag{1.59}$$

subject to the condition that $\omega_{ci} \ll \omega_{ce}$. Collisional damping is easily included by replacing ω everywhere in 1.55 and 1.56 with $\omega + i\nu_i$ and $\omega + i\nu_e$, respectively and carrying through the formulation above; damping will only serve to help meet the the criterion above. Since the cyclotron frequencies are directly proportional to the field, this criterion is not met if B_0 is too large; for operation with Argon at $B = 1500G$ with $\omega = 2\pi 13.56\text{MHz}$, $\omega_{lh} = 2\pi 15.5\text{MHz}$. The ion mass effect is clearly larger than the electron mass effect for moderate B_0, but the inertia term in 1.58 may nevertheless be neglected if it is small in comparison to the other terms; this is the case for

$$k \gg \left(\frac{\omega_{ce}/\omega - \omega/\omega_{ce}}{1 + \omega_{ci}/\omega_{ce}}\right)\frac{en_0\mu_0\omega}{B_0} \approx \frac{e^2 n_0}{\epsilon_0 m_i}\frac{1}{c^2} \tag{1.60}$$

The right hand side of the above expression may be interpreted as the approximate ion plasma skin number[3]. This criterion is generally satisfied in the plasmas of interest; k is typically of order several $10m^{-1}$ whereas the plasma ion skin number for Argon is approximately $5m^{-1}$ for even the highest discharge density of $1 \times 10^{19}m^{-3}$.

1.3 Antennas and Wave Excitation

Helicon waves may be excited with the use of several antenna configurations. Antenna design optimization for ultra-compact sources ($a = 1\text{cm}$, $l \approx 20\text{cm}$) has not been previously considered in the literature. It was shown from the physics discussion in the preceding sections that the helicon wave may be left or right hand circularly polarized and consequently plane polarized by superposition as well. This presents options in terms of wave excitation and antenna design. One may excite the H-wave with a simple multi-loop antenna ($m = 0$) such as the Nagoya III antenna[8] or use more sophisticated geometries to preferentially excite certain modes. The discussion in the preceding section provides an overview of the physics and insight into wave propagation, but it does not encompass all of the relevant physics, for the simple reason that some aspects are poorly understood and are currently being pursued as research topics. Plasma source efficiency

Figure 1-3: Right hand polarized half-helical antenna (RH-HH), used to excite predominantly the $m = +1$ mode; the helical arms twist counterclockwise away from their originating ring rotating 180° before terminating on the second ring, setting the antenna length at one half the axial wavelength.

and electron heating is one of these topics but asymmetries between modes (i.e. $m = +1$ vs $m = -1$) is another. For instance, it has been experimentally demonstrated that the $m = +1$ mode is preferentially excited (that it is the major contributor to mode content), regardless of antenna geometry. Furthermore, it has been shown that the $m = +1$ mode achieves a higher peak density than its counterpart[8] and has a lower power threshold for high-density helicon mode operation[15]. It is desirable for these reasons to design an antenna which best couples with the $m = +1$ mode. This is achieved by using a geometry that closely matches the form of that mode in space. One such possibility is the right handed half-helical antenna (RH-HH) illustrated in figure 1-3. It is denoted a half-helical antenna since the helical arms rotate 180° with respect to their ring of origin before they terminate on the second ring. The antenna is deemed a right-handed antenna since it is designed to launch right hand circularly polarized waves ($m = +1$) parallel to $\mathbf{B}$ and left hand polarized waves antiparallel to $\mathbf{B}$. The helicity sense determines the antenna type; note that the right handed half-helical antenna of figure 1-3 has helical arms which twist in a *counter*-clockwise direction as the arms move away from their originating ring, independent of how the antenna is oriented; the winding sense is opposite the wave polarization as a result of Lenz's Law. A left-handed antenna is also possible, and in that case one could reverse the direction of $\mathbf{B}$ and obtain an identical discharge; it has indeed been experimentally proven that reversing both the helicity of the antenna and the direction of the field yields a configuration indiscernable from that of the original[8].

The antenna length determines the axial wavenumber k just as the rotational (a)symmetries set

the azimuthal wavenumber launched. In selecting the axial wavelength one must consider i) values of k within the allowed envelope for a given frequency and magnetic field, as illustrated in figure 1-2 and ii) values of k so as to maximize the efficiency of the source (maintain a low ion cost). The first condition is trivially met; designing for the second condition requires an understanding of the underlying mechanisms for efficient plasma production. It has been experimentally demonstrated that the energy absorption rate is several orders of magnitude larger than what one would expect from collisional damping alone[9]. Initially Landau damping and later energy absorption via mode conversion at the boundary to Trivelpiece-Gould waves were proposed as potential damping mechanisms to account for the discrepancy[7, 10, 13]. It has been theoretically shown that the the energy absorption spectrum in k is significantly altered when one includes Trivelpiece Gould modes in antenna loading calculations. In that case the power absorption profile was shown to be hollow with most of the energy absorbed near the boundary. The absorption spectrum had a peak at k corresponding to primary electron energies in the range 10-100eV for Argon; that peak increased and broadened with density[13]. This result suggests that excitation of a broader spectrum of k would be needed for more efficient operation, specifically k would decrease with density and from figure 1-2 larger magnetic fields would be needed. For large enough fields the maximum attainable density saturates as mentioned previously; the choice of k in that case has no influence on plasma density and should reflect energy absorption considerations. It is then desirable to use an antenna which predominantly excites k corresponding to primary electron energies just above the peak (slightly smaller k or correspondingly larger λ) so as to allow the antenna to excite harmonics and couple power to them. The axial wavelength in experiments is generally chosen in correspondence with this result; the expression relating the axial wavelength to the energy of fast primaries is simply

$$\frac{1}{2}m_e(\omega/k)^2 = eE \tag{1.61}$$

where E is the energy in electron volts. It should be noted that the expression above does not imply that Landau damping is indeed the dominant mechanism, rather the above formulation is a convenient one[**?**]. For the case of a half-helical antenna, the antenna length corresponds to one-half the axial wavelength, thus the expression relating antenna length to k is just $l_a = \pi/k$, or

$$l_a = \frac{\pi}{\omega}\left(\frac{2eE}{m_e}\right)^{1/2} \tag{1.62}$$

The antenna configuration illustrated in figure 1-3 has been found to be particarly effective at exciting the $m = 1$ mode[8]. Alternative configurations to the RH-HH antenna such as the bifilar antenna (each helical arm composed of two filaments) have also been used; the filaments are driven with the same frequency but with 90° of phase difference so as to better match the wave pattern in time[16].

Chapter 2

Design of a Helicon Plasma Thruster

The design of a compact helicon plasma thruster is outlined in the following sections. The general anatomy of the thruster is presented with a brief description of pertinent components. Consideration is given to the amount of radio-frequency power and propellant needed to sustain a given discharge based on a simple power balance; various propellant options are discussed. Finally, the design of a prototype compact thruster for the purposes of laboratory testing is presented.

2.1 Overview

The helicon plasma thruster under consideration is a 2cm (plasma) diameter, 20cm long thruster with a maximum operating power of 1.2kW at frequency of 13.56Mhz, yielding a power density of 16MW/m^3. Neutral propellant gas is injected, efficiently ionized with the use of helicon waves, and accelerated outward at supersonic speeds; the latter is demonstrated in following chapters. The helicon wave physics discussion of the preceding chapter related plasma density to some experimental parameters such as magnetic field strength and antenna geometry. One must consider additional discharge physics such as collisions and diffusion in the context of the thruster. This enables one to both complete the physical design and serves as a starting point for experimentation in terms of knowledge of the input power and gas flow rates required to sustain a discharge. At this time it is appropriate to introduce the anatomy of the thruster under consideration; it is illustrated in figure 2-1.

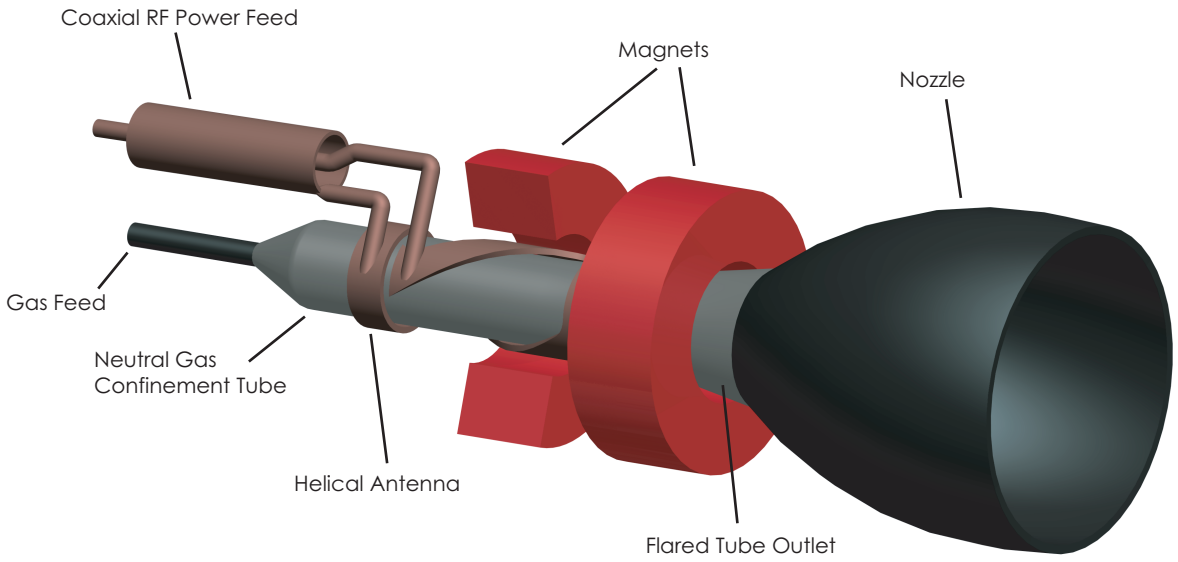

Figure 2-1: Anatomy of a basic helicon plasma thruster with helical antenna, neutral gas confinement tube with flared outlet, permanent or electromagnets, nozzle, coaxial RF feed and gas feed.

The overall length of the thruster is approximately 20cm, with a plasma radius of $a = 1$cm. The antenna has a right handed half-helical geometry with a length of approximately 10cm for operation at 13.56MHz; this corresponds to $k = 31\text{m}^{-1}$ or a resonant electron energy of 20eV. The fields required for helicon wave propagation are then approximately upwards 1000G, producing plasma densities of order 10^{19}m^{-3}, as deduced from figures 1-2 and 1-1. An insulating tube is used to confine the neutral gas before it is ionized; this is often referred to as the neutral gas confinement tube (NGCT). The antenna is surrounded by a magnet which provides the axial magnetic field necessary for helicon wave propagation; these magnets may be electromagnets or permanent magnets. The design and optimization of the nozzle section is a magnetohydrodynamics problem[17] and is beyond the scope of this work; it is included for completeness. The relative positioning of the antenna, magnets, and NGCT are subject to optimization. It was found qualitatively that discharges with an extended plume were produced for antennas positioned with an axial offset relative to the magnets, as shown in figure 2-1. Launching helicon waves into a slight gradient of magnetic field converts a double-ended source into a single-ended one, as the $m = -1$ mode can not propagate upstream towards the gas feed for the configuration under consideration.

2.2 Power and Propellant Scaling

It was noted earlier that one of the advantages of physically scaling down helicon technology was the ability to achieve discharges of higher density. This is offset by the fact that a proportionally greater amount of power and propellant is needed to sustain any given discharge; since the density is larger and the cross sectional area smaller, ∇n and consequently the rate of radial diffusion for particles will be larger, assuming all other parameters such as the axial magnetic field remain constant. This section considers the amount of power and propellant required to sustain a plasma discharge with a prescribed density.

Particle and Power Losses

The preceding chapter showed that ion effects are generally negligible in the context of helicon wave physics, however one must consider the effects of ion temperature on particle confinement. The ion temperature in the discharge region has been experimentally shown to be anisotropic with a $T_{i\perp}$ which increases with magnetic field and a $T_{i\|}$ which remains constant. Values of $T_{i\perp} \approx .2$eV and $T_{i\|} \approx .5$eV at 1000G were typical in that experiment which had power densities comparable to the system under consideration[18]; it is assumed as a starting point that ion temperatures in the discharge region will be of this order. For $B_0 \approx 1500$G in the discharge region (the 20cm region around the antenna) it is assumed that $T_{i\perp} = .5$eV in Argon which yields an ion larmor radius $r_L = .22$cm. Thus, for the large fields under consideration, the criteria for ion confinement and negligible inertial effects in helicon wave physics are simultaneously met. Note that if the magnetic field is small enough so that the ion larmor radius is greater than the tube radius then ions will diffuse towards the walls more quickly than electrons and an ambipolar electric field will be setup to confine ions radially. It is of interest to determine the radial and axial particle losses; this amounts to calculating radial and axial fluxes $\Gamma_{i\perp}$ and $\Gamma_{i\|}$, respectively. The exact problem of diffusion in the present context is inherently three-dimensional. The ionization region near the antenna is essentially a localized source which produces plasma with density of order $1 \times 10^{19}\mathrm{m}^{-3}$. The plasma density falls off in the axial directions as particles diffuse towards the walls and nozzle; this density gradient in turn determines the rate of particle diffusion. The problem is decoupled here for simplicity - the radial and axial fluxes are solved independently with the goal of determining an order of magnitude estimate of particle and power losses. The radial flux is governed by Spitzer diffusion across a magnetic field[19]

$$\Gamma_\perp = -D_\perp \nabla n = \frac{\eta_\perp n(KT_e + KT_i)}{B^2}\nabla n \tag{2.1}$$

where $D_\perp$ is the classical diffusion coefficient for a fully ionized plasma and $\eta_\perp = 2\eta_\parallel$ the Spitzer resistivity with approximate value $\eta_\perp \approx 3.2 \times 10^{-5}$ohm-m for $T_e \approx 5$eV. The above result is applicable for fully ionized plasmas with magnetized ions; the diffusion rate for electrons and ions is then the same and no ambipolar field arises. Combining this result with the equation of continuity yields the diffusion equation in the tranverse dimension

$$\frac{\partial n}{\partial t} + \frac{\eta_\perp (KT_e + KT_i)}{B^2}\nabla\cdot(n\nabla n) = S \tag{2.2}$$

In steady state $\partial n/\partial t = 0$ and away from the ionization region $S = 0$ reducing the above expression to

$$\nabla\cdot(n\nabla n) = \frac{1}{2}\nabla\cdot(n\nabla n + n\nabla n) = \frac{1}{2}\nabla\cdot(\nabla n^2) = 0 \tag{2.3}$$

where the simplification is made using a vector identity[1]. The solution to the Laplacian for n^2 in cylindrical coordinates with the boundary condition $n(r)$ at $r = a$ yields

$$n(r) = \{n_0^2 J_0(z_{01} r/a)\}^{1/2} \tag{2.4}$$

where n_0 is the peak density on-axis, a the radius of the tube, and $z_{01} = 2.405$, the first zero of J_0. This expression is then subsitituted into equation 2.1 to obtain the radial particle flux

$$\Gamma_\perp = \frac{1.2\eta_\perp (KT_e + KT_i)}{aB^2} n_0^2 J_1(z_{01} r/a) \tag{2.5}$$

The radial power loss at $r = a$ for $T_e \approx 5$eV may be expressed as

$$P_\perp = 2\pi a L e \alpha_c \Gamma_\perp = .64 \left(\frac{n_{19}}{B}\right)^2 L \tag{2.6}$$

where the numerical formula on the right hand side is expressed in SI units with density in multiples of $1 \times 10^{19} m^{-1}$ for an ion cost $\alpha_c = 200$eV; note that the result is independent of radius. The radial

[1] $\nabla(AB) = A(\nabla B) + B(\nabla A)$

losses for the case of partial confinement (ion larmor radius greater than tube) is governed by ambipolar diffusion. The solution is similar to the formulation above, except that the diffusion coefficient in that case does not depend on density and the solution consequently goes like J_0 rather than $J_0^{1/2}$. The solution for that case may be found in the literature[3]; it is given as the numerical expression

$$P_\perp = 2\left(\frac{n_{19}}{B}\right)^2 L \tag{2.7}$$

in the same units as equation 2.6 for an ion cost of 200eV as well. It is provided here for comparison against equation 2.6; note that the particle and power loss is greater by approximately a factor of 3 when ions are not confined, as expected.

The axial particle flux will depend on specific ion acceleration mechanisms, the identification of which is one of the goals of this thesis. It is expected that ambipolar diffusion will at minimum accelerate ions to the acoustic sound speed. The minimum particles loss is then governed by ambipolar diffusion, with a diffusion coefficient which may be expressed as[19]

$$D_{a\|} \equiv \frac{\mu_i D_e + \mu_e D_i}{\mu_i + \mu_e} \approx D_{e\|}\left(1 + \frac{T_i}{T_e}\right) \tag{2.8}$$

where the Einstein relations have been invoked with the approximation $\mu_e \gg \mu_i$, with $D_{e\|}$ given by

$$D_{e\|} = \frac{KT_{e\|}}{m_e \nu} = \frac{KT_{e\|}}{\eta_\| n e^2} \tag{2.9}$$

The solution to the diffusion equation is carried out in a similar manner as above. The boundary condition is taken to be that the ions reach the thruster nozzle with a velocity that of the ion acoustic velocity $c_s \equiv (KT_e/m_i)^{1/2}$ with a density of $n = n_0/e$. The condition is necessary (at minimum) since the plasma acts in such a way as to keep the ion and electron fluxes equal. The solution has been carried out and may be expressed as[3]

$$P_\| = 3.5 \times 10^5 \left(\frac{a^2}{L}\right) n_{19} \tag{2.10}$$

The above formulation is an approximation since one may not simply superimpose the solutions

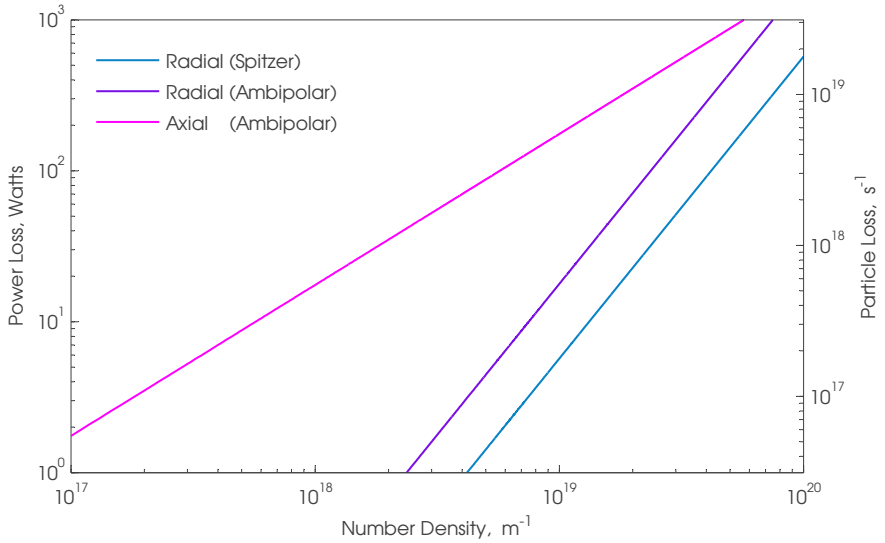

Figure 2-2: Particle and power losses as a function of density as governed by classical diffusion (Spitzer) and ambipolar diffusion (partial confinement) across a magnetic field ($B_0 = 1500G$). Axial contributions due to ambipolar fluxes are also shown for $a = 1$cm, $L = 20$cm.

of the diffusion equation in the perpendicular and parallel directions; the reason for this is of course that the equations are nonlinear. Nevertheless, the results give some insight into the magntiude of power and flow rate required for this particular thruster; the results of equations 2.6 and 2.7 are illustrated in figure 2.2. The results show that a compact source makes for a good ion pump; in order to fuel the discharge one must provide the combination of radial and axial particles lost every second.

Note that both formulations above have neglected volume recombination in the above expressions; it is assumed that recombination at the walls dominates. Furthermore, the particle loss rates calculated above do not include radial and axial fluxes due to fluid drifts; these drifts however may be neglected. The $\mathbf{E}_\perp \times \mathbf{B_0}$ and diamagnetic drifts are going to be in the azimuthal directions since $E_\perp$ has circular polarization and therefore do not contribute to particle losses. Drifts due to nonuniform magnetic field (e.g. expanding field lines near the nozzle) do not exist in a fluid[19].

Propellant Selection

Some useful properties of gas propellants such as atomic mass and ionization energies are listed in table 2.1. Noble gases are generally desirable for use as propellants since they are inert; gases such as Nitrogen and Argon are abundant and furthermore attractive as cost-effective fuels. The purity

Table 2.1: Propellant properties including atomic mass and first & second ionization potentials.

	Atomic Mass (amu)	Ionization Energy (eV)	
		I	II
^{7}N	14.007	14.53	29.60
^{10}Ne	20.180	21.56	40.96
^{18}Ar	39.948	15.76	27.63
^{36}Kr	83.798	13.99	24.36
^{54}Xe	131.293	12.13	20.98

of the gas must also be considered in addition to the species. The presence of impurities is not critical relative to other thruster topologies as it is in the case of hall thrusters with hollow cathodes; there the impurities are detrimental to cathode performance. Gases with impurities of 50 parts per million (ppm) are typical and readily available; impurities as low as 10ppm or better may be costly and are sometimes required for the case described in the preceding example. Argon is typically used in the laboratory for the aforementioned reasons, although Xenon is more attractive for the final space application as higher performance engines are realizable due to the lower ionization energy. The species may also be selected based on its atomic mass properties. In general a fixed amount of energy is absorbed by the plasma and used to accelerate ions. Species with a lower mass will attain higher velocities and hence higher I_{sp}, however the thrust will generally be lower per equation 1.3. This result is true for ambipolar acceleration mechanisms, to be discussed shortly.

2.3 Prototype Thruster Design

The thruster of figure 2-1 illustrates all of the necessary components for a complete spaceflight-like rendition of the helicon plasma thruster. For the purposes of laboratory testing one may simplify or remove several of these components since they will not be the focus of the present work. It is for this reason that the gas confinement tube of figure 2-1 is constructed with a uniform cross section and the nozzle omitted altogether. The experimental helicon thruster[20, 21, 22, 23, 24] is illustrated in figure 2-3. The implications of uniform gas confinement tube cross section are discussed in what follows; omission of the nozzle implies that particle detachment will not be at an optimium. The design of each of the experimental thruster's subsystems are discussed below.

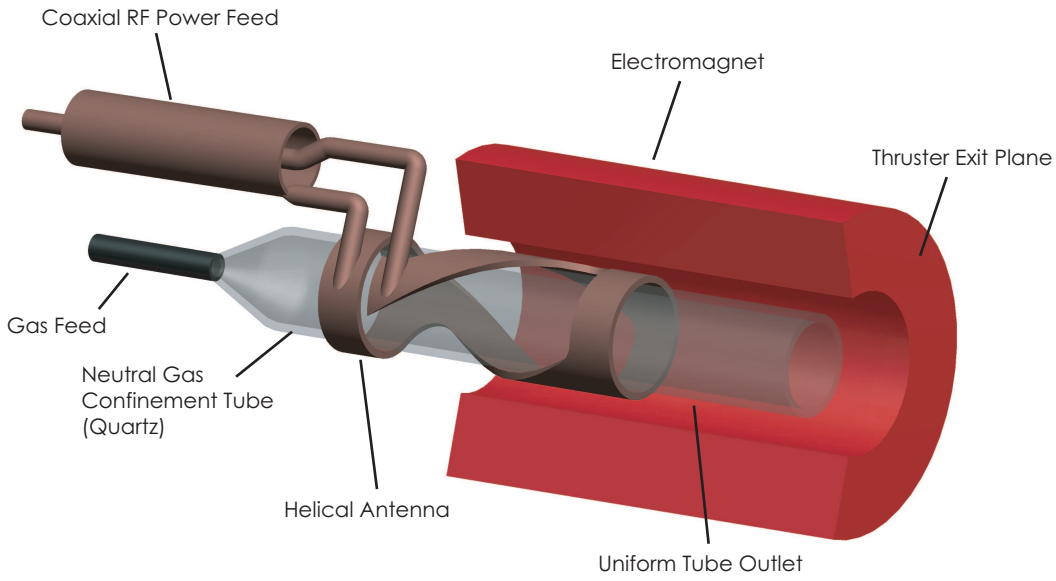

Figure 2-3: Actual experimental apparataus with helical antenna, neutral gas confinement tube with uniform cross section, single electromaget, coaxial RF feed and gas feed.

2.3.1 Power System

The thruster is operated in an isolated vacuum environment and a system is therefore required to monitor and transmit radio-frequency power to the thruster's coaxial feed as illustrated in figure 2-3. The complete system schematic is illustrated in figure 2-4, including impedance matching network (C_1,C_2), voltage sensing (C_3, C_4), current sensing (T_1), and load (L_A, $R_A + R_P$). Design of matching networks, current and voltage sensing as well as practical implementation considerations are discussed in what follows.

Transmission lines and impedance matching

Transmission lines will be an integral part of this system since the physical distance over which RF power must be transmitted is an appreciable fraction of the RF wavelength. The basic system with RF generator, source impedance Z_S, load impedance Z_L and two port impedance matching network is illustrated in figure 2-5. The load impedance represents the combined plasma and antenna impedance. It is assumed in the following analysis that the transmission line is impedance

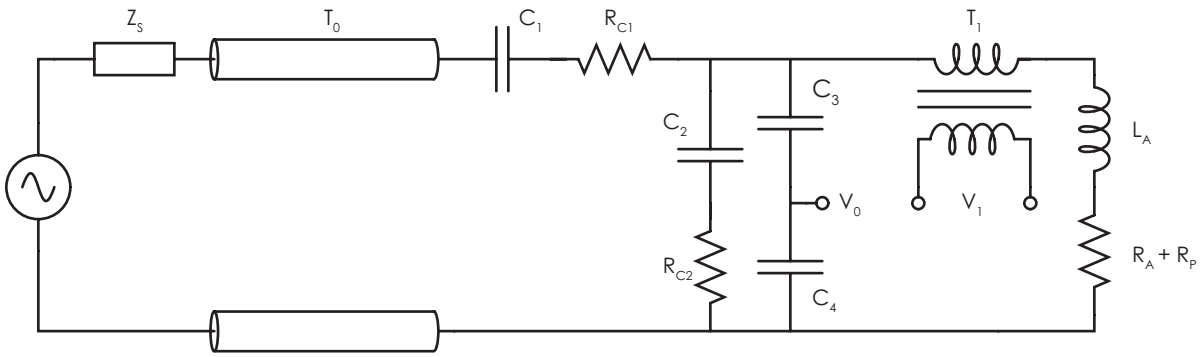

Figure 2-4: Complete helicon power system: RF generator with output impedance Z_S, impedance matched transmission line, L-matching network formed by C_1 and C_2 with respective ESR's R_{C1} and R_{C2}, voltage sensing with C_3 and C_4, current sensing with T_1, antenna inductance L_A and combined plasma & antenna resistance, $R_A + R_P$.

Table 2.2: Components used in the schematic of figure 2-4, with nominal values, tolerances and brief description. Estimates were made wherever exact specifications were available.

Component	Value	Tolerance (%)	Description
C_1	7-1000pF		Jennings CVCJ-1000-5S (70A rms, 5kV peak)
R_{C1}	7mΩ		ESR for C_1 (estimate) at $f_0 = 13.56$MHz
C_2	5-100pF	±10	Comet CV1C-100F/7.5kV (58A rms, 7.5kV peak)
R_{C2}	8mΩ		ESR for C_2 at $f_0 = 13.56$MHz
T_1	0.1V/A	±1	Current transformer; Pearson 6600
L_A	243nH	±20	Helicon antenna
R_A			Antenna and coaxial feed resistance
R_P	0.7Ω		Plasma resistance
Z_S	50Ω		Generator source impedance
T_0	50Ω		RG213/U, -4.9dB/100m loss, $V_p = 0.66$c
C_3	3pF	±5	2500V, stripline package (RF)
C_4	360pF	±5	2500V, stripline package (RF)

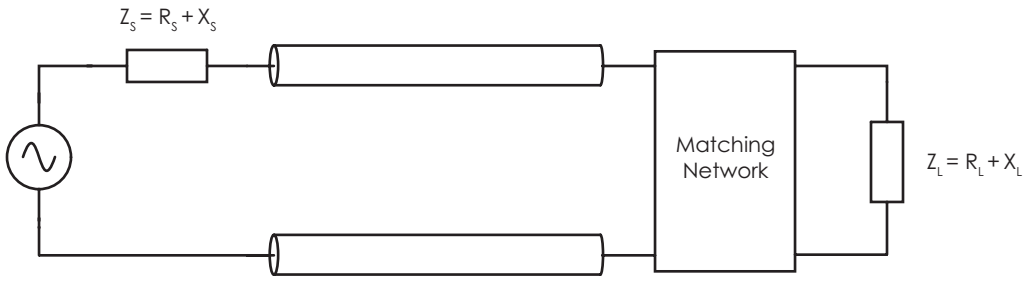

Figure 2-5: Radio-frequency generator with output impedance Z_S connected to an arbitrary load with impedance Z_L via transmission line matched to the generator; the load impedance may represent the combined antenna and plasma load.

matched to the source Z_S. In the absence of a matching network, the complex current flowing through the load may be expressed as

$$I_L = \frac{1}{\sqrt{2}} \frac{V}{Z_L + Z_S} \tag{2.11}$$

where $V = V_+ + V_-$, the superposition of forward and reflected waves amplitudes at the load. The average power delivered to the load may then expressed as

$$P = I^2 Re[Z_L] = \frac{1}{2} \frac{V^2 R_L}{(R_L + R_S)^2 + (X_L + X_S)^2} \tag{2.12}$$

which is maximized when $X_L = -X_S$. The impedance matching network must then be designed to transform the load impedance Z_L into the complex conjugate of Z_S so as to ensure maximum power transfer to the load. The voltage reflection coefficient for such a system may be written as

$$\Gamma = \frac{Z_N - 1}{Z_N + 1} \tag{2.13}$$

with $Z_N \equiv Z_L/Z_S$. The standing wave ratio and hence the voltage reflection coefficient is measured using a directional coupler (not indicated in the schematic) which is placed between the generator and the load. The reflection coefficient Γ does not vanish for $Z_L = Z_S*$ and reflections will occur. The reflections must however add in phase to deliver maximum power to the load[25], highlighting the subtleties of conjugate matching techniques. However, it is often the case that $\mathrm{Im}[Z_S] = 0$, reducing the conjugate matching condition to $Z_L = Z_S* = Z_S$ and suppressing reflections by virtue

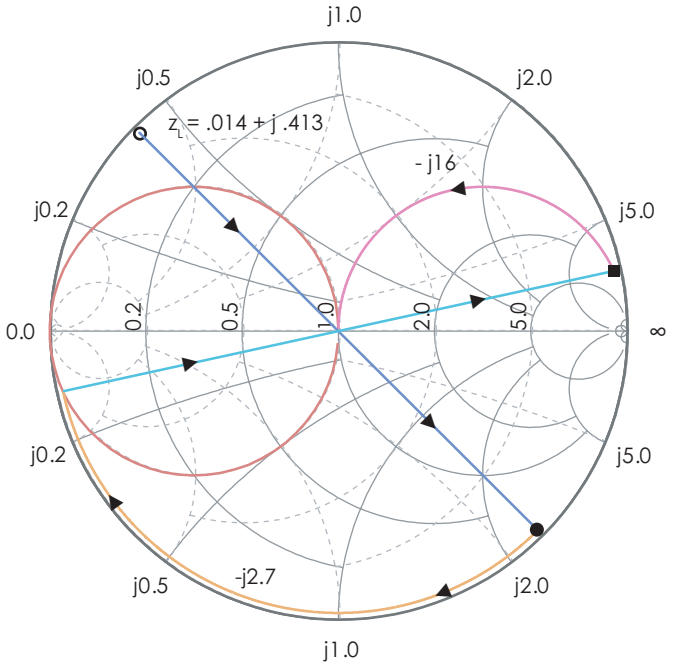

Figure 2-6: Impedance-admittance Smith chart with normalized load impedance $z_L = 0.014+0.413j$ (open circle). z_L is reflected into an admittance (filled circle) and brought to the SWR circle (red) by adding a susceptance of $-2.7j$. It is then reflected into an impedance (filled square) and added to a reactance of -16, bringing it to the origin to achieve $\Gamma = 0$.

of equation 2.13. Standard L-section matching networks are sufficient for narrowband conjugate matching. A series-shunt network is ideal for this application, as illustrated in figure 2-4; the network is formed by C_1 and C_2 with R_{C1} and R_{C2} representing the equivalent series resistance (ESR) of the capacitors. An alternative shunt-series network is also possible. The load as mentioned before consists of the antenna reactance as well as the antenna and plasma loading resistances. The characteristics of typical antenna were investigated with the use of a network analyzer. The antenna was found to have an inductance of approximately 240nH with an estimated resistance of 30mΩ. The resistance is sufficiently small that standard S-parameter measurements may not be used to accurately deduce the resistance. The plasma loading resistance however is an order of magnitude larger with typical values of 0.7Ω.

A graphical solution to the problem of impedance matching the load is shown in figure 2-6. The load impedance is first converted to an admittance since the first element from the load is a shunt susceptance. A susceptance of $-2.7j$ is then added to bring the load to the SWR circle on

the admittance chart. The admittance is then reflected back into an impedance and added to a series impedance of $-16j$, bringing the load to the origin of the chart and impedance matching it to the line. The normalized series reactance of $-16j$ an shunt susceptance of $-2.7j$ correspond to respective capacitor values of 14.7pF and 633pF for $f_0 = 13.56$MHz. However one must subtract the parallel capacitance added by the series combination C_3 and C_4; the inductance from the primary winding of T_1 is generally small and neglected. The accuracy of such a solution is limited however it is noted that the load values (particularly the antenna inductance) may vary depending on manufacturing tolerances. The matching network consisting of C_1 and C_2 is in reality constructed using variable capacitors to allow for tuning.

If greater accuracy is desired, an analytic solution may be used. The input impedance of the two-port network formed by C_1 and C_1 followed by the load may be expressed as

$$Z_1 = jX_1 + \frac{jX_1(R + jX_L)}{R + j(X_L + X_2)} \tag{2.14}$$

where R is the combination antenna and plasma loading resistance, and where X_1, X_2 and X_L are the series, shunt, and load reactances. Note that C_3 and C_4 are abosrbed in X_2 along with C_4, while any inductance from T_1 may be absorbed into X_L along with L_A. Equation 2.14 may then be rewritten in terms of its real and imaginary parts. The match requires the real and imaginary parts of Z_1 and Z_0 to be equal (assuming that the transmission line is matched to the generator), this yields the equations

$$X_1 = R^2(X_2 - Z_{0I}) + (X_2 + X_L)(X_2X_L - (X_2 + X_L)Z_{0I}) \tag{2.15}$$

$$X_2 = [X_L Z_{0R} \pm \{RZ_{0R}(R^2 + X_L^2 - RZ_{0R})\}^{1/2}]/(R - Z_{0R}) \tag{2.16}$$

where Z_{0R} and Z_{0I} are the real and imaginary parts of the source impedance and the remaining symbols have the usual meanings; note that there are two solutions. Application of these equations to the current analysis yields a normalized series reactance $-16.16j$ and a shunt susceptance $-2.69j$, corresponding to 14.5pF and 632pF, respectively. The solution with two capacitors (as opposed to an inductor and a capacitor) is chosen here since capacitors with good properties (e.g. low ESR, low dielectric loss, etc) are more readily available; a subtle point not illustrated in the graphical

solution. The analytic solution given by equations 2.15 and 2.16 have been used to compute the required values of shunt and series capacitances for a conjugate match and those values are shown in figures 2-7 and 2-8 as a function of load resistance for a few values of load inductance. The plasma resistance was experimentally measured using techniques discussed momentarily and is shown in figure 2-9 as a function of mass flow rate. The plasma resistance was not significantly sensitive to variations in power or magnetic field (for $P_0 > 600$W and $B_0 > 1000$G).

The reflection coefficient will in general be rather sensitive to capacitance value since the load will have narrow resonances given the antenna and plasma characteristics (Q $\approx$ 30). In practice, the sensitivity of the capacitors used in the network then becomes more important than a precise calculation of component values. The sensitivity is given by $\Delta C/C$, where ΔC is the smallest change in capacitance which may be achieved and C the total range of capacitance. ΔC will generally depend on implementation details (e.g. the product of capacitance to turns ratio and smallest angular resolution in physically tuning the capacitor). In addition to high Q, it is important to consider the finite equivalent series inductance (ESL). The presence of this parasitic effectively turns the capacitor into a resonant network; above the resonant frequency the capacitor becomes unuseable since it behaves as an inductor. ESL's of order 10nH were not uncommon for the C_1 and C_2, yielding resonant frequencies of order 100MHz.

Current and voltage sensing

The plasma resistance may be measured in real time if the antenna currents and voltages are known. This information may also be used to estimate matching network losses. Current sensing may be achieved with the use of a ferrite-core current transformer, represented as T_1 in the schematic (see table 2.2 for component information). The secondary winding in the schematic (with voltage V_1 across leads) represents an inductor wound on a ferrite ring, and the current being measured is passed through the center of this ring; there will be some mutual inductance and this is captured by the primary winding in the schematic. The time-varying current on the primary throws a time varying flux on the ferrite ring and hence the secondary. The flux linkage may be found from Maxwell's equations; Ampere's law becomes

$$\oint \mathbf{B} \cdot \mathbf{dl} = 2\pi a B = \mu_0 I_0 \sin(\omega t) \tag{2.17}$$

where I_0 is the ampliude of the time harmonic current, B the azimuthal field generated around that

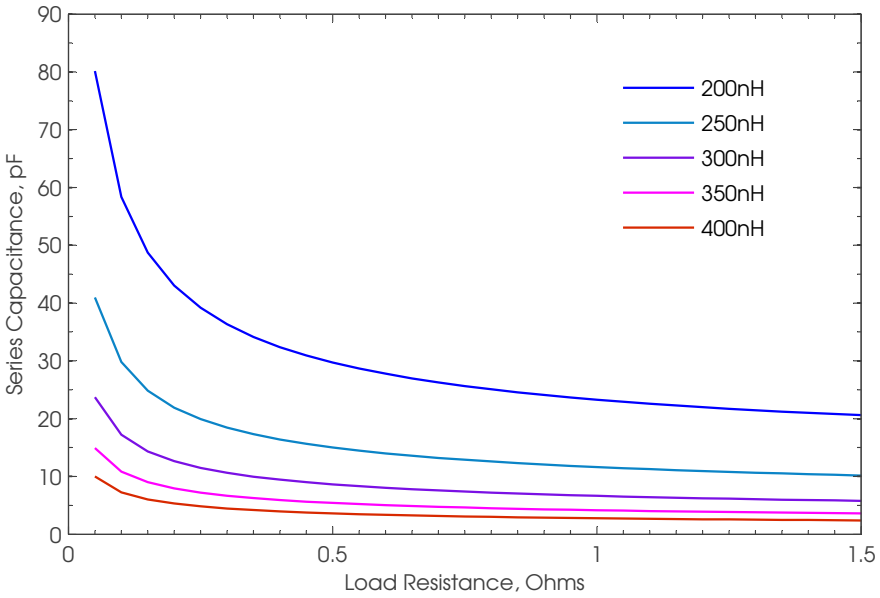

Figure 2-7: Series capacitance required for a conjugate match as a function of load resistance $(R_A + R_P)$ for several values of load inductance.

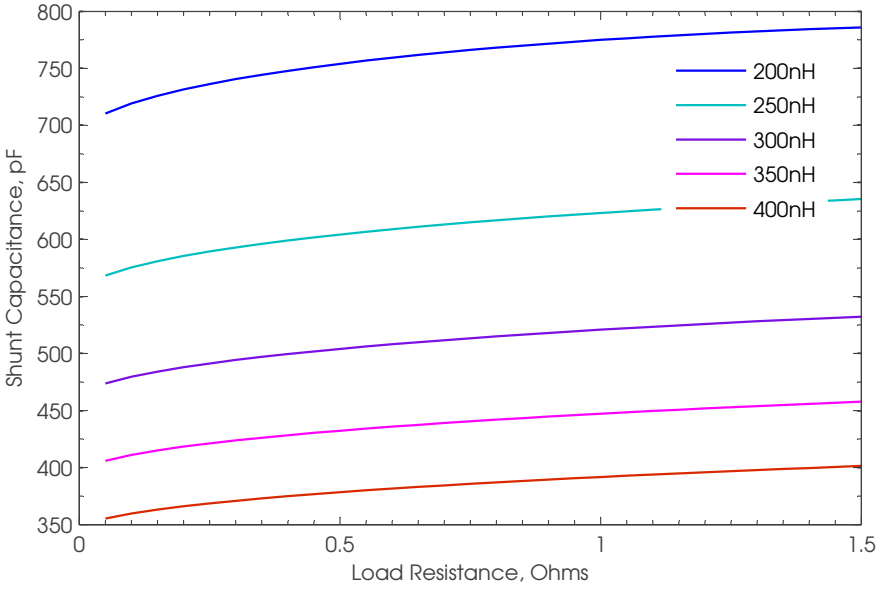

Figure 2-8: Shunt capacitance required for a conjugate match as a function of load resistance $(R_A + R_P)$ for several values of load inductance.

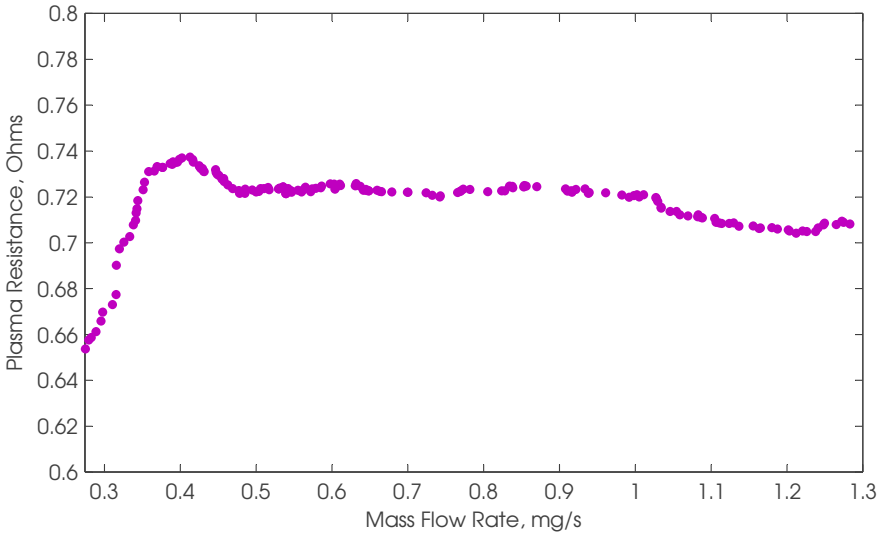

Figure 2-9: Plasma resistance for $P_0 = 635$W and $B_0 = 1540$G as a function of mass flow rate.

current and a the radius of the ferrite core. The time-varying flux on the secondary will induce a voltage on the leads which may be found from Faraday's law

$$\oint \mathbf{E} \cdot \mathbf{dl} = V_1 = N A_c \frac{dB}{dt} \tag{2.18}$$

where V_1 is the open-circuit voltage measured at the leads of the secondary, N the number of turns on the secondary, A_c the cross-sectional area of the ferrite ring, and dB/dt as found from 2.17. Note that the measurement is not subject to misalignment errors (e.g. current carrying wire off-center) due to the implied symmetries of equation 2.17. The above formulation illustrates the working principles behind the measurement; note that the frequency response is not going to be flat, as 2.18 will contribute a zero. The response may be designed to be flat with the use of additional passive components, and the sensor used does in fact exhibit a flat frequency response with upper and lower -3dB cutoffs of 25Hz and 120MHz and a gain of 0.1V/A. The sensor is terminated with a high impedance connection so as to draw negligible current and hence power from the circuit. The time-varying flux however results in ferrite core dissipation, giving rise to a small insertion loss.

Voltage sensing is accomplished with the use of a capacitive voltage divider formed by C_3 and C_4 in the schematic. High Q capacitors are not critical for this application since the high input impedance (by design) will draw little current. The voltage division ratio is

$$V_0 = \frac{C_3}{C_3 + C_4} V_A \tag{2.19}$$

where V_A is the voltage across the antenna. The input impedance to the divider is simply

$$Z = \frac{1}{\omega C_3} + \frac{1}{\omega C_4} \tag{2.20}$$

The antenna's impedance is considerable at the frequencies of interest, generating typical antenna voltages in the range of hundreds of volts. An attenuation of at least $100:1$, output impedance of 50 ohms or less and input impedance of n output impedance of 100kΩ is desired so that V_0 may be interfaced with a data acquisition system, setting $C_3 = 3$pF and $C_4 = 360$pF for an attneuation of 121:1 and input and output impedances of $4k\Omega$ and 32Ω. The input impedance of $4k\Omega$ may seem low however it is two orders of magnitude larger than its parallel connected elements. In addition, the divider adds approximately 3pF to the shunt capacitance of the matching network.

Loss Mechanisms

The power system will have several loss mechanisms and some of these discussed in what follows. One may express the loss magnitudes in terms of the power drawn from the source however in that case a standing wave ratio larger than 1:1 will lead to additional losses in the transmission line and must be accounted for as well. In order to decouple the problem losses are specificed in dB with respect to power delivered to the load. and the mismatch losses must be specified as well. The impedance matching capacitors will have a finite ESR, and the losses associated with it may be calculated as follows, assuming that the voltage divider draws negligible current. It is easiest to start at the load; given a current I_L is flowing through the branch consisting of the load, the voltage across that branch in steady state must be

$$V_L = I_L Z_L \tag{2.21}$$

this voltage appears across the branch containing C_2 and R_{C2}, causing that branch to draw a current of

$$I_2 = I_L Z_L / Z_2 \tag{2.22}$$

The sum of I_2 with I_L must equal the total current flowing through the branch consisting of C_1 and R_{C1}

$$I_1 = I_L + I_2 = I_L(Z_L/Z_2 + 1) \tag{2.23}$$

The power delivered to the load is just $I_L^2(R_A + R_P)$, and the power dissipated in the capacitors may be expressed in terms of this quantity

$$P_{C1} = I_1^2 R_{C1} = P_L R_{C1}\{Z_L^2/(Z_2 + 1)\}^{1/2}/(R_A + R_P) \tag{2.24}$$

$$P_{C2} = I_2^2 R_{C2} = P_L R_{C2} Z_L^2/\{Z_2^2(R_A + R_P)\} \tag{2.25}$$

The losses are then linearly proportional to power; for the typical values cited in this section, the attenuation in is C_1 is 29.97dBm and in C_2 is $30d$Bm. These loss mechanisms are much lower than that of the transmission line connecting the source to the matching network and load. If the load is prefectly matched to the line the attentuation is approximately .182dB or 1.8%for the 8m coaxial cable used (by specification).

As a final note, losses in the coaxial feed between the matching network and the antenna itself must be considered. This is sometimes referred to as coupling efficiency or antenna efficiency, which was first introduced in chapter 1. The antenna efficiency is defined as

$$\eta_A = R_P/(R_A + R_P) \tag{2.26}$$

It is a measure of what fraction of antenna power is coupled to the plasma. In practice R_A represesnts not only the antenna resistance but the resistance of any power feed lines connecting the matching network to the antenna and may be estimated as follows. The skin resistance for a cylindrical conductor may be written as

$$R_{skin} = \rho l \left[\int_{a-\delta_s}^{a} s ds d\theta\right]^{-1} = \frac{\rho l}{(2a - \delta_s)\pi\delta_s} \tag{2.27}$$

where ρ is the resistance of the material, a the outer radius, δ_s the skin depth at the frequency of interest, and l the length of conductor; the integral is just the cross sectional area of the conductor.

The skin depth is given by

$$\delta_s = \sqrt{\frac{2}{\omega\mu\sigma}} \tag{2.28}$$

where ω is the frequency, μ the permability of the material and $\sigma = 1/\rho$ the conductivity of the material. The skin depth for copper at $T = 20°C$, $f_0 = 13.56$MHz is approxmately 17.9μm, yielding surface resistances of 48mΩ and 14mΩ for the inner and outer conductors, respecitvely, of the coaxial power feed line to the antenna which as dimensions $l = 1$m and $a = 1.1$cm. The losses for the coaxial feed then go like $I_L^2 R$ resulting in losses of .288dB or about 6.8% with respect to power delivered to the load; this corresponds to an antenna efficiency of 93.2%. Note that these losses will vary with temperature and frequency. One additional power loss mechanism is the efficiency of the DC to RF conversion (η_{RF}) which we will take to be unity for the laboratory. The determination of efficiency in the laboratory beings after RF power has been generated. This metric does however become relevant in spaceflight applications where additional complexity is needed in power processing units (PPUs), and one must penalize for this power conversion as not all thruster or components will generally require it. The transmission line losses and antenna to plasma coupling efficiency is easliy optimized in spaceflight applications since the thruster and its associated electronics will be compact, alleviating the need for power to be delivered across long lengths. The RF power conversion efficiency may however be optimized through careful design of power processing electronics.

Materials selection and fabrication

Conductive losses in the coaxial power feed and antenna may be minimized with the use of copper interconnects. Copper alloys such as as brass may also be used; performance may be improved if the materials are silver coated. Since the currents travel along a thin layer for any given surface it is important that anodized metals not be used altogether. Whenever other materials must be used (e.g. for electronics packaging and enclosures) aluminum with a chrome finish may be used; this finish prevents the formation of non-conductive oxide layers, which prevent RF currents from penetrating the metal surface. The antenna, coaxial power feed and other interconnects were fabricated with oxygen free copper (alloy 10100), which is better suited for brazing applications. The interconnects are joined using silver brazing alloys (56% Ag, 22% Cu, 17% Zn, and 5% Sn) with a melting temperature of approxmiately 650°; alloys containing nickel are better suited for

brazing copper to stainless steel (e.g. vacuum chamber components).

2.3.2 Magnetic Field Generation

The magnetic fields required for helicon wave propagation and particularly ion confinement are in excess of 1000G. Although plasma density saturates at fields of this order, it is desired to attain fields as high as practically possible for purposes of experimentation in addition to particle confinement, making the use of an electromagnet suitable for this application. The electromagnet consisted of a single air-core solenoid with a length of approximately 12cm, outer radius of 9.5cm and inner radius of 3.5cm. It was fabricated using square cross section copper conductor (66mm $\times$66mm) with polyurethane insulation (rated to 200°C), with 18 turns per layer and 9 layers for a total of 162 turns. Contours of the magnitude of the magnetic field are shown in figure 2-10 while contours of the magnetic flux in are shown in figure 2-11. The contours are in the $r-z$ plane with rotational symmetry in θ; the axis of rotation is the horizontal at the bottom of each figure.

The field strength and shape was verified experimentally using a hall-effect sensor. Several measurements were taken on-axis and these measurements were used in conjuction with a finite element model to produce the field contours of figure 2-10. It was determined from the experimental measurements that the peak field (occuring at the center of the magnet) scaled as 11 Gauss per Ampere. This result combined with knowledge of the geometry allows one to construct the flux contours of the figure, illustrating the lines of force which charged particles will follow. The electromagnet is best suited for testing purposes in a laboratory environment. Generation of comparable fields (1000G-2000G) may be readily achieved using permanent magnets, which are lighter and consume no power. For comparison, the resistance of the above coil is approximately 0.03Ω at $T = 20$°C, yielding a power consumption upwards 500 Watts for fields of 1500G and higher. One final consideration is the rate at which the current is increased or decreased to its final value. The self-inductance of the magnet will generate a large back EMF (potentially damaging power electronics) if care is not taken. That voltage is just $V_b = -L\frac{dI}{dt}$. The inductance of the coil is approximately 120μH, and if it is desired that the backemf remain at 1% of the maximum operating voltage (approximately 6V) then the constraint is that dI/dt remain below 480As^{-1}, a criterion which is easily met in practice.

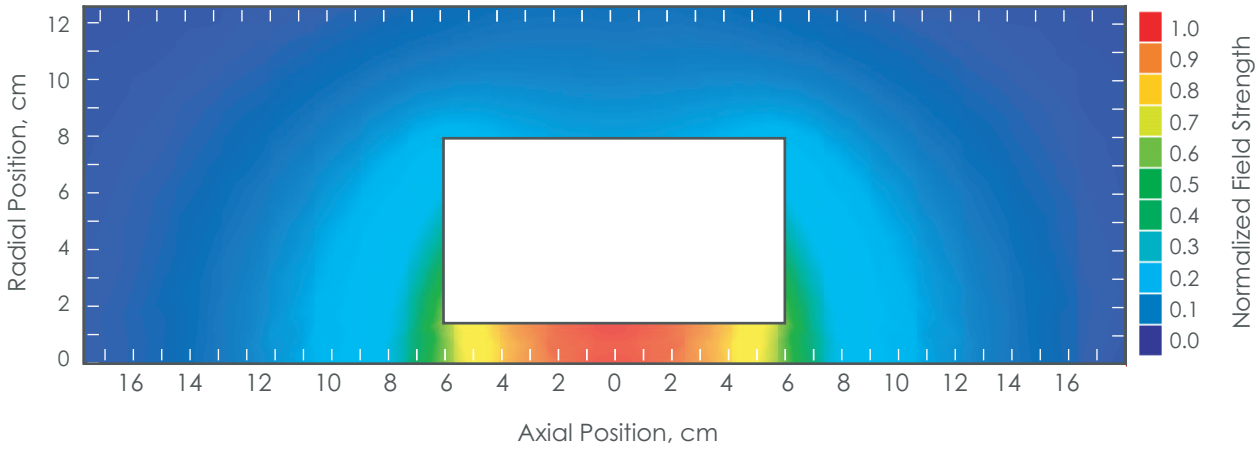

Figure 2-10: Magnetic field contours normalized to peak values. The scaling constant is 11G/A for the peak magnetic field. Coil cross section respresented by the white box, with the axis of rotation being the horizontal at the bottom of the figure.

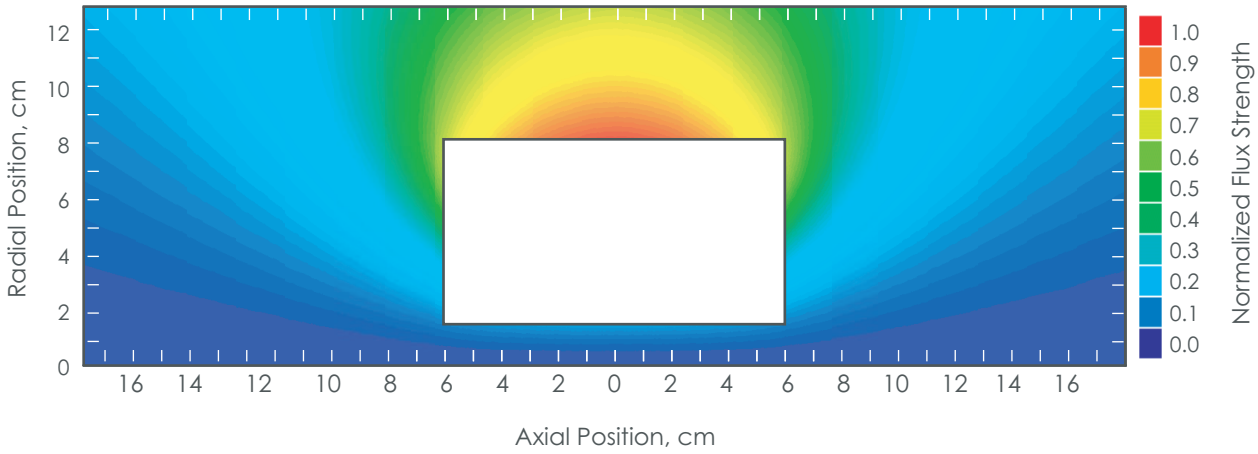

Figure 2-11: Magnetic flux contours normalized to peak values. The scaling constant is 1.07μWb/A for the peak magnetic flux. Coil cross section respresented by the white box, with the axis of rotation being the horizontal at the bottom of the figure.

2.3.3 Neutral gas confinement tube

The gas confinement tube serves to confine neutrals as they enter the ionization region. The cross sectional area of the tube is chosen in correspondence with the desired plasma radius to be 2cm. The cross section should in general vary to accomodate expanding magnetic fields lines. If the tube does not grow to accomodate the plasma the magnetic field lines will intersect the wall and particles following those field lines will be lost. It is for this reason that figure 2-1 incorporates a continuously expanding wall, the profile of which matches the expansion of the field line at 2cm in the ionization region. For practical reasons a tube of this type was not implemented in the laboratory; a tube with constant cross section was used and recessed approximately 3cm with respect to the end of the magnet to minimize the magnetic field line - wall intersection. In addition to the physical dimensions of the tube, one must consider the thermal loading on the tube. In the absence of active cooling, the tube must radiate away heat; the power radiated is given by the Stefan-Boltzman law

$$P = \epsilon\sigma A(T^4 - T_E^4) \tag{2.29}$$

where ϵ is the emissivity, $\sigma \equiv 5.6704\times10^{-8}\mathrm{W/m^2K^4}$ the Stefan-Bolzmann constant, A the radiating area of the body, T and T_E the temperatures of the black body and environment, respectively; T_E is usually taken to be 293°K for the laboratory. The temperature will reach steady state when the radiated power is equal to the power absorbed. One may use the expression for radial power loss to determine this loading, however note that in the derivation of that expression an ion cost of 200eV was assumed, some of which will be radiated away. If the tube is transparent to certain wavelengths of radiation causing the latter to escape. The 200eV estimate per ion then is an upper bound to the energy absorbed by the tube. For the case of $P_\perp \approx 10\mathrm{W}$ at $n_0 = 10^{19}$ with an emissivity of $\epsilon = .8$, the tube will reach a steady state temperature of approximately 400°K. Materials must be chosen to withstand these heat loads, and ceramics are generally a good choice. Quartz is particularly advantageous for laboratory applications since it allows for transmission of light thereby enabling optical diagnosis of plasma parameters. It is however not ideal for spaceflight applications for a variety of reasons. It has a relatively low thermal conductivity ($35\mathrm{W}/m°\mathrm{K}$) which removes the possibility of using the tube itself to extract heat away from the plasma and into a

radiator. Another concern with regard to material properties is the dielectric loss; the coupling between the antenna and the tube may be weak but this factor must be considered nevertheless.

2.3.4 Propellant flow system

The amount of propellant which must be supplied to keep any given discharge fueled was determined in the calculation of radial and axial particle flux. The particle losses illustrated in figure 2.2 may be used to determine the necessary flow rate; the produce of the particle loss and the molecular weight (in grams) is used to determine the mass flow rate. The results suggest that mass flow rates will be of order 1mg/s for Argon. The components comprising the flow system are illustrated in figure 2-12. The propellant is stored in a pressurized tank (typically 2000psi). That pressure is then reduced to approximately $20 - 25$psi so that the flow may be regulated by a mass flow controller. The flow controller consists of a heating element and a pickup coil downstream (neither are shown). The flow is initially heated and the amount of heat transferred to the secondary coil downstream may then be measured. Since the heat transfer is convective the amount of heat transferred is proportional to the flow rate, allowing for a measurement. The flow is sensed using this techniques and controlled using a variable solenoid valve via feedback loop. The ceramic break shown in the schematic is necessary so as to shield the flow control electronics from radio-frequency currents which may be induced on the gas feed lines. The break is comprised of a stainless steel to alumina seal, electrically isolating the stainless steel gas feed lines of the thruster from the flow controller.

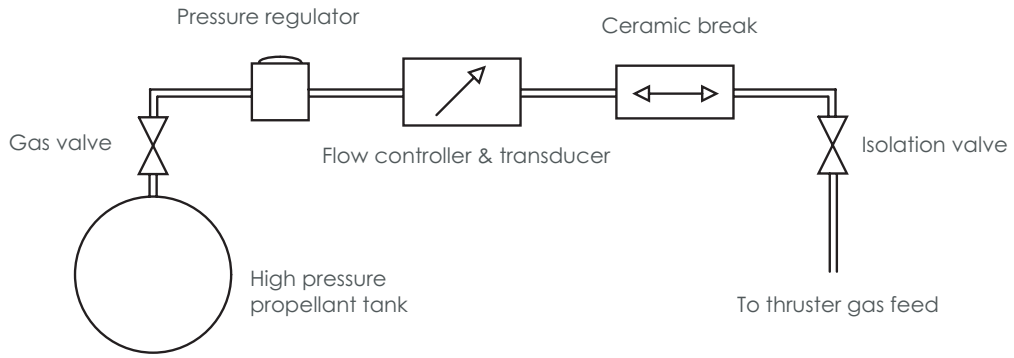

Figure 2-12: Propellant flow system showing valved pressurized tank (typically Argon), pressure regulator, mass flow controller, ceramic break and isolation valve.

Chapter 3

Plasma Jet Energy Measurements

Measurements of the ion energy in the plasma jet reveal a great deal about efficiency and more importantly the amount of ion acceleration. Since it is the goal of this paper to identify potential mechanisms for ion acceleration so that they may be better studied and optimized it is only suitable to begin with a characterization of the ion energy in the plume. The diagnostic methods used for the analysis are presented along with a brief discussion of proper measurement techniques. Ion energy measurements in the plume are presented as a function of magnetic field, power, and propellant flow.

3.1 Diagnostic Methods

It is desired to measure the ion velocities ($T_{i\|}$) far downstream of the thruster so that any potential ion acceleration mechanisms have already come into effect. The measurement of ion velocities in this region of the plume is best accomplished with the use of a retarding potential energy analyzer. The analyzer first repels all plasma electrons and then uses a retarding potential to selectively collect ions; ions with an energy greater than the retarding potential are collected. The retarding potential analyzer thus allows one to probe the ion energy distribution, thereby obtaining a great deal of information with regard to plasma energy content. Knowledge of the distribution function not only allows one to calculate mean ion energies and hence deduce quantities such as I_{sp}, but it also allows one to measure the effective ion temperature, $T_{i\perp}$ from the width of the distribution function. The retarding potential analyzer can also reveal whether there are multiple populations

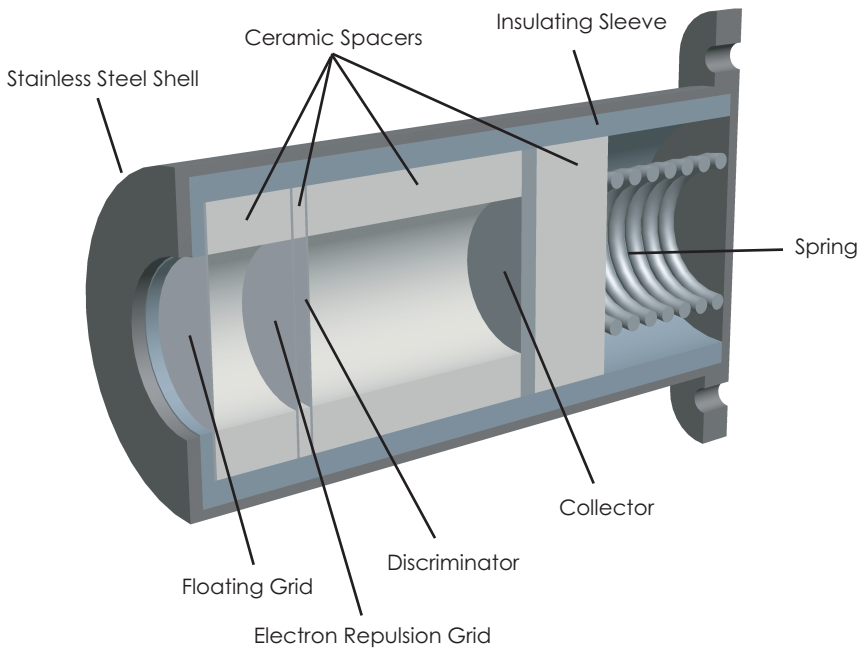

Figure 3-1: Retarding potential analyzer cross-section illustrating floating, electron repulsion and ion retarding grids, collector and the various insulating ceramic spacers used to separate them. Energy analyzer and illustration is based on a design from another work[1]

of ions due to various plasma processes (e.g. charge-exchange, recombination).

The retarding potential energy analyzer used for this measurement is illustrated in figure 3-1; it is based on a design which was experimentally tested against thrusters with well known characteristics[1]. The outer shell of the probe is fabricated with stainless steel. A mica ceramic sleeve fits inside the shell so as to electrically insulate it from the various grids inside. The first grid may in general be grounded or left floating. It is left floating for this particular application so as to provide a more smooth transition in potential from the plasma to the second grid, which is biased negatively to repel all plasma electrons; this tends to perturb the plasma less. The third and final grid, referred to as the ion retarding grid, is biased positively to selectively collect ions. Ions with an energy equal to or greater than the bias on the disriminator may pass, and eventually reach a conducting collector plate. The collector plate may be left floating or biased negatively so as to increase the signal to noise ratio. The energy analyzer achieves a collection angle of 22.8° via small

opening at the inlet, allowing it measure the component of velocity and hence temperature normal to the collecting plate. The grids are composed of 35μm thick molybdenum with a transparency of 72% and the spacers between them were fabricated from mica glass ceramics. The spacing between the electron repulsion and ion retarding grids was adjusted and verified to be less than a few debye lengths so that the space-charge limit is not reached when extracting ion current from the grid; the spacing between the grids (from left to right, as shown in figure 3-1) is 3.35mm, 1.07mm, and 9.85mm. The opening into the energy analyzer is approximately 6.35mm and the collector has a diameter of approximately 1cm. The reader is referred to the reference[1] for further detailed design information with regard to the energy analyzer. The probe is operated with a fixed bias voltage on the electron repulsion grid and collector; the retarding grid bias is swept while simultaneous measurements of the ion current are performed on the collector. The current collected for each value of retarding grid bias then includes all ions with a directed energy greater than or equal to that bias; the current collected is

$$I_c = \phi^3 e n_0 A_c \langle v_i \rangle \tag{3.1}$$

where n_0 is the density of ions incident on the collector, A_c the area of the collector, ϕ the grid transparency and $\langle v_i \rangle$ the average velocity of the ions collected. The average ion velocity may be expressed in terms of the ion energy distribution function

$$\langle v_i \rangle = \int_{v_d}^{\infty} v f(v) dv \tag{3.2}$$

where v_d is the ion velocity corresponding to an energy equal to that of the retarding grid. The relationship is simply

$$\frac{1}{2} m_i v_{\parallel}^2 = \frac{1}{2} K T_i = e V_{bd} \tag{3.3}$$

with v_d being the ion velocity and $V_b d$ the bias on the retarding grid. In a strong magnetic field it is appropriate to use the one-dimensional Maxwellian for the energy distribution function, which in normalized form may be written as

$$f(v_{\parallel}) = \left(\frac{m_i}{2\pi K T_i}\right)^{1/2} \exp\left[-\frac{1}{2} m_i v_{\parallel}^2 / K T_i\right] \tag{3.4}$$

where the parallel and perpendicular subscripts are explicitly noted to avoid confusion. Note that experimental measurements may be performed in regions of negligible magnetic field, however the ion velocities in these regions are strongly directed by acceleration mechanisms and the flow may nevertheless be considered one dimensional. Combining equations 3.1, 3.2 and 3.4 one obtains

$$I_c = \phi^3 A_c e n_0 \int_{v_d}^{\infty} \left(\frac{m_i}{2\pi K T_i}\right)^{1/2} v \exp\left[-\frac{1}{2} m_i v_{\parallel}^2 / K T_i\right] dv \tag{3.5}$$

The integrand may be expressed in terms of the retarding grid bias voltage; the change of variables required may be accomplished with the use of equation 3.3. The result is

$$I_c = \phi^3 A_c e n_0 \int_{V_{bd}}^{\infty} \frac{e}{m_i} \left(\frac{m_i}{2\pi K T_i}\right)^{1/2} \exp[-e V_{bd} / K T_i] dV \tag{3.6}$$

The derivative of both sides of the above expresion yields

$$dI_c / dV_{bd} = \phi^3 \frac{A_c n_0 e^2}{m_i} \left(\frac{m_i}{2\pi K T_i}\right)^{1/2} \exp[-e V_{bd} / K T_i] \tag{3.7}$$

which is proportional to the ion energy distribution function. Thus, measurements of collector current against retarding grid bias may be used to deduce the axial ion energy as well as the temperature. Note that density measurements are unnecessary for the determination of those two parameters, since they are extracted from the exponential portion of equation 3.7. Knowledge of the local plasma density may be used to deduce the height of the distribution and hence the particle flux.

3.2 Measurement Techniques

Measurement of the ion energy distribution function is accomplished as noted earlier; the electron repulsion grid and collector are held at a constant bias voltage meanwhile the retarding voltage is swept and current collected simultaneously. The determination of repulsion grid and collector bias voltage depend on the type of plasma being probed and the environment in which the probe is operating. It is not uncommon for helicon sources to require repulsion grid voltages with magni-

tudes on the order of several tens of volts usually somewhat higher than that of simple inductively or capacitively coupled plasmas. The reason for this the strong local antenna fields which drive electrons in a periodic motion along the thruster axis. The required voltages were found by experimental investigation. The thruster was operated with typical discharge parameters ($B_0 = 1500$G, $P = 690$W coupled to plasma, and a gas flow rate of .548mg/s of Argon) and several I-V curves were obtained for various electron repulsion grid voltages (with no bias on the collector) as shown in figure 3-2. If the repulsion voltage is not large enough, some electrons will penetrate the grid and subtract from the overall ion current. If the magnitude of the voltage is too high ions may be artificially accelerated. The ions are of course always accelerated as they approach the grid and then decelerated, but if the voltage is too negative the sheath the repulsion grid may expand and overlap with the sheath on the retarding grid, not allowing the ion to be fully decelerated as it passes through the repulsion grid. The latter effect however adds an offset to the measurement and may be readily subtracted from the data gathered in postprocessing. An electron repulsion grid voltage greater than 65 in magnitude proved to be sufficient for the range of plasma parameters which were swept. The effects of collector bias were then investigated, as shown in figure 3-3; the effect is to enhance the current signal. The measured curves of collector current vs. retarding potential, such as those illustrated in figures 3-2 and 3-3, are fitted to a smoothing spline so as to minimize any noise which is generated when discrete derivatives would otherwise be taken. The smoothing spline $s(x)$ is defined by

$$p\sum_i (y_i - s(x_i))^2 + (1-p)\int \left(\frac{d^2 s}{dx^2}\right)^2 dx \tag{3.8}$$

where y_i and x_i are the discrete indepdendent and dependent variables, respectively, and p a user-defined fitting parameter. The value of p is manually adjusted to obtain a smooth spline without compromising critical features (e.g. adjusted to filter out noise without losing or merging peaks). Once the smoothing spline function is found, its first derivative is taken resulting in a function proportional to the ion energy distribution function.

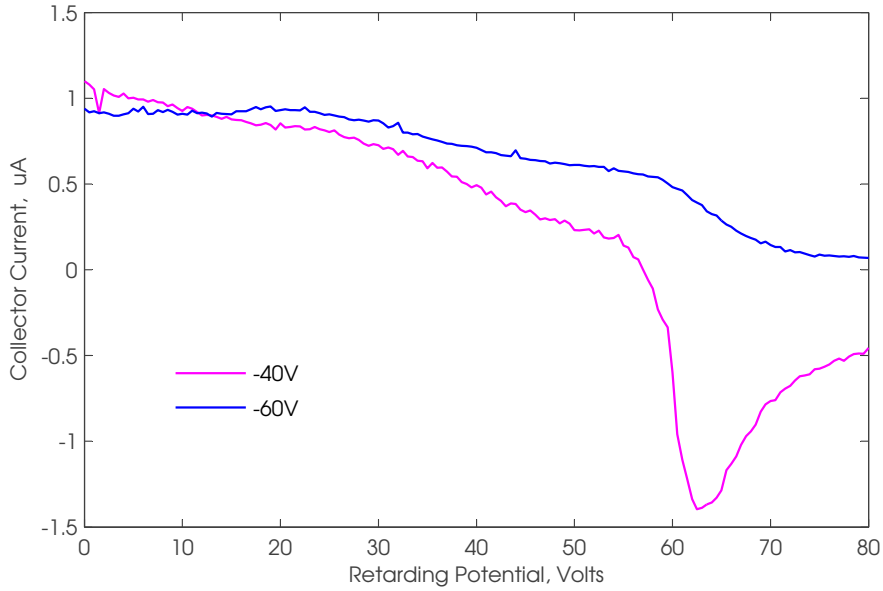

Figure 3-2: Ion current vs. retarding grid bias voltage (smoothed data) for electron repulsion grid voltages of -40V and -60V. The curves are for a discharge with $B_0 = 1500$G, $P = 690$W and a gas flow rate of .548mg/s of Argon.

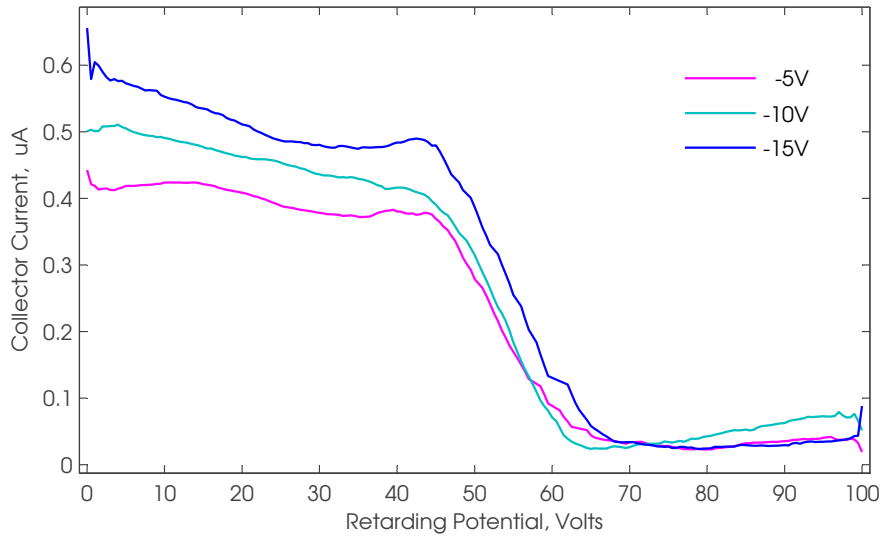

Figure 3-3: Ion current vs. retarding grid bias voltage (raw data) for various collector bias and electron repulsion bias of -60V, $B_0 = 1540$G, $P = 735$W and a gas flow rate of .548mg/s of Argon.

3.3 Ion Energy Measurements

The axial ion energy in the plasma jet was measured with the retarding potential analyzer described above. The energy analyzer was placed approximately 40cm downstream of the exit plane on the thruster's central axis. Experiments were performed with Argon propellant for various powers (magnetic field and flow rate held constant), various magnetic fields (flow rate and power held constant) as well as for various flow rates (magnetic field and power held constant). In addition, the magnetic field was turned off (with the remainder of the experimental setup unchanged) so as to determine the differences in ion energy when the helicon wave does not propagate. Some experiments with Nitrogen were also performed so as to check for consistency.

3.3.1 RF Power Scans

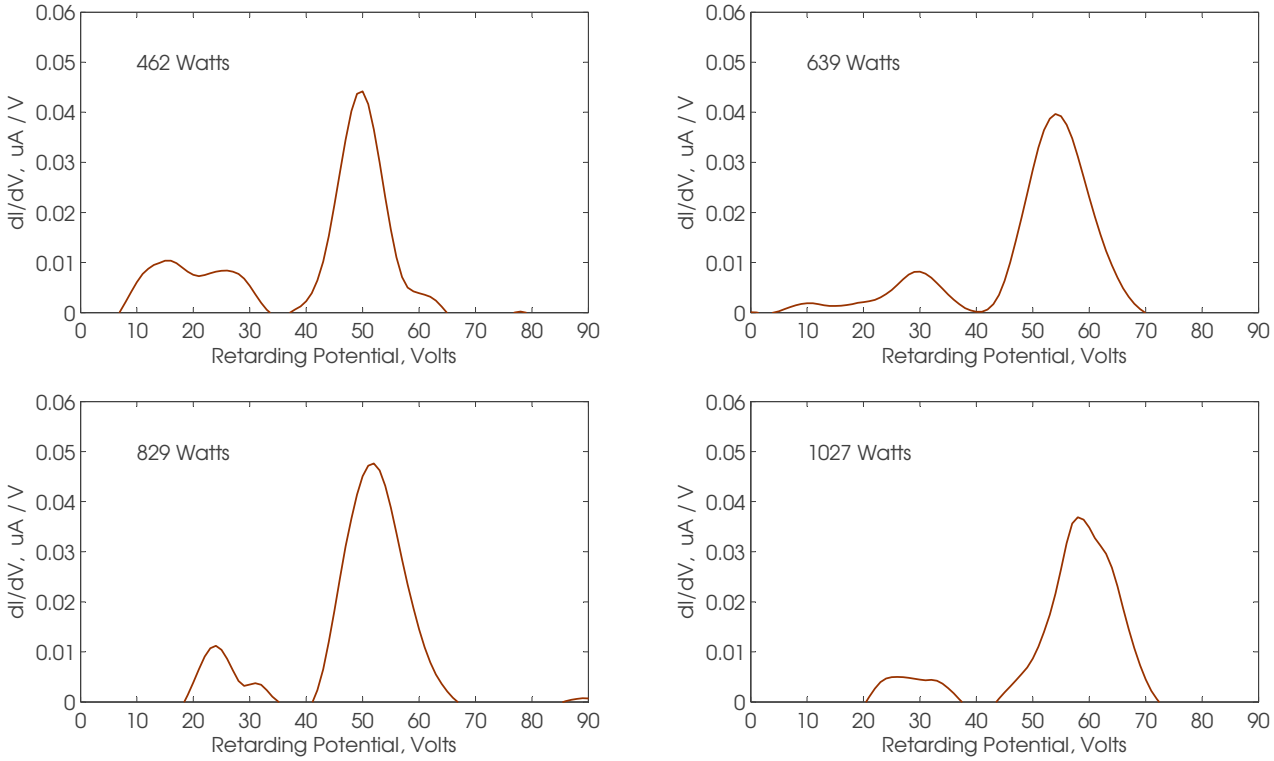

Figure 3-4: Ion energy distribution functions for various power delivered to plasma (loss mechanisms are accounted). Discharge parameters were $B_0 = 1500$G and a Acquisition parameters were a voltage step of $1V$ every 250ms with an electron repulsion bias of -65V and a collector bias of -20V. The retarding voltage is specified with respect to ground.

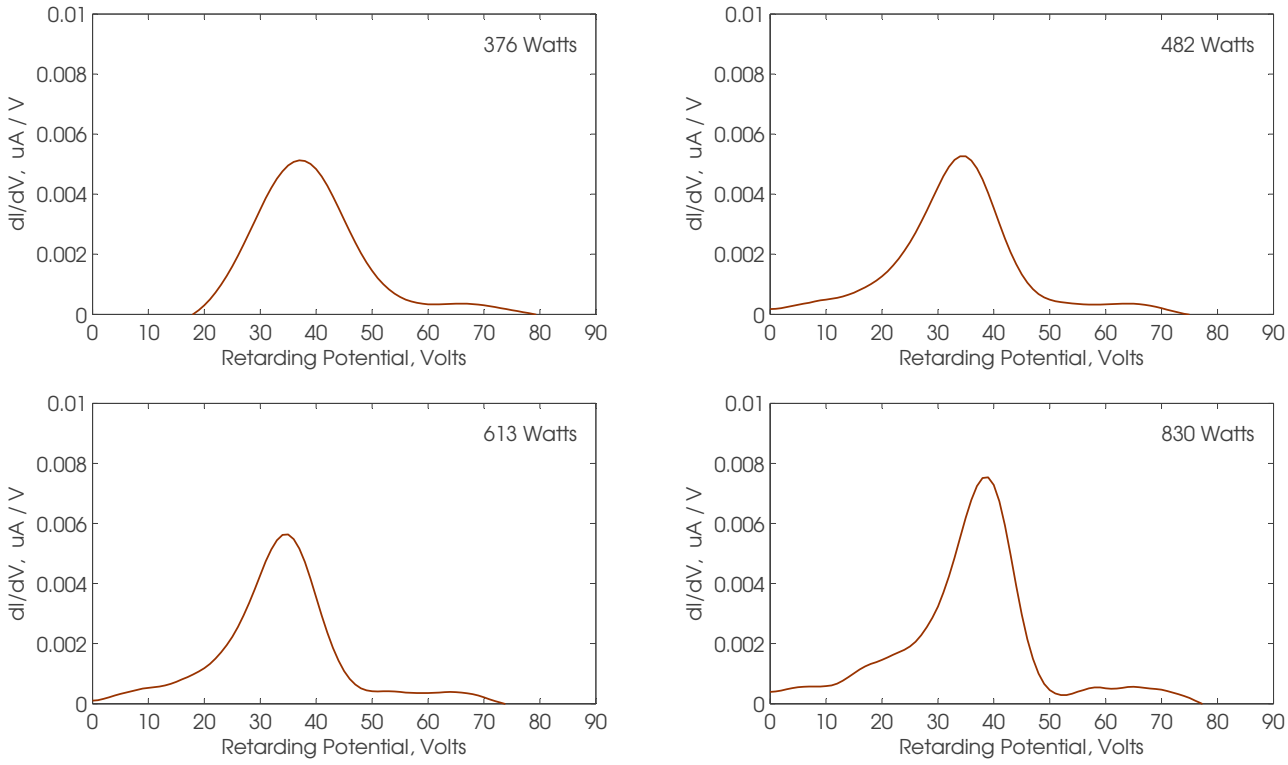

Figure 3-5: Ion energy distribution functions for various power delivered to pure inductively coupled plasma ($B_0 = 0$) for a gas flow rate of .548mg/s of Argon. Acquisition parameters were a voltage step of $1V$ every 200ms with an electron repulsion bias of -65V and a collector bias of -20V. The retarding voltage is specified with respect to ground.

3.3.2 Magnetic Field Scan

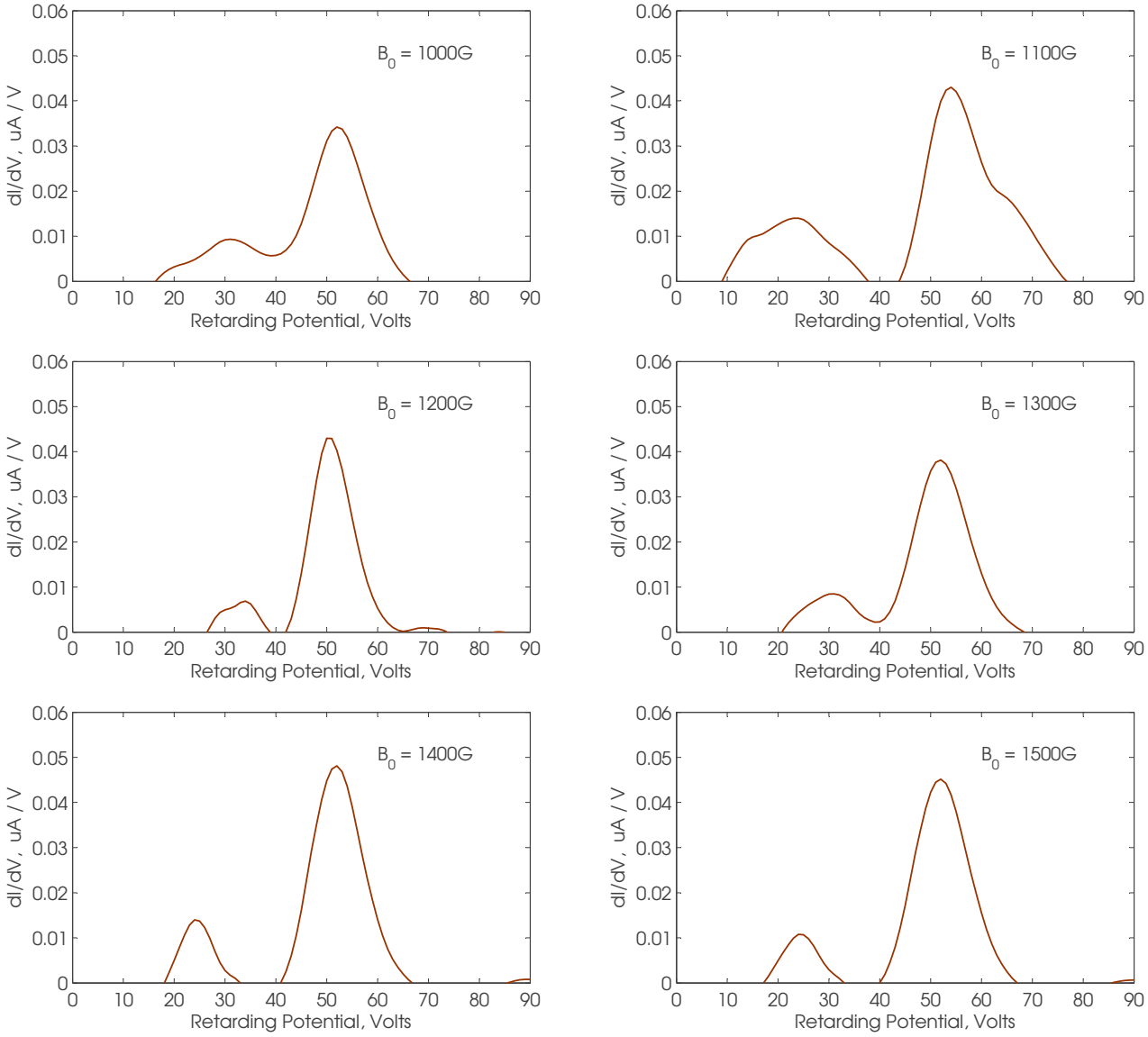

Figure 3-6: Ion energy distribution functions for peak magnetic field values in the range of 1000G to 1500G. Discharge parameters were $P = 830$W and a gas flow rate of .548mg/s of Argon. Acquisition parameters were a voltage step of $.5V$ every 250ms with an electron repulsion bias of -65V and a collector bias of -20V. The retarding voltage is specified with respect to ground.

3.3.3 Gas Flow Rate Scans

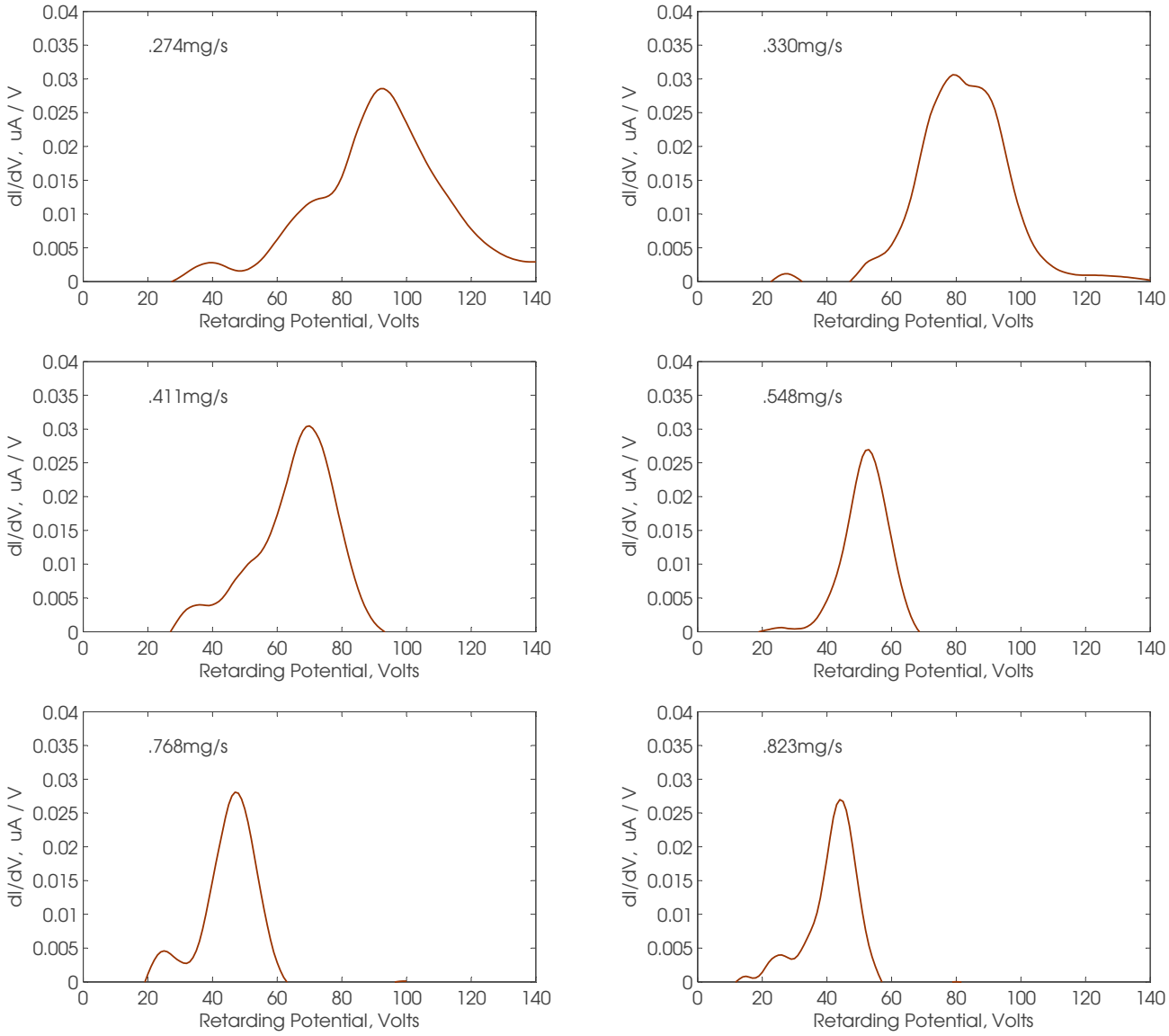

Figure 3-7: Ion energy distribution functions for various flow rates of Argon (mg/s) as indicated on each plot. Discharge parameters were $P = 640$W and $B_0 = 1500$G. Acquisition parameters were a voltage step of $1V$ every 250ms with an electron repulsion bias of -65V and a collector bias of -20V. The retarding voltage is specified with respect to ground.

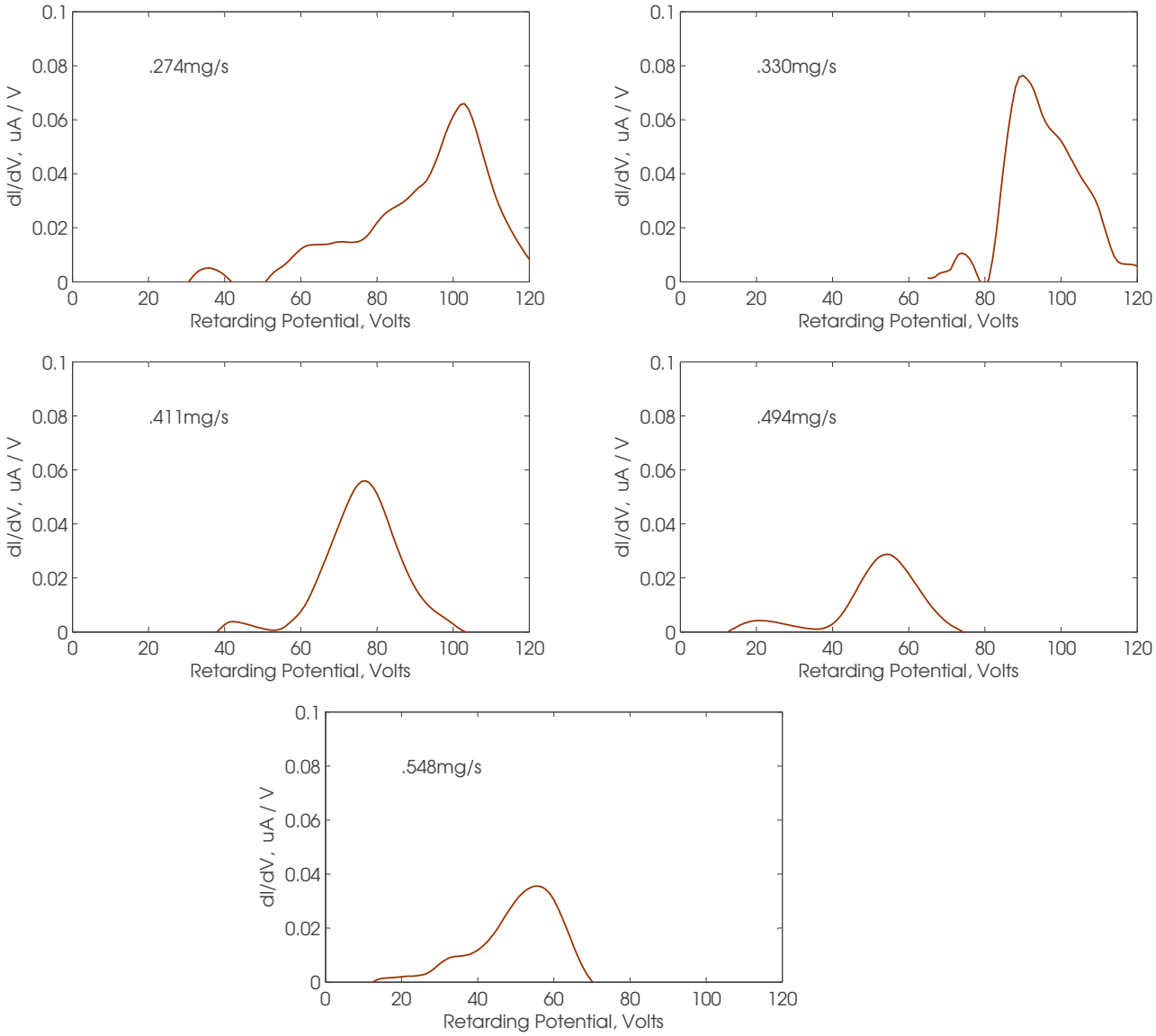

Figure 3-8: Ion energy distribution functions for various flow rates of Argon (mg/s) as indicated on each plot. Discharge parameters were $P = 1010$W and $B_0 = 1500$G. Acquisition parameters were a voltage step of $1V$ every 250ms with an electron repulsion bias of -65V and a collector bias of -20V. The retarding voltage is specified with respect to ground.

3.3.4 Nitrogen Power and Gas Flow Scans

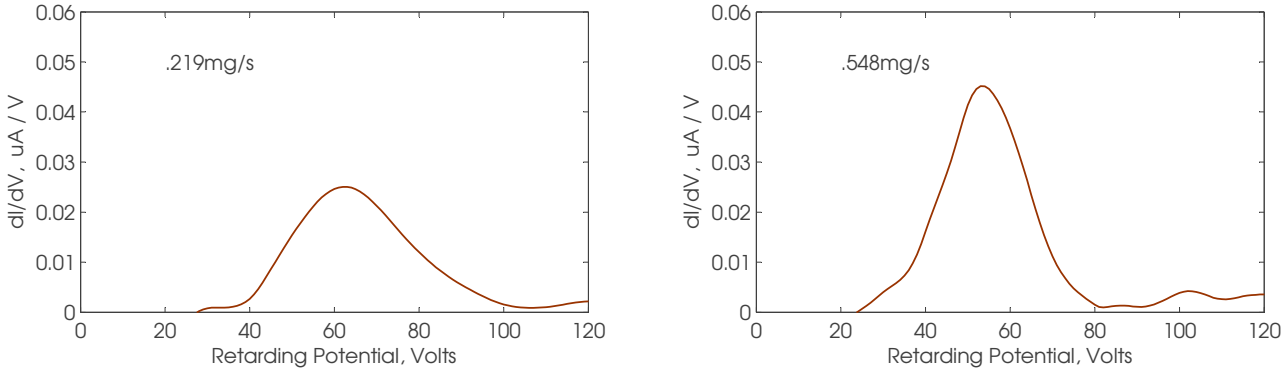

Figure 3-9: Ion energy distribution functions for various flow rates of Nitrogen (mg/s) as indicated on each plot. Discharge parameters were $P = 665$W and $B_0 = 1500$G. Acquisition parameters were a voltage step of $1V$ every 250ms with an electron repulsion bias of -65V and a collector bias of -20V. The retarding voltage is specified with respect to ground.

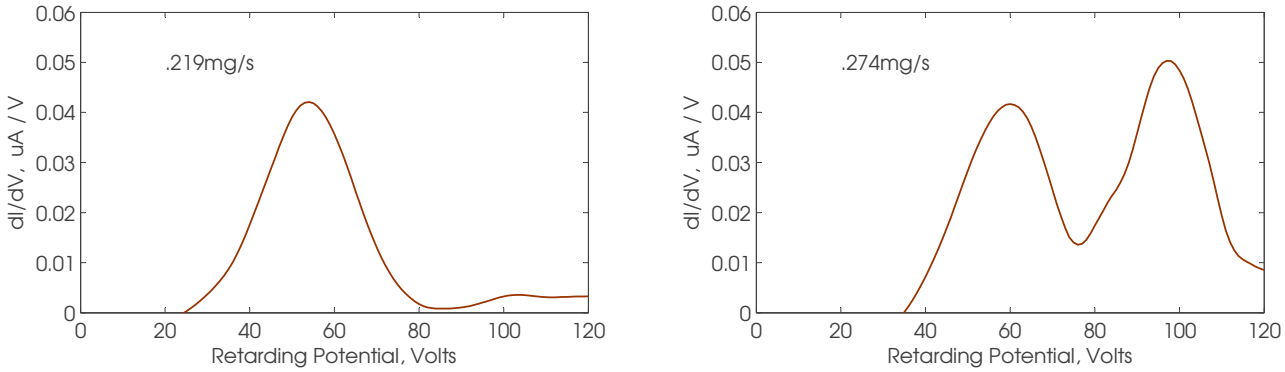

Figure 3-10: Ion energy distribution functions for various flow rates of Nitrogen (mg/s) as indicated on each plot. Discharge parameters were $P = 855$W and $B_0 = 1500$G. Acquisition parameters were a voltage step of $1V$ every 250ms with an electron repulsion bias of -65V and a collector bias of -20V. The retarding voltage is specified with respect to ground.

3.4 Summary of Results

The energy analyzer measurements indicate a significant amount of ion acceleration by the plasma. The measurements include an ion free fall across a voltage equal to the plasma potential, which was measured to be approximately 28V. This is because the energy analyzer is biased with respect to the ground; this is the same reference point for the plasma which is above ground by the plasma potential V_p. Nevertheless, it is clear that the plasma itself is able to accelerate ions by as much as approximately 60eV.

The various scans show insensitivity to variations in power and magnetic field as illustrated in figures 3-4 and 3-6. As a consistency check, the magnetic field was turned off and a power scan recorded as illustrated in figure 3-5. It is clear that the helicon mode of operation gives rise to a considerable amount of ion acceleration than one would otherwise obtain. The mean ion energy in the pure inductively coupled mode is slightly higher than the plasma potential. Note that the full width of the distribution functions at half maximum correspond to the total ion energy given as $3/2KT_i = KT_{i\perp} + 1/2KT_{i\|}$. As a further consistency check, one may subtract the plasma potential (shift the curves to the left) and then extract the perpendicular temperature from the width and the mean ion energy of the distribution, and this leaves a $T_{i\perp}$ of order 1eV, as expected. The plasma potential must be subtracted there since the free-fall ions undergo as they enter the energy analyzer is not part of the statistical mechanics which gives rise to the Maxwellian distribution. Plasma potential measurements local to the energy analyzer were not taken since it is difficult to extract a value with any precision, particularly in an RF plasma.

A population of low-energy ions is observed in the the energy distribution functions, particularly notable in the magnetic field scan of 3-6 and the power scan of 3-4. There are several possibilities for the presence of these peaks. One might suggest that the magnetic field lines just downstream of the discharge region intersect the walls of the gas confinement tube, causing a population of ions to recombine there and then to re-ionize and accelerate outward with lower energy. This would suggest some sensitivity to magnetic field which is not observed in figure 3-6. Furthermore, the results of the following section will show that a majority of the acceleration occurs just downstream of where the gas confinement tube ends, meaning that if this were the case then the energy difference between the minority and majority peaks would be of order 5eV.

It is noted that the energy is particularly sensitive to the mass flow rate. There exists a regime

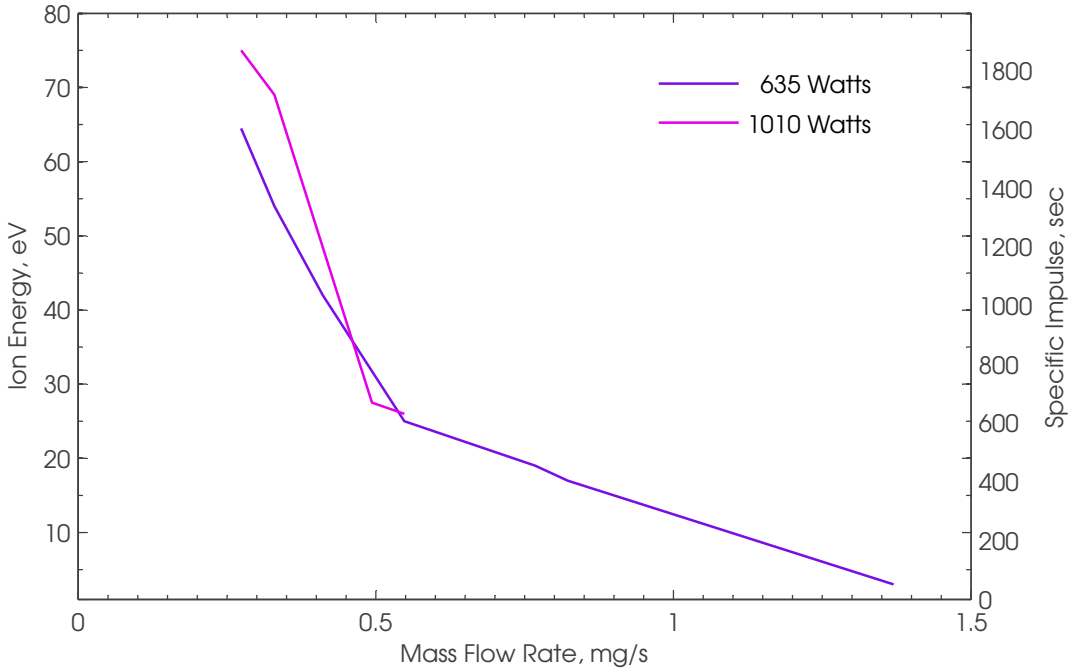

Figure 3-11: Mean ion energy and corresponding specific impulse for the flow rate scans of figures 3-7 and 3-8. The peak magnetic field was held at $B_0 = 1540$G.

for the case of low flow rates where the acceleration mechanism is particularly strong. The mean ion energy calculated from the distrubtion and the corresponding specific impulse is illustrated in figure 3.4. The results of that figure are corrected for the plasma potential (taken to be approximately 28V).

Finally, experiments with nitrogen illustrated in figures 3-9 and 3-10 demonstrate sensitivity to flow rate as well. Nitrogen is more complicated as a propellant since as a diatomic molecule it posses various modes of energy storage; one may create molecular ions as well as atomic ions by first putting in enough energy to dissociate the molecule. This is thought to be the cause behind the double peaks sometimes seen in 3-10.

Chapter 4

Particle Flux Measurements

The energy measurements of the previous section revealed the presence of strong ion acceleration mechanisms. Those measurements were performed well downstream of the nozzle at which point whatever mechanism responsible for ion acceleration had fully developed. In support of these findings, ion flux measurements were performed near the exit plane of the thruster in an attempt to determine the physical location at which the majority of ion acceleration occurs. Plasma density, electron temperature and the mach number of the flow were measured for various gas flow rates and power coupled to the plasma.

4.1 Diagnostic Methods

The Mach number of plasma flow both parallel ($M_{\|}$) and perpendicular ($M_{\perp}$) to magnetic field lines can be measured with the use of a Mach probe. The Mach probe typically consists of several current collecting electrodes surrounded by an insulator. The idea behind Mach number measurements with such probes is to insert into the flow an insulating solid body (this is the probe body, usually constructed of high temperature resistant materials) so as to create a perturbation of the flow around the probe. The asymmetry of the flow across the the upstream and downstream sides of the probe may then be exploited; electrodes are used to separately collected ions on either side of the probe. In a flowing plasma the electrode on the upstream side of the probe will measure a greater current than the electrode on the downstream side, and the ratio of these two currents is a function of the Mach number. Theory and a significant amount of modeling can be used to correlate the

Mach number far from the probe with the ratio of the measured currents at the probe itself. The Mach probe used in the present work is illustrated in figure 4.1.1; it is one possible implementation of this diagnostic.

4.1.1 Theory of Operation

The dimensions of the probe are essential in linking the experimental measurement with theory. The relevant dimension is the width, a, of the face of the probe (the insulating perturbing body, not the electrodes themselves) facing the flowing plasma. There exist three regimes of operation: the plasma is considered strongly magnetized for $a \gg r_L$, the ion gyroradius, weakly magnetized for $a \sim r_L$ and unmagnetized for $a \ll r_L$. Considerable theoretical and numerical modeling has been done for probes in magnetized plasmas, and there is good correlation between theory and experiment[26, 27]. The larmor radius for ions (in centimeters) is given by

$$r_L = 102\mu^{1/2}Z^{-1}T_i^{1/2}B^{-1} \tag{4.1}$$

where μ is the ratio of the ion to proton mass, Z the charge number (degree of ionization), B the magnetic field (in units of Gauss), T_i the ion temperature (in units of eV) and r_L the larmor radius in centimeters. One must apply the appropriate theoretical framework to experimental data depending on the regime of probe operation or alternatively design the probe such that the regime of operation is what one desires. Near the exit plane of the thruster, the magnetic field is at least 1200G and T_i at most 0.5eV, yielding a larmor radius of 4.5mm for Argon; the discussion of the probe theory is restricted to the magnetized case. In a magnetized plasma, the particle motion perpendicular to the magnetic field lines is negligible as the larmor orbits are much smaller than the probe. Kinetic models, particle-in-cell computer simulations and laser induced florescence experiments have all shown that a one-dimensional fluid treatment accurately models the physics for subsonic flows[28, 26]. The results of a fluid theory provide a practical formula for interpreting probe data and are summarized here[26, 27]. The fluid dynamics in the probe region are governed

by the following equations

$$\nabla \cdot (n_i \mathbf{v}) = 0 \tag{4.2}$$

$$\nabla \cdot (n_i m_i \mathbf{v} \nu_{\|}) - \nabla \cdot (\eta \nabla \nu_{\|}) + \nabla_{\|} p_i - Z e n_i \mathbf{E}_{\|} = 0 \tag{4.3}$$

$$n_i \mathbf{v}_{\perp} + D \nabla_{\perp} n_i = 0 \tag{4.4}$$

$$\nabla_{\|} p_i = \gamma \; T_i \nabla_{\|} n_i \tag{4.5}$$

The ion continuity and parallel momentum equation with convective, viscosity, pressure, and electric field terms are accounted in equations 4.2 and 4.3, respectively. We consider a plasma flowing in steady state so that $\partial/\partial t = 0$ everywhere. The electric field in equation 4.3 can be determined if one assumes that electrons are isothermal and have negligible inertia. One can then solve the Boltzmann relation for the electric field

$$\mathbf{E}_{\|} = -\nabla_{\|} (T_e/e) \; ln(n_i/n_{\infty}) = -(T_e/e n_i) \nabla_{\|} n_i \tag{4.6}$$

Since the ion larmor radius is much smaller than the transverse probe dimension the dominant mechanism for perpendicular momentum transfer is diffusion. It is for this physical reason that a perpendicular diffusion equation replaces the usual perpendicular momentum equation in 4.4. Thermal effects are accounted for in equation 4.5 where the simplifying assumption is made that ions are isothermal. The set of equations do not, in general have a closed-form solution; they are non-dimensionalized and solved using numerically. The solution can then be fit to a functional form, yielding a practical formula for probe data interpretation

$$M_{\|} = M_c \; ln(I_u/I_d) \tag{4.7}$$

where it is defined that $M_{\|} = v_f/c_s$, with $c_s \equiv [(T_i + T_e)/m_i]^{1/2}$, v_f is the plasma flow velocity (parallel to the field), $I_{u,d}$ the respective upstream and downstream currents and M_c the calibration factor. Fluid theory predicts the formation of shocks (discontinuities of physical quantites in the probe region) for the case of supersonic flows and then the fluid theory is no longer applicable. Kinetic models have been developed to extend the theoretical framework to supersonic flows and provide correspondence with the fluid theory for the case of subsonic flows[29]; the reader is referred

to the reference for details with regard to that work. The kinetic results have the same functional form as 4.7, however with different calibration constants. The results may be expressed as

$$M_{\parallel} = \frac{1}{K}\, ln(I_u/I_d) \tag{4.8}$$

with calibration constant K. In this case that constant is sensitive to the ratio of ion and electron temperatures; K was computed to be 1.3, 1.7, and 1.9 for $T_i/T_e = 2.0$, 1.0, and 0.2, respectively. It should also be noted that the sound speed is defined as $c_s \equiv (T_e/m_i)^{1/2}$[29]. The mach number of the flow may thus be determined with the use of simple flux measurements. If the electron temperature is known then the absolute ion velocity may be determined as well; this suggests the use of a langmuir probe. One possibility is to treat each side of the mach probe as a separate langmuir probe. The voltage on each electrode may then be swept while current is simulataneously recorded resulting in the familiar characteristics which may be used to determine temperature. This approach was not adopted in the present work because the upstream and downstream sides of the probe will yield two different measurements of temperature and density; those measurements must be reconciled with the use of probe theory. The theoretical framework for this does indeed exist for the case of unmagnetized flows but even then one requires knowledge of the plasma potential which is not easily measured[30]. The measurements were taken separately; the mach probe was first used to collect ion current and was then replaced with a simple langmuir probe for the measurement of electron temperature and plasma density. In the limit of negligible debye length compared to probe radius ($\lambda_D \ll a$) the relationship between the Langmuir probe I-V characteristic and the electron temperature may be written as

$$T_e = e(I - I_{si})/\frac{dI}{dV} \tag{4.9}$$

where I_{si} is the ion saturation current where it is acknowledged that the result is accurate to within $10 - 20\%$ in the presence of a magnetic field[26]. Once the temperature is found the density may be extracted from the ion saturation current in the usual manner,

$$I_{si} = enAc_s = enA(T_e/m_i)^{1/2} \tag{4.10}$$

where A is the projection of the area of the electrodes on the magnetic field, T_e the electron

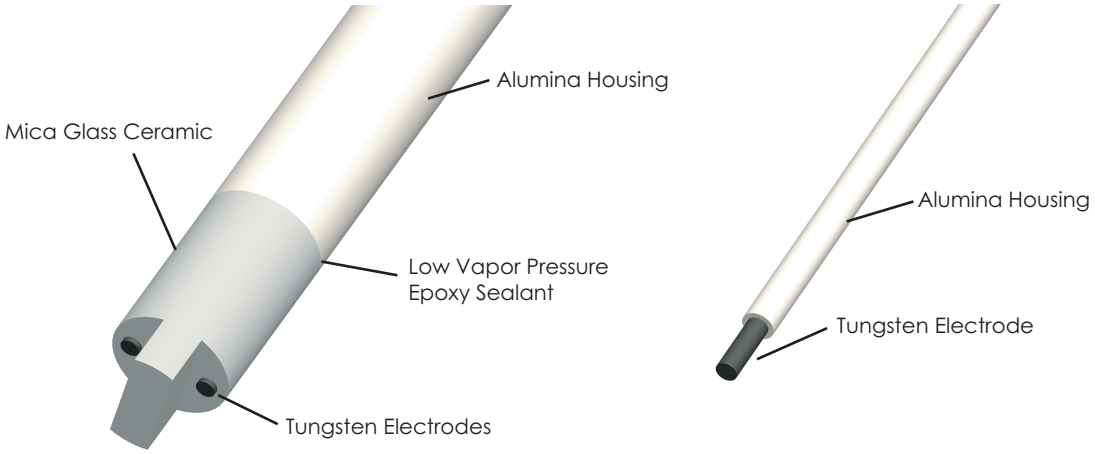

Figure 4-1: Construction of Mach probe (left) and Langmuir probe (right) used for plasma density, temperature, and flow measurements.

temperature as found from equation 4.9, and n the plasma density far from the probe.

4.1.2 Probe Design Considerations

Geometrical symmetry about the centerline of the probe (this is the line along the center of the probe which is normal to the flow) is important as the validity of the fluid and kinetic theories rely on this presumption. As mentioned earlier, the width of the probe facing the plasma (typically the radius for cylindrical probes) is the only important dimension as it determines the regime of operation. The detailed geometry of the probe, such as the collection area of the electrodes, the height of the center protrusion, or the length of the probe itself are only qualitatively important. The electrodes should be well below the top surface of the protrusion so that particle collection is in fact directional (so that the measurement occurs in a region where the plasma flow is in fact perturbed); this vertical distance should be greater than the larmor radius for operation in the magnetized regime. The probe was constructed with a body diameter of 6.35mm, electrodes with diameters of 1.01mm and 1.00mm and current collection heights above the body of 0.26mm and 0.32mm on the upstream and downstream sides of the flow, respectively. The Langmuir probe was constructed with an electrode diameter of 0.5mm and a current collection height of approximately

1.62mm.

The probes should be constructed of high-temperature resistant materials so that they are able to withstand exposure to a hot flowing plasma. Machineability of the material is also of concern as it may be difficult to fabricate a mach probe with the features shown in figure 4.1.1. High temperature glass-mica ceramic was chosen for the body of the mach probe; it has a low dielectric constant ($\epsilon/\epsilon_0 = 6$), low thermal conductivity ($\kappa = 1.5 W/m{\cdot}\mathrm{K}$), a melting point of 1033K, and is generally easy to machine using Tungsten carbide tools. An alumina tube was used to insulate the remainder of the electrodes of both the mach and langmuir probes from the plasma. The electrodes for both probes were fabricated from Tungsten for good electrical conductivity and thermal properties (melting point of 3673K) and low vapor pressure vacuum epoxy was used to bond the electrodes to the probe bodies.

4.2 Circuit Techniques and RF Compensation

The mach probe measurements are achieved by biasing both the upstream and downstream electrodes with a sufficiently negative voltage so as to collect ion saturation current. The voltage on the probes was initially swept to determine a suitable negative bias; at a voltage of -40V the probe was well in the ion saturation region and this bias was used thereafter. The langmuir probes were generally swept from the ion saturation region the electron saturation region, typically spanning a voltage from -60V to 80V with respect to ground. One possible implementation of the circuitry needed for this kind of functionality is illustrated in figure 4.2. A waveform generator is used to output a symmetric ramp in voltage between -5V and $5V$. That signal is amplified approximately 20 times with the non-inverting composite amplifier formed by $A1$ and $A2$. $A1$ is an operational amplifier driver, typically powered between ± 15V whereas $A2$ is a high voltage amplifer capable of rail-to-rail voltage swings of ± 150V. The gain of the composite amplifier is set by R_I and R_F to be approximatley 21, and the gain of the second stage is set by R_G and an internal feedback resistor (internal to the IC) to be approximately 10.7. The overall gain of 20 is suitable as it is desired that small signals (± 5V) drive the probe tip between -60V and 80V, for instance. The gain of the second stage is chosen to be large enough to accomodate the relatively small output swings of the driver; this leaves the driver with a gain of approximately 2, requiring maximum output swings of

$\pm$10V. R_{CL} is a current limiting resistor for the second stage, chosen for a current limit of 600mA. C_C is a compensation capacitor for $A2$, part of an internal compensation network for stability; with a gain of 10 or equivalently 20dB, the second stage has a bandwidth of approximately 300kHz and a phase margin of about 110 for a compensation capacitor of 22pF. Since the driver will have a gain of at least 100dB with a gain-bandwidth product of approximately 1Mhz, compensation on the major loop will likely be required for stability. The open-loop frequency response and the closed-loop step response of the system without any compensation on the major loop (less C_F) is illustrated in figure 4.2; the system has a bandwidth of 340kHz, just 43° of phase margin and exhibits an overshoot of 25% in the step response. For optimum stability a driver with low gain-bandwidth product should be used; this makes compensation easier however it is a tradeoff of speed for stability. A simple lag compensation network may be used in the feedback path to further increase stability in exchange for bandwidth. The capacitor C_f is chosen to be approximately 20pF, leading to a phase margin of 66°, an overshoot of 8% in the step response and comparable bandwidth. The degree of stability is important for this application more so than bandwidth; if the bias voltage on the probe is stepped gradually, ringing on the line will lead to erraneous measurements of both voltage and current. The dynamic tracking error which is a result of low loop gain (a compromise for stability) is not as critical for this application as the voltage may be monitored with a simple resistive divider, which is the purpose of R_1 and R_2 in the schematic.

The composite amplifier is able to drive several sources as it can sink or source several hundreds of milliamps. One measurement channel for a probe is illustrated in the schematic of 4.2. The measurement involves the use of a current sense resistor and a difference amplifier. The difference amplifier used for this particular application attenuates the signal at the input to bring it within the common-mode input range of the amplifier and uses high-common mode rejection to remove the unwanted common mode voltages (which may be as high as 100V for this particular application); the differential portion of the signal is then re-amplified by the same amount it was originally attenuated. The size of the current sense resistor is a tradeoff between sensitivity and dynamic range; since the input of the difference amplifier can accomodate some fixed range of voltage, larger values of resistance will will lead to greater sensitivity but lower dynamic range. Finally, the high frequency bypass capacitors C_3 provide some noise immunity in addition to the power-supply rejection provided by the amplifier itself; C_1 and C_2 perfom the same function for the power rails.

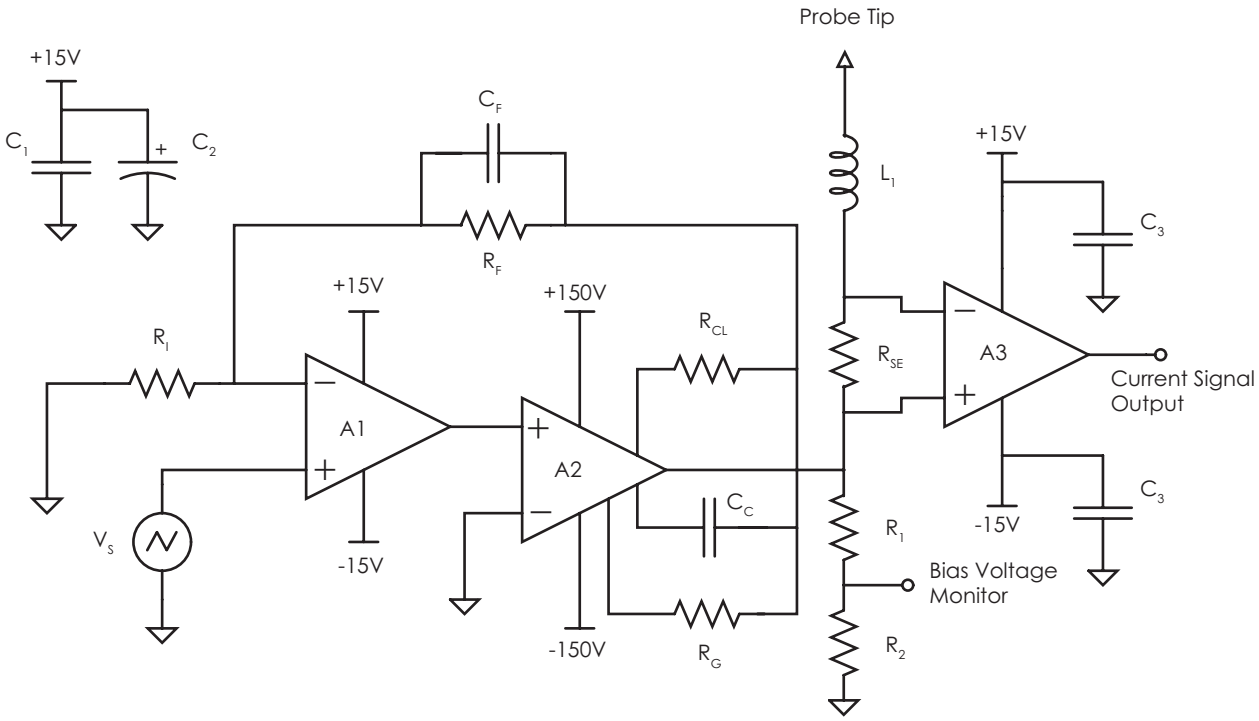

Figure 4-2: Circuit used to drive Mach and Langmuir probes, showing ramp generator V_s, composite amplifier formed by A_1 and A_2, and a single measurement channel formed by difference amplifier A_3 with current measurement resistor R_{SE} and RF choke L_1.

Table 4.1: Components used in the schematic of figure 4.2, with nominal values, tolerances and brief description.

Component	Value	Tolerance (%)	Description
C_1	0.1uF		Ceramic Disc Capacitor
C_2	1uF		Aluminum Electrolytic
A_1			LM741 Operational Amplifier
A_2			Apex PB58 High Voltage Amplifier
R_I	3.3k	± 5	Composite Gain Resistor
R_F	67k	± 5	Composite Gain Resistor
C_F	22pF	± 5	Compensation Capacitor
R_{CL}	1Ω	± 5	Current Limit Resistor
R_G	24k	± 5	PB58 Gain Resistor
C_C	20pF	± 5	PB58 Compensation Capacitor
R_{SE}	51Ω	± 1	Current Sense Resistor
R_1	10k	± 1	Voltage Divider Resistor
R_2	90k	± 1	Voltage Divider Resistor
A_3			AD629 Isolation Amplifier
C_3	0.1uF		Ceramic Disc Capacitor
L_1	10mH		RF Choke
V_S	-5V to $+5$V		Agilent A33000 Waveform Generator

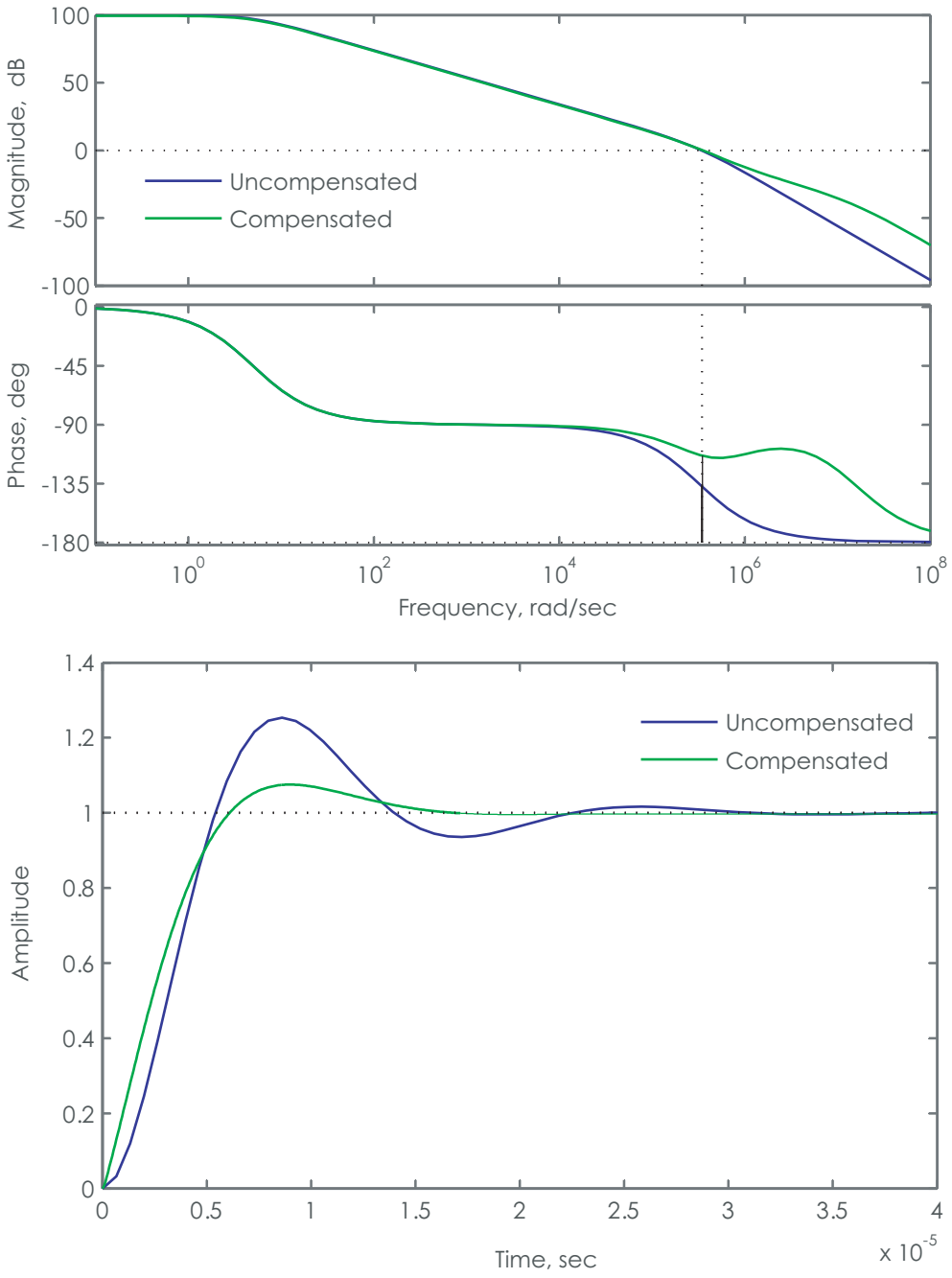

Figure 4-3: Frequency and step response for the composite amplifier of figure 4.2 with and without compensation capacitor C_f.

The use of langmuir probes in RF plasmas can lead to erraneous measurements. The presence of oscillating RF fields mean that the plasma potential and consequently the sheath drop at the probe will have both ac and dc components. Measurements of electron temperature may be distorted in these plasmas if the RF amplitude is large enough to drive the electron current outside of the exponential region[31]; RF effects and compensation should then be considered when q $\phi_{RF} > KT_e$. Compensation then amounts to accounting for RF fluctuations in the sheath, and this may be accomplished in several ways. One method is to add the RF voltage to the probe bias voltage in phase with the RF voltage at the antenna so as to maintain a constant sheath voltage drop at the probe; this method requires additional complexity in probe electronics and one must then not only feed in the RF voltage at the fundamental frequency but at the harmonics (in proprotion) as well. An alternative approach is to use an inductor or an RF choke; the inductor is chosen so that the impedance is large at the RF frequencies of interest and negligible for the frequencies at which the probe bias is swept. This method is viable however the stray capacitance introduced by the sheat itself must be considered. This capacitance may be expressed as[31]

$$C_{sh} = \frac{1}{2^{7/4}} \frac{\epsilon_0 A_{sh}}{\lambda_D} \left[\frac{e(V_s - Vp)}{KT_e} \right]^{-3/4} \tag{4.11}$$

where A_{sh} is the area of the sheath, λ_D the debye length, V_s the sheath voltage, and V_p the plasma potential. At the RF frequency and its harmonics the probe itself will present an output impedance of $Z = 1/\omega C_{sh}$. The inductor must be chosen so that it is much greater than this value at the RF fundamental for the choke to be effective; in this way the portion of the electron current which is induced by the RF voltage is choked while the DC current is allowed to pass. The langmuir probe of the preceding section will have a sheath capacitance of approximately 0.05pF in the presence of a 5eV plasma with a density of order $10^{17}\mathrm{m}^{-3}$, corresponding to an impedance of 255kΩ at $f = 13.56$MHz. The choke by comparison has an impedance of 850kΩ at that frequency. If greater precision in temperature measurement is required, an auxiliary electrode may be used to further enhance the RF compensation[32]. Raw current-voltage characteristics are shown for a compensated and uncompensated (RF choke absent) probe in figure 4.2.

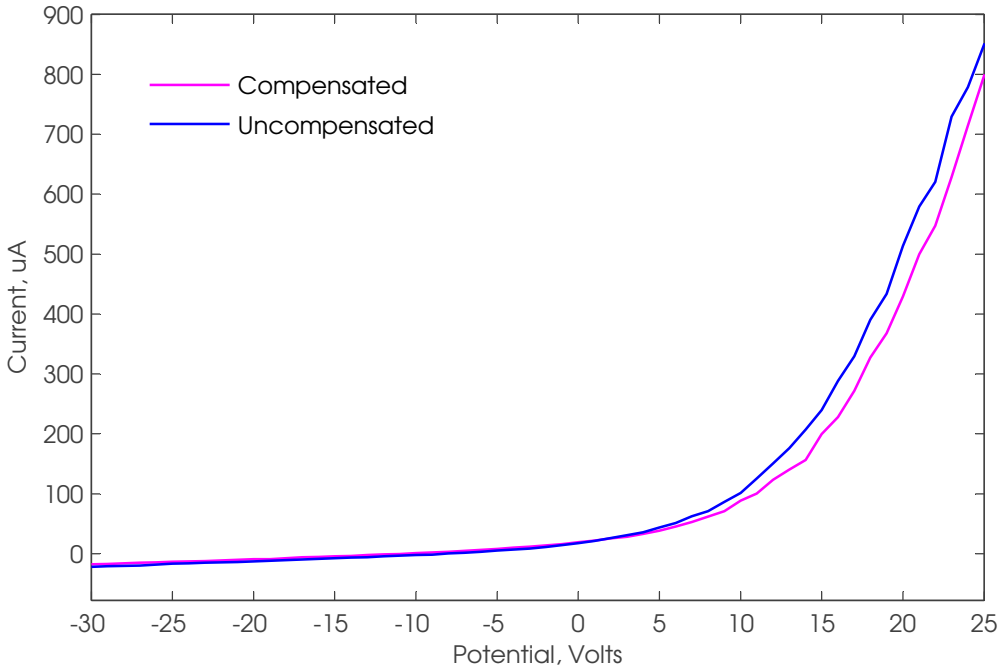

Figure 4-4: I-V characteristics for a typical discharge with parameters $P = 635$W, $B_0 = 1430$G and a gas flow rate of 0.548mg/s of Argon for RF compensated and uncompensated probes.

4.3 Particle Flux Measurements

4.3.1 Temperature and Density

Plasma temperature and density were measured with the use of the aforementioned Langmuir probe. The following sections show the raw, unprocessed current-voltage characteristics obtained in the measurements. The experiments were performed approximately 4.24cm from the exit plane, on the thruster's central axis (at $r = 0$). The power and magnetic field were first held constant at 643W and $B_0 = 1540$G, respectively, while the mass flow rate was varied from 0.237mg/s to 1.37mg/s. In the second series of experiments the flow and the magnetic field were then held constant at 0.548mg/s and $B_0 = 1540$G, respectively, as the power was varied from 550W to 1010W. Data for both experiments are shown below; the temperature for each scan was extracted by fitting the natural log of the exponential portion of the curve to equation 4.9 and then extracting the density from the ion saturation current as prescribed by equation 4.10. Experiments with variation in magnetic field were not conducted as it is difficult to separate magnetic field effects on the probe from field effects on the plasma; this is particularly true for the Mach probe per the preceding discussion of probe theory. The discharge power indicated is the actual coupled power after antenna efficiencies are accounted for.

It is clear from the first set of measurements as illustrated in figure 4-5 that the plasma density increases while the electron temperature decreases as the flow is increased. Futhermore, the plasma density increases linearly with mass flow rate to within experimental error whereas the electron temperature falls more gradually; the dependence of electron temperature seems to vary as the square root of the flow rate, at best. The linear dependence of density with flow rate seems to suggest that all of the propellant gas is ionized or that the ionization fraction either stays constant. The second set of experiments as shown in figure 4-6 are consistent with the energy measurements in that the there seems to be no clear variation of electron temperature with power. The variation of plasma density with power is non-monotonic with no clear form of dependence. Figure **??** summarizes the density and temperature variation with mass flow rate.

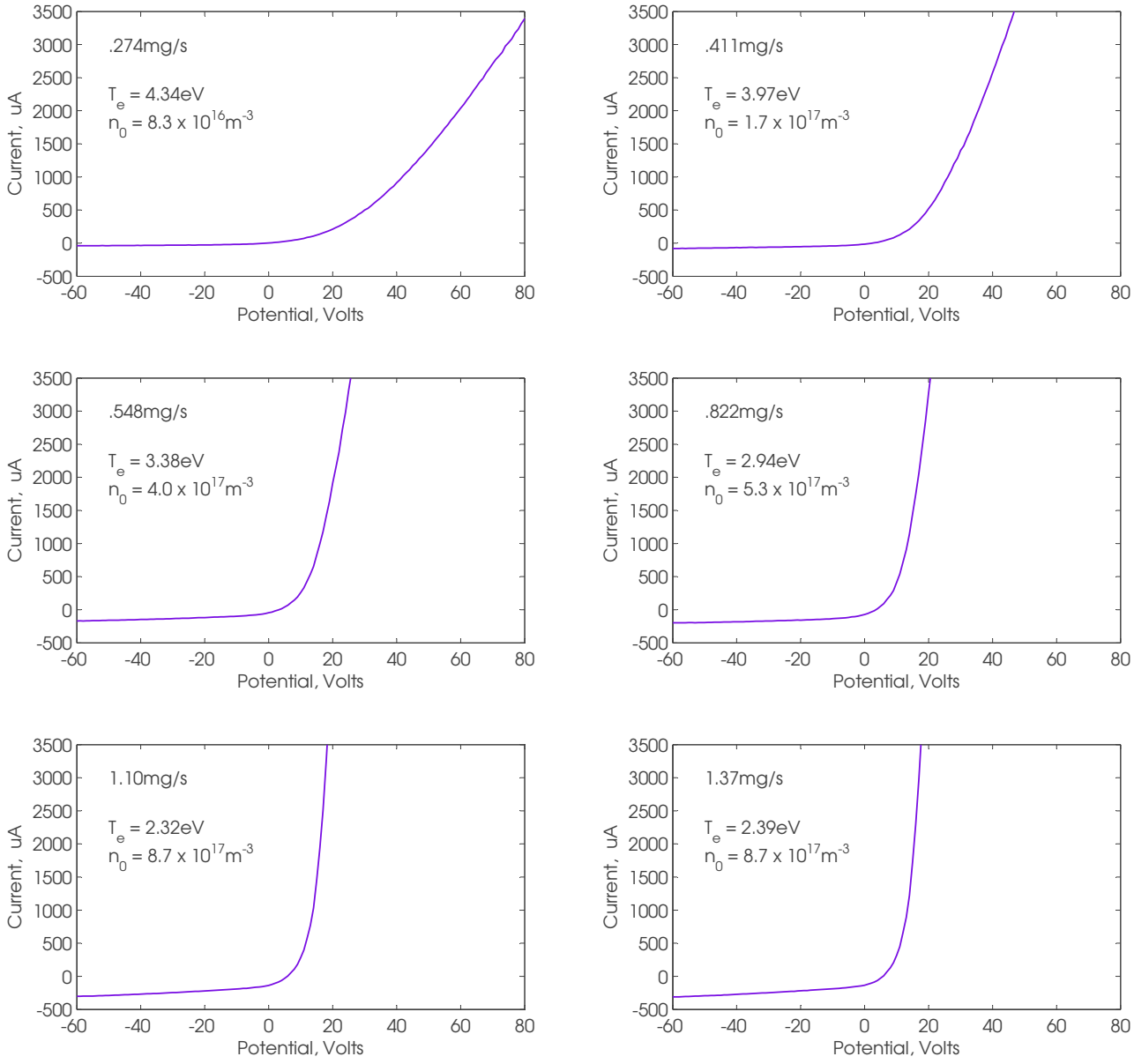

Figure 4-5: Raw I-V curves for $P_0 = 643$Watts, $B_0 = 1540$G and various mass flow rates of Argon as indicated. Plasma temperature extracted from fitting $\ln(I - I_{sat})$ vs. V; density extracted from ion saturation current and c_s.

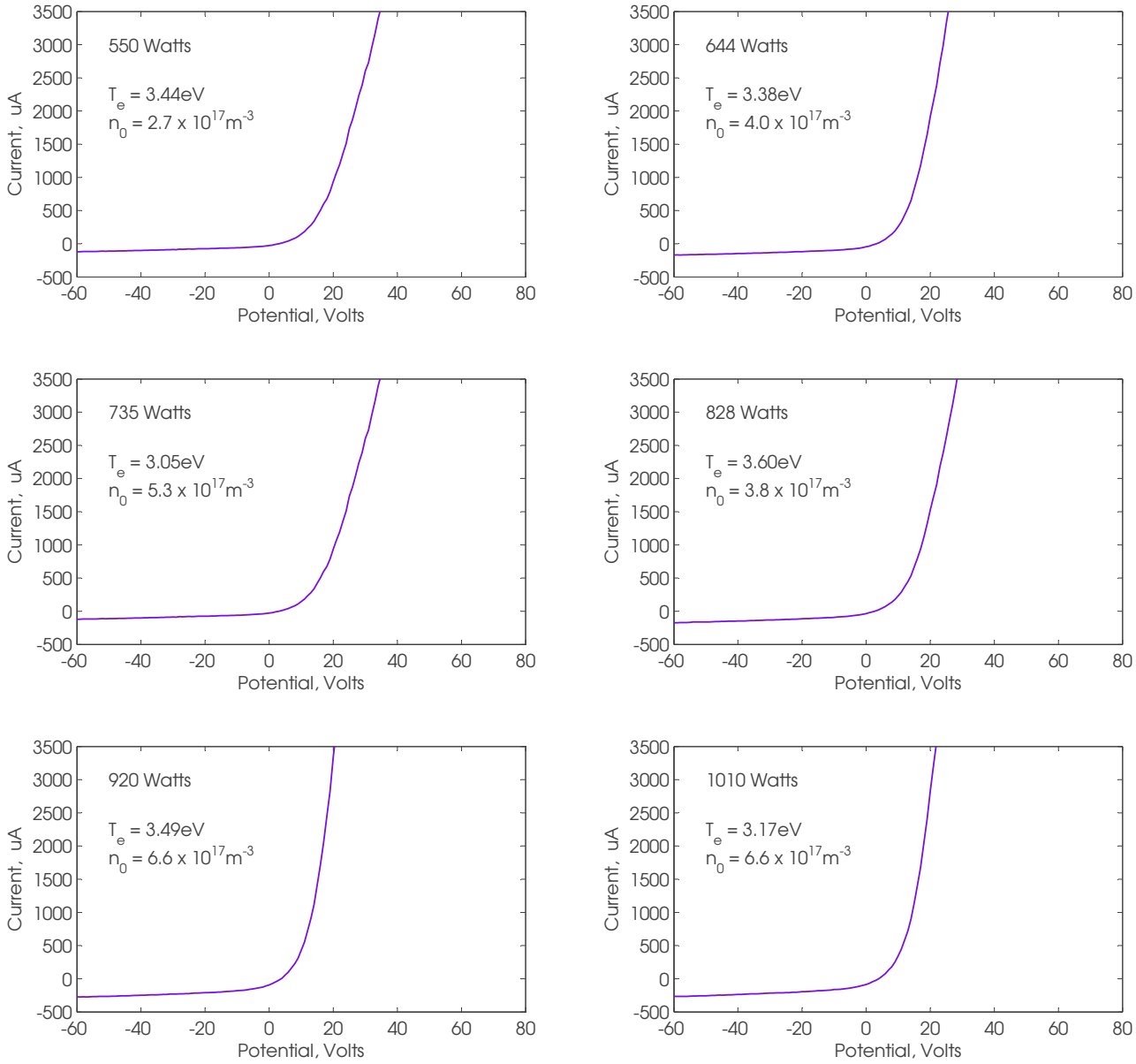

Figure 4-6: Raw I-V curves for various power coupled to plasma. Discharge parameters were $B_0 = 1540$G and a gas flow rate of 0.548mg/s of Argon.

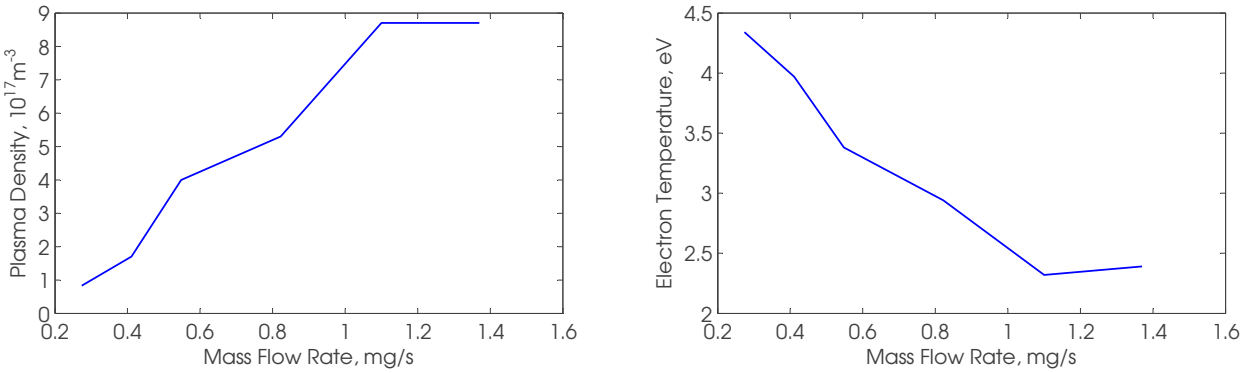

Figure 4-7: Summary of the temperature and density measurements for $P_0 = 635$W, $B_0 = 1540$G as a function of mass flow rates of Argon.

4.3.2 Mach Number and Flow Velocity

The mach number of plasma flows parallel to the magnetic field were measured for a variety of discharge parameters. The probe was placed on axis at a distance of approximately 4.24cm from the exit plane so that the results may be correlated with those of the langmuir probe. The probe was biased into ion saturation at -40V and ion current was separately collected on the upstream and downstream sides of the probe. Statistical errors were reduced by averaging 50 points with timesteps of approximately 200ms in between measurements. The average ratio of the upstream to downstream currents were then corrected for the slight asymmetry in collection area as specified in a preceding section and the Mach number was extracted using equation 4.8 with a calibration constant of $K = 1.9$ for $T_i \approx .2T_e$. Data was again taken by first holding magnetic field constant at $B_0 = 1540$G while the mass flow rate was varied from 0.237mg/s to 1.37mg/s for $P = 643$W and $P = 1010$W. This was followed by a power scan where the flow rate was held constant at 0.548mg/s while the power was varied from 550W to 1010W. Magnetic field scans were again avoided so as to not intertwine probe effects from those of the plasma itself.

The Mach number increases with flow rate, as illustrated by figure 4-8. The mass flow rate scan however is somewhat deceiving; it suggests that the Mach number is higher for greater power. This is likely to be a systematic measurement error since the power scan shows no significant variation in the Mach number. The Mach number measurement was then be combined with the local electron temperature measurement in order to extract the absolute flow velocity; those results

are shown in figure 4-9. These results are qualitatively consistent with the trends found in the energy measurements, namely that the flow velocity (and consquently the mean ion energy) decreased with increasing mass flow rate and that no significant change was observed in the mean ion energy with respect to variations in power. Note however, that the velocities here are considerably smaller than those measured farther downstream with the energy analyzer. The dependence of flow velocity on variations in mass flow rate is linear which implies that the dependence of energy on flow rate quadratic which is again consistent with the energy measurements.

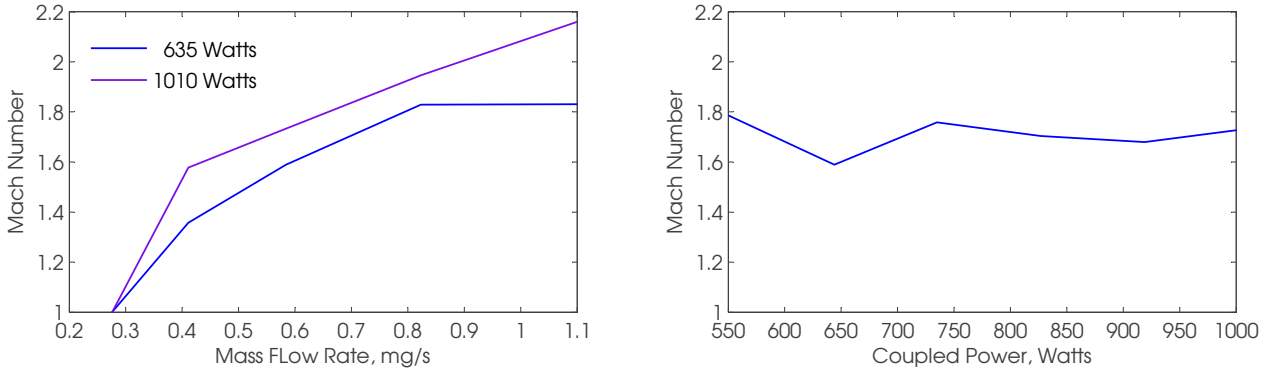

Figure 4-8: Mach number as a function of mass flow rate for $P_0 = 700$W and $P_0 = 1100$W (left). Mach number as a function of power coupled to plasma for $B_0 = 1540$G and a gas flow rate of 0.548mg/s of Argon (right).

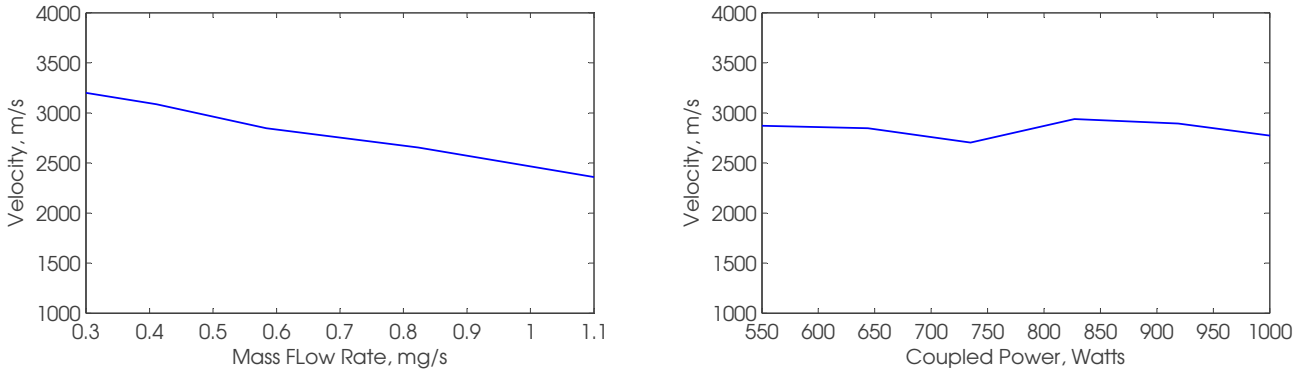

Figure 4-9: Flow velocity as a function of mass flow rate for $P_0 = 635$W and $P_0 = 1010$W (left). Flow velocity as a function of power coupled to plasma for $B_0 = 1540$G and a gas flow rate of 0.548mg/s of Argon (right).

Chapter 5

Conclusion

The plasma parameters measured in the preceding chapters may be used to deduce several of the performance characteristics as discussed in chapter 1. It was shown consistently in both chapters 3 and 4 that plasma parameters are not particularly sensitive to power or magnetic field for the operational regime under consideration with $B_0 > 1000$G and $P_0 > 600$W. Sensitivity to mass flow rate was however demonstrated and the mean ion energies and corresponding specific impulse shown in chapter 3. The remaining performance characteristics such as thrust and ion cost are computed and presented here. Potential ion acceleration mechanisms are briefly discussed as well as recommendations for future research.

5.1 Performance Characteristics

It is of interest to determine thruster performance characteristics for variations in flow, as it was experimentally demonstrated that ions undergo significant acceleration for low mass flow rates. The starting point for this analysis is the axial ion speed or equivalently mean ion energy as determined in chapter 3. This information combined with equation 1.11 allows the determination of thrust as well as the thrust efficiency if the mass flow rate of propellant leaving the thruster $\dot{m}$ is known. The mass flow rate leaving the thruster is just the mass flow rate injected at the gas feed less any wall losses. In an ideal situation one would obtain this information from flux measurements as outlined in the discussion of utilization efficiency in section 1.1. The utilization efficiency may be found from equation 1.9 however determination of the total mass flow out of the thruster as well

as the ionization cost requires knowledge of the plasma radius. This is non-trivial since the gas expansion and the divergence angle of the plasma has been qualitatively seen to change with flow rate and power in addition to magnetic field as one might predict. The approach taken here is to obtain an upper bound by assuming that the ionization fraction and the utilization efficiency are approximately unity. These assumptions are justified by the density measurements of chapter 4 as well as spectral measurements[33]. Referring to figure 4-7, it is seen that the density exhibits a linear dependence on flow rate. This result combined with the depletion of prominent Argon neutral lines in the spectral experiments[33] indicate that nearly all of the gas is ionized and accelerated out; estimates from the latter reference suggest a utilization of 95% or more. With this assumption one may use equation 1.11 to determine the thrust and efficiency from the measurements of specific impulse. Once efficiency is found equation 1.12 may be used to determine the ion cost. The results are computed and illustrated in figure 5-1.

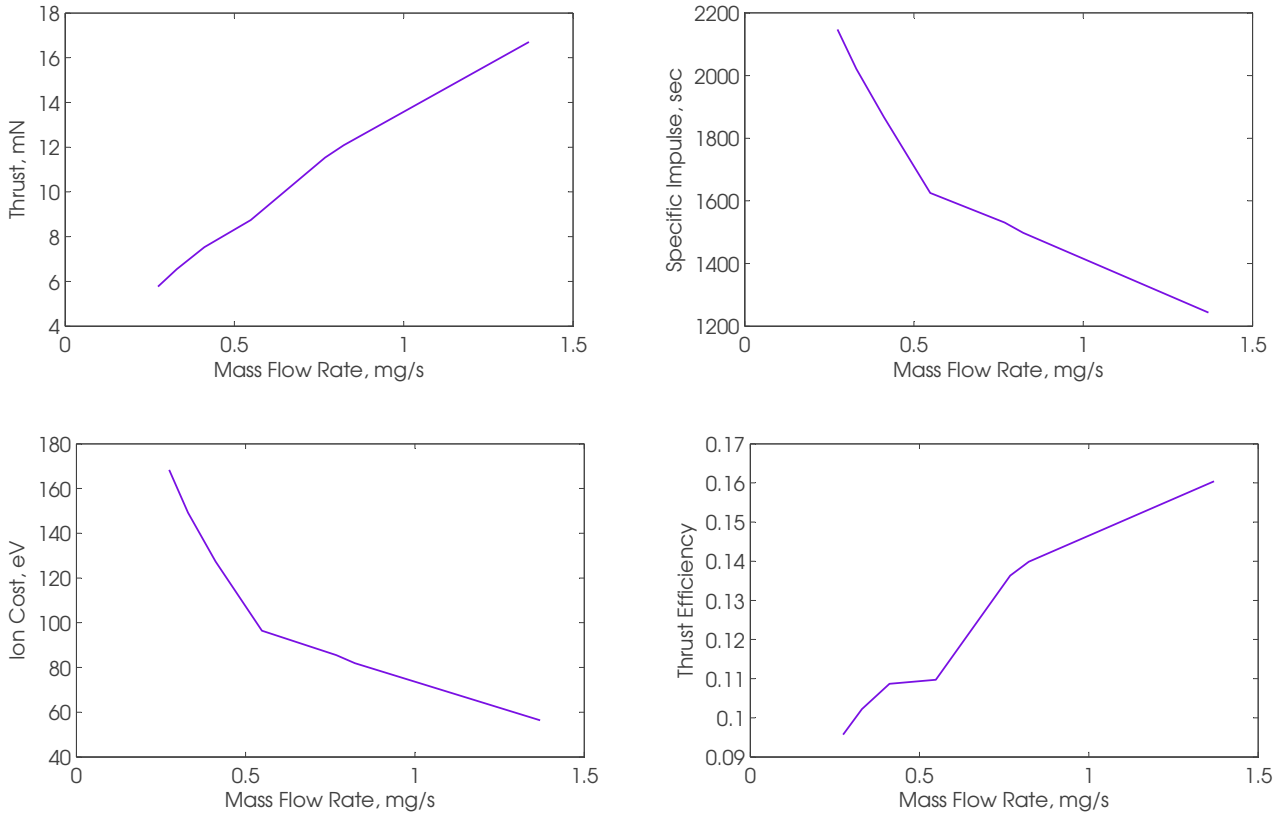

Figure 5-1: Thrust, specific impulse, ion cost and thrust efficiency for $P_0 = 635$W, $B_0 = 1540$G as a function of mass flow rates of Argon.

5.2 Propulsion Mechanisms

The measurement results presented throughout the last chapters illustrate the presence of significant ion acceleration, even after one accounts for a plasma potential of approximately $28 - 30$V. The energy measurements were made far downstream of the thrusters exit plane, where all ion acceleration mechanisms have presumably been accounted for. The flux measurements performed near the exit plane demonstrate that the ion speed there is roughly that which one would expect if the acceleration were due to ambipolar flux alone (this is of order KT_e). The discrepancy then suggests that the majority of the acceleration takes place in the plasma jet after leaving the thruster. The measurements show consistant trends where the velocities are not significantly affected by variations in power or magnetic field but are particularly sensitive in a regime where the mass flow

rate is low. The cause of this effect is not clear, as the extra energy does not contribute to direct electron heating but presumably sets up a potential drop in the plume region which then accelerates ions. Similar observations of this operational regime have been made for another helicon source, however that experiment was physically larger with a lower power density and utilized Helium and Hydrogen propellants[34, 35]. The observed acceleration of ions up to 40km/s in that experiment was explained by electron temperatures as high as 14eV[36], which are not seen in the present work. It is clear from the flux measurements that ambipolar mechanisms alone cannot explain the high ion energies observed downstream in the thruster's plasma jet. Electrons have a temperature of only 5eV (at most) by which ions may be accelerated. Note that the flux measurements were taken where the magnetic field was approximately two-thirds the peak value. The lack of high energy ions in that region confirms the notion that the ion temperature ($T_{i\perp}$) is low and rules out any acceleration mechanism involving adiabatic expansion of the gas. This also rules out the possibility of any initial significant adiabatic compression of the gas during the cycle when neutrals are initially ionized and the plasma compressed by the magnetic field while the helicon wave simultaneously propagates along the thruster's axis.

One possibility previously not considered is the interaction of high-energy electrons near the antenna with the ions in the plume region. Qualitatively, significant ion acceleration tends to coincide in experiments with a visually expansive plume; this occurs only when the thruster is operating in the helicon regime (as opposed to $B_0 = 0$). The local antenna fields drive the electrons axially; their extent penetrates the plasma jet out of the thruster, resulting in a visible plume. Spectroscopic measurements on the thruster have demonstrated excitation of Argon lines with excitation energies upwards 30eV[33], indicating the presence of a fast electron population. Furthermore, the lifetimes of these excited Argon states imply that the excitation is local and that fast electrons are in fact present in the plume region. The population of these fast electrons must however be investigated to determine whether they impose a significant impact on the dynamics in the plume.

The formation of an associated potential drop in the plume due to plasma expansion through the magnetic nozzle is another possibility. It has been proposed that the formation of current free double layers is possible in a plasma expanding through a magnetic field[37], assuming that the electrons have a Maxwellian distribution and that the plasma is frozen along field lines. The ions are first accelerated to the Bohm velocity due to the expansion of the magnetic field, which

occurs when the plasma radius has expanded by 28% or the equivalently the magnetic field fallen by approximately 50%. At this point in space the ion density falls more slowly than the electron density and an ion sheath is formed. Quasineutrality breaks down and this separation of charge can lead to potential drops of approximately $5KT_e$ in Argon plasmas[37]. For the current plasma this would be no more than roughly 25eV based on the measurements of chapter 4. When combined with the energy of ions at the exit plane (found from velocity measurements shown in figure 4-9 yields about 30eV ions which falls considerably short of the ion acceleration measured downstream in chapter 3.

5.3 Recommendations for Future Work

The accuracy of the performance parameters measured here may be improved with flux measurement along the radial direction of the plume. This allows one to deduce the plasma radius and in turn allows for an accurate calculation of utilizatoin efficiency and ion cost; plasma jet collimation is a second order performance parmater which may also be deduced from these measurements.

Ion velocity measurements along the thruster's axis may be taken to bridge the physical gap between the measurements at the thruster's exit plane and those far downstream of the thruster where energy measurements were taken; this will verify that the acceleration does occur in that region and will quantify it as well. That measurement however presents several challenges. The use of Mach probes in this region is troublesome in that the variation of magnetic field introduces an error which is not well characterized. The energy analyzer on the other hand is fragile and easily destroyed if brought near the dense plasma just downstream of the thruster's exit plane.

Once the mechanism for ion acceleration and plasma jet collimation are understood the optimization of thrust and ion cost may be conducted. The variables are the shape of the magnetic field, the relative positioning of the antenna, source diameter and length (within the limit of a compact thruster).

Appendix A

Photographs of Experimental Hardware

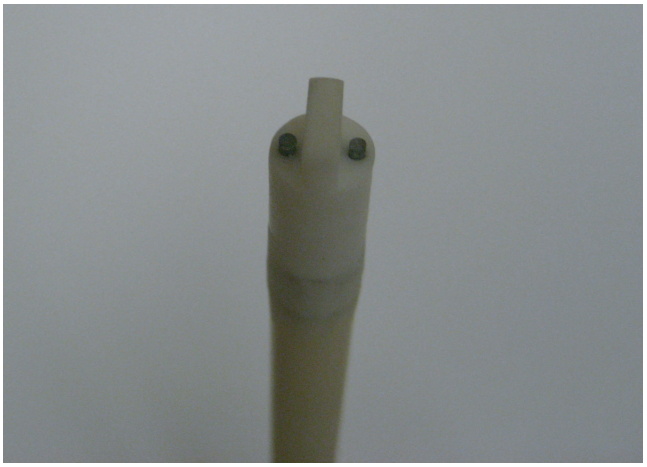

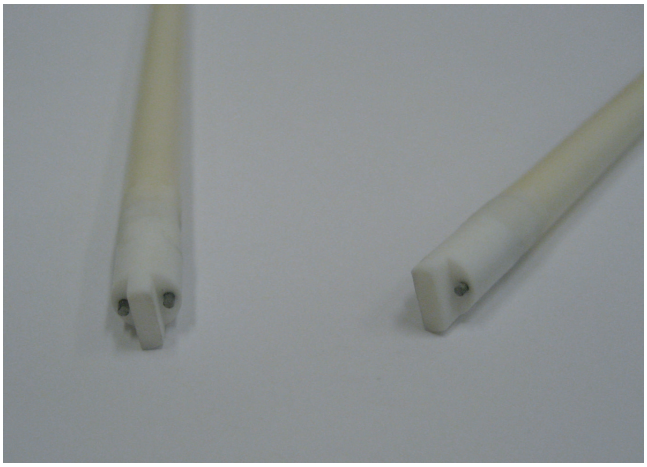

Figure A-1: Mach probes used in the ion flux measurements of chapter 4.

Figure A-2: Retarding potential analyzer used for the ion energy measurements of chapter 3, showing various spacers, grids, stainless steel body and inner sleeve.

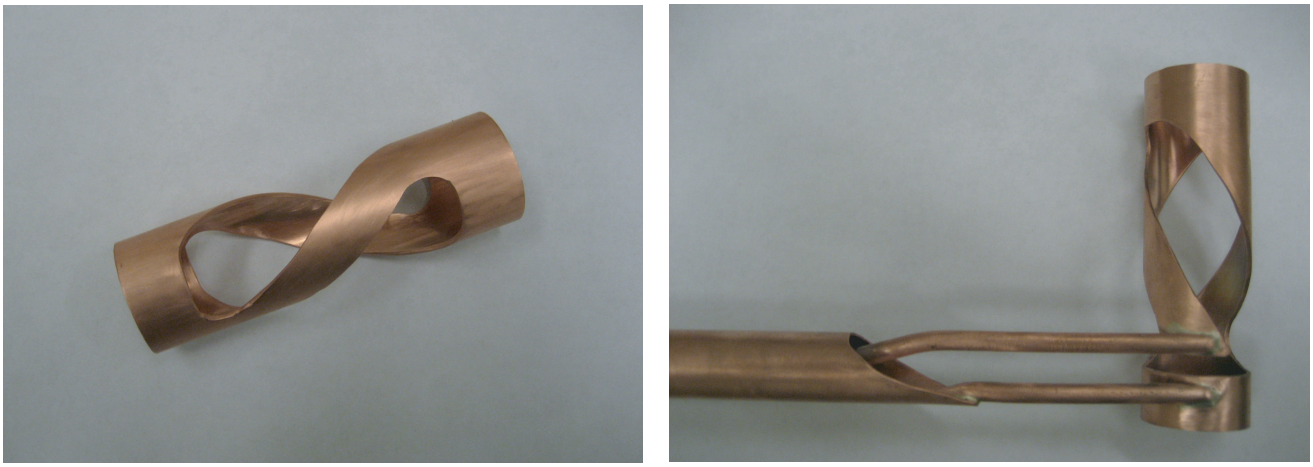

Figure A-3: Right handed half-helical antenna used in experiments. Antenna length is approximately 10cm corresponding to a resonant electron energy of 20eV. Antenna connected to coaxial RF power feed shown on right.

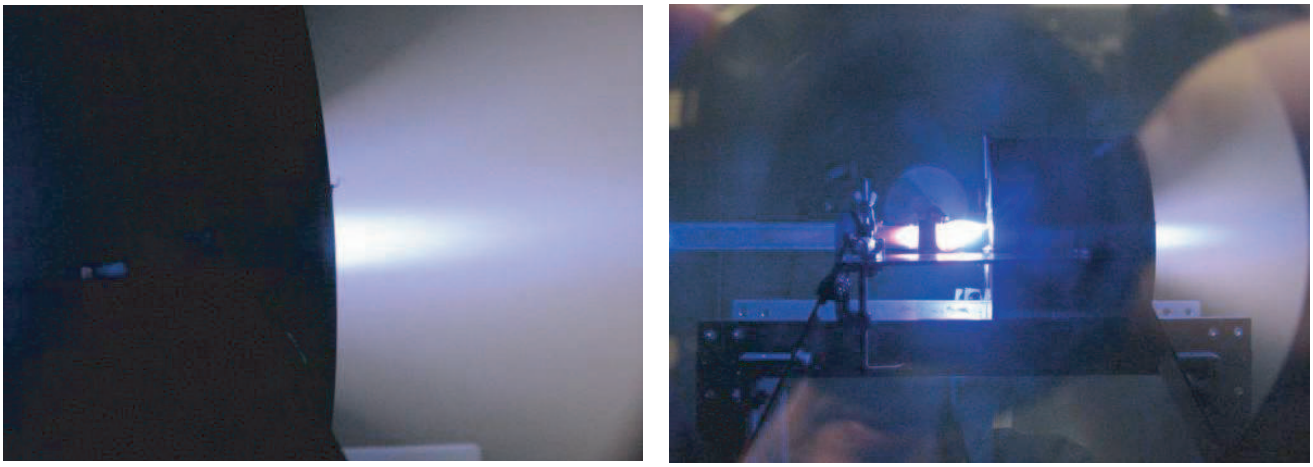

Figure A-4: Thruster in operation with $P_0 = 900$W, $B_0 = 1540$G and a mass flow rate of 0.548mg/s of Argon.

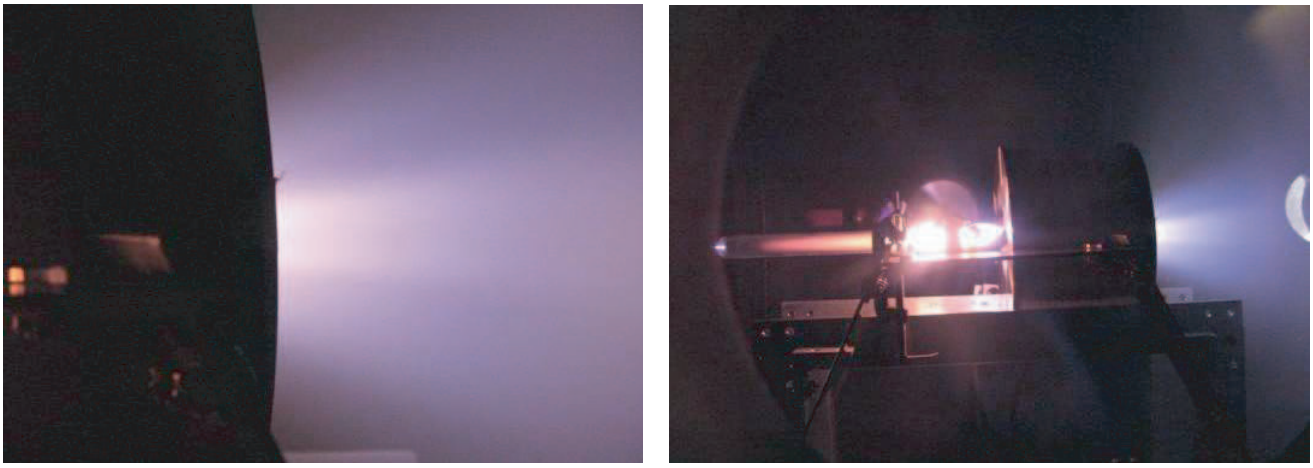

Figure A-5: Thruster in operation with $P_0 = 900$W, $B_0 = 1540$G and a mass flow rate of 0.548mg/s of Nitrogen.

Appendix B

Laboratory Vacuum Environment and Plasma Impurities

A cylindrical (1.6m $\times$1.5 m) magnetic stainless steel chamber is used to simulate the vacuum environment of space for the purposes of thruster laboratory testing. The chamber is equipped with a rotary vane pump and two cryopumps. The rotary vane pump is first used to get to the edge of rough vacuum ($< 1 \times 10^{-3}$ Torr) and the cryopumps are then valved in to bring the chamber down to high vacuum ($< 1 \times 10^{-6}$ Torr). The cryopumps have a combined pumping speed of $7,500$L/sec of Argon, $26,500$L/sec of water vapor and approximately $9,000$L/sec of air. Thermocouple pressure gauges are used to monitor chamber pressure until rough vacuum, and are calibrated once at vacuum and again at atmosphere against internal calibration curves. The use of a cold cathode vacuum gauge is made to monitor chamber pressure under high vacuum conditions. The cold cathode is calibrated for Nitrogen and is generally corrected for the molecular weight of gas used; the gauge is accurate to within 10-20%. A gas correction factor of 1.3 was used for Argon (i.e. the Nitrogen calibrated pressure is scaled down by that factor). Once the chamber reaches high vacuum ($< 1 \times 10^{-4}$ Torr) the walls will begin to outgass; this load consists primarily of the water vapor absorbed in the room. Outgassing rates are difficult to estimate, although they have been characterized for various commonly used materials[38].

Every effort is made to use vacuum compatible materials wherever possible; this will limit excessive loads on the pumping system however more importantly from an experimentalist viewpoint

is critical in maintaining plasma purity. The thruster is less prone to contamination by impurities since pure propellant gas is injected axially at the end and has nozzle pressures slightly larger than that of its ambient. Measurements of chamber pressure against input flow rate were taken immediately after pumpdown and four hours thereafter, as illustrated in figure B-1. The results show that the gas flow rates used for the experiment constitute a greater load than any outgassing from the chamber or the thruster itself; this can be seen by the fact that the loads do not change over the course of several hours. Outgassing rates for water vapor have been have been shown to drop by several factors over the course the time alotted for measurement; the same applies for the outgassing rates of most of the materials used in the experiment (aluminum frames, copper and steel)[38]. It is unlikely for the impurity concentration to be significant in these experiments.

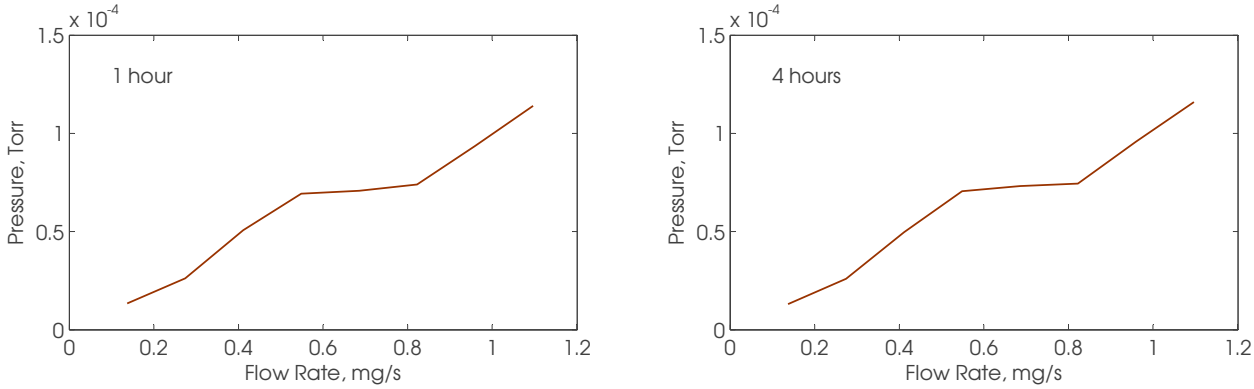

Figure B-1: Vaccum chamber backpressure as a function of Argon mass flow rate one hour and four hours after initial chamber pumpdown.

Appendix C

Thruster Control System

A control system was developed to monitor and control thruster operation, including the mass flow rate of the propellant, the radio-frequency power as well as the magnet current. The following pages illustrate the three main LabVIEW virtual instruments used to control the RF and DC power supplies as well as the mass flow controller.

The RF power supply application allows the user to select the amount of power to be deliverd, monitors the forward and reflected power and calculates the voltage standing wave ratio (VSWR) and network impedance. The magnet control application allows the user to set (or change) the magnet current in real time. The current is ramped by the sepcificed ramp rate. Temperature monitoring and automatic shutdown upon reaching a pre-defined temperature threshold is also supported. The flow application allows the user to select the desired gas and the amount of flow to be delivered. The actual flow rate is monitored in real time. Purge fuctionality is also built in, allowing the user to flush the flow lines for several seconds (useful when switching between different propellants).

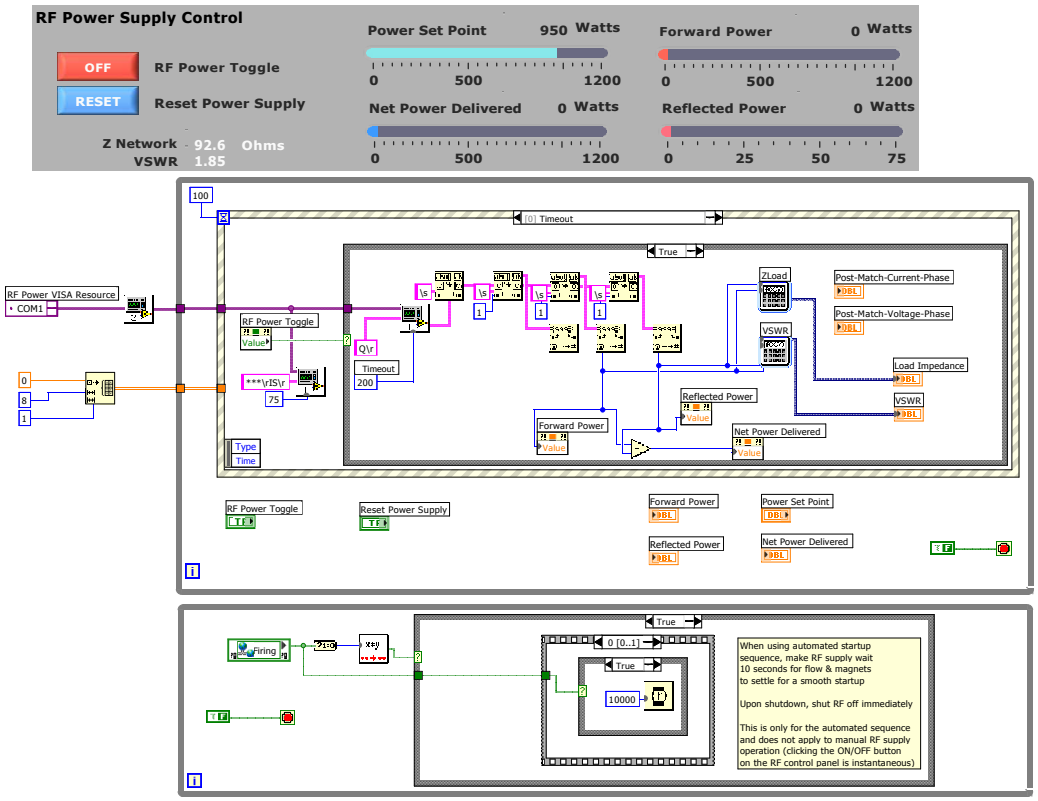

Figure C-1: Radio-frequency power control virtual instrument (VI). The power set point may be chosen while the forward, reflected and net power are acquired and displayed from a directional coupler. The voltage standing wave ratio and the impedance of the matching network and load are calculated and displayed as well.

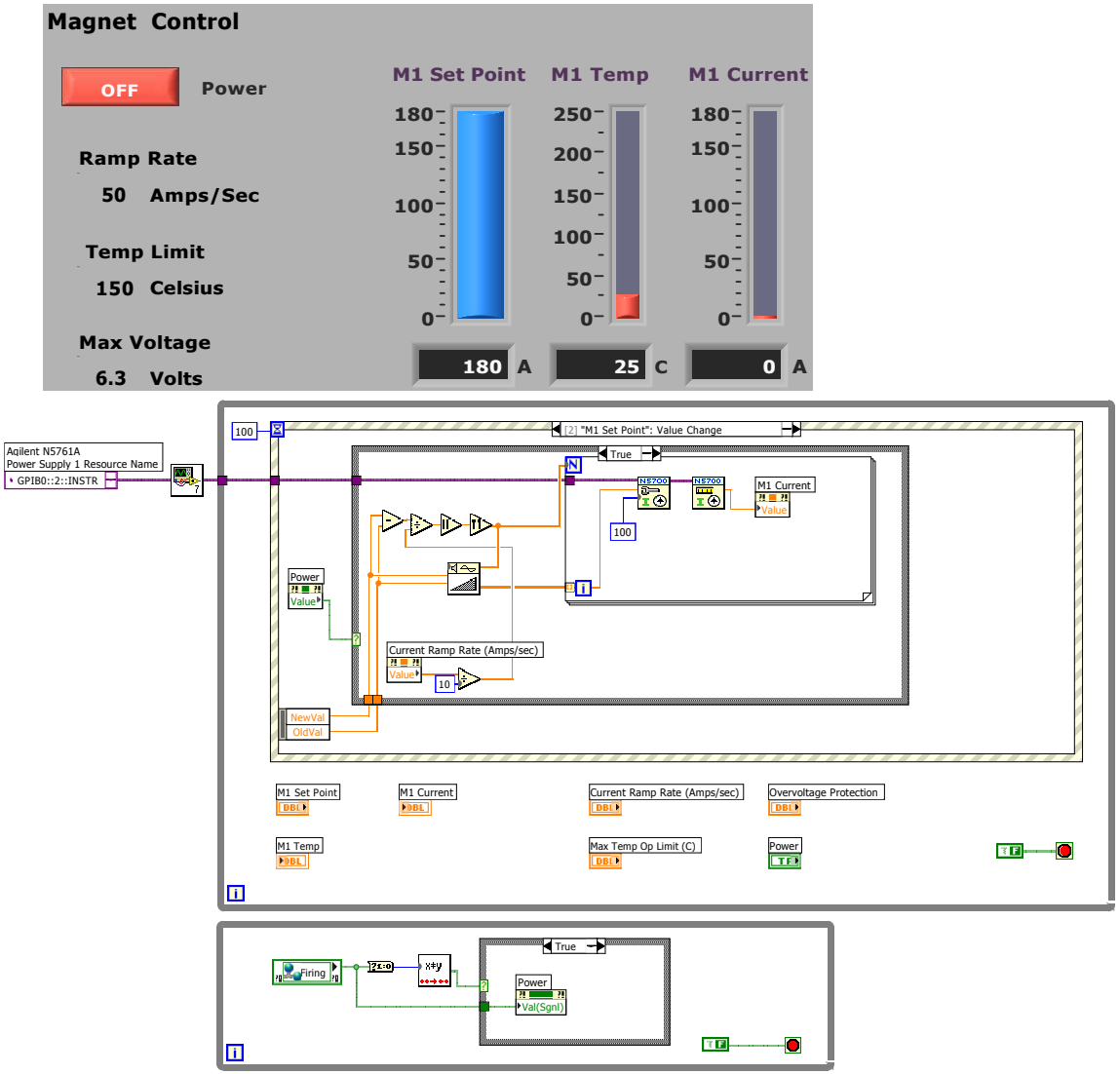

Figure C-2: Magnet power control. The current set point may be chosen (0-180A) while the actual current is acquired and displayed in real time. The ramp rate, overtemperature limit and voltage limits of the power supply may also be selected.

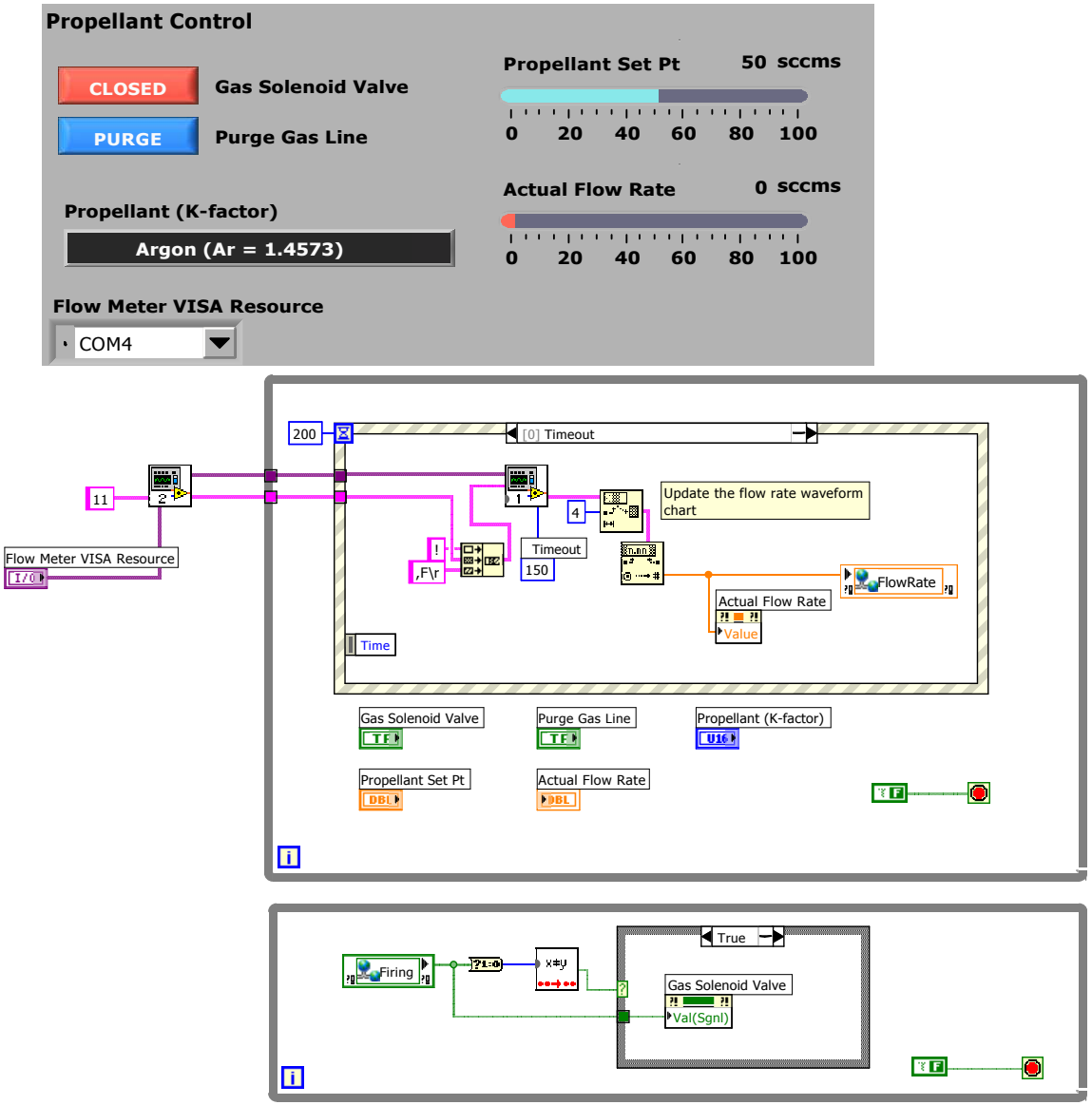

Figure C-3: Propellant flow control. The propellant gas flow may be selected (in standard cubic centimeters per minute, or sccm) while the actual flow rate is monitored in real time. The type of gas used may be specified to apply a correction factor to the flow control.

References

[1] Y. Azziz. *Experimental and Theoretical Characterization of a Hall Thruster Plume*. Phd dissertation, Massachusetts Institute of Technology, Department of Aeronautics and Astronautics, June 2007.

[2] M. Martinez-Sanchez and J. E. Pollard. Spacecraft electric propulsion-an overview. *Journal of Propulsion and Power*, 14(5):688–699, Sep-Oct 1998.

[3] O. A. Popov, editor. *High Density Plasma Sources*. Noyes Publications, Park Ridge, New Jersey, 1995.

[4] G. P. Sutton and O. Biblarz. *Rocket Propulsion Elements*. John Wiley & Sons, Inc, New York, seventh edition, 2001.

[5] F. F. Chen and D. Arnush. Generalized theory of helicon waves. i. normal modes. *Physics of Plasmas*, 4(9):3411–3421, September 1997.

[6] F. F. Chen and D. Arnush. Generalized theory of helicon waves. ii. excitation and absorption. *Physics of Plasmas*, 5(5):1239–1254, May 1997.

[7] F. F. Chen. Plasma ionization by helicon waves. *Physics of Plasmas and Controlled Fusion*, 33(4):339–364, November 1991.

[8] M. Light and F. F. Chen. Helicon wave excitation with helical antennas. *Physics of Plasmas*, 2(4):1084–1093, April 1995.

[9] R. W. Boswell. Very efficient plasma generation by whistler waves near the lower hybrid frequency. *Plasma Physics and Controlled Fusion*, 26(10):1147–1162, February 1984.

[10] F. F. Chen and D. D. Blackwell. Upper limit to landau damping in helicon discharges. *Phys. Rev. Letters*, 82(13):2677–2680, March 1999.

[11] V. Kaeppelin et al. Different operational regimes in a helicon plasma source. *Review of Scientific Instruments*, 72(12):4377–4382, December 2001.

[12] J. P. Klozenberg et al. The dispersion and attenuation of helicon waves in a unifrom cylindrical plasma. *J. Fluid Mech.*, 21(3):545–563, July 1965.

[13] D. Arnush. The role of trivelpiece-gould waves in antenna coupling to helicon waves. *Physics of Plasmas*, 7(7):3042–3050, July 2000.

[14] M. Light, F. F. Chen, and P. L. Colestock. Quiescent and unstable regimes of a helicon plasma. *Plasma Sources Science and Technology*, 11:273–278, June 2002.

[15] Y. Sakawa, N. Koshikawa, and T. Shoji. Characteristics of the high density plasma production by m=0 helicon wave. *Appl. Phys. Lett*, 69(12):1695–1697, September 1996.

[16] D. Miljak and F. F. Chen. Helicon wave excitation with rotating antenna fields. *Plasma Sources Sci. Technology*, 7:61–74, July 1997.

[17] A. V. Arefiev and B. N. Breizman. Magnetohydrodynamic scenario of plasma detachment in a magnetic nozzle. *Physics of Plasmas*, (12):043504–1 – 043504–10, March 2005.

[18] E. E. Scime et al. Control of ion temperature anisotropy in a helicon plasma. *Plasma Sources Sci. Technol.*, (7):186–191, March 1998.

[19] F. F. Chen. *Introduction to Plasma Physics and Controlled Fusion*, volume 1. Plenum Press, New York, N.Y., second edition edition, 1984.

[20] N. Sinenian, O. Batischev, and M. Martinez-Sanchez. Plasma flow characterization of a mini-helicon thruster. In *49th Annual Meeting of the Division of Plasma Physics*, Orlando, Florida, November 2007. American Physical Society.

[21] O. Batischev, N. Sinenian, M. Celik, and M. Martinez-Sanchez. Results from the mini-helicon thruster experiment. In *49th Annual Meeting of the Division of Plasma Physics*, Orlando, Florida, November 2007. American Physical Society.

[22] O. Batishchev, J. Pucci, N. Sinenian, Z. LaBry, M. Celik, and M. Martinez-Sanchez. Mini-helicon thruster experiment at mit. In *48th Annual Meeting of the Division of Plasma Physics*, Philadelphia, Pennsylvania, November 2006. American Physical Society.

[23] O. Batishchev, N. Sinenian, M. Celik, and M. Martinez-Sanchez. Development of the mini-helicon thruster at mit. In *30th International Electric Propulsion Conference*, Florence, Italy, September 2007.

[24] J. M. Pucci, N. Sinenian, J. Palaia, M. Celik, Z. LaBry, A. Shabshelowitz, O. Batishchev, and M. Martinez-Sanchez. Preliminary characterization of a helicon plasma source for space propulsion. In *42nd AIAA/ASME/SAE/ASEE Joint Propulsion Conference & Exhibit*, Sacramento, California, July 2006.

[25] D. M. Pozar. *Microwave Engineering*. John Wiley & Sons, Inc., Park Ridge, New Jersey, third edition edition, 2005.

[26] I. H. Hutchinson. *Principles of Plasma Diagnostics*. Cambridge University Press, New York, second edition, 2005.

[27] I. H. Hutchinson. Ion collection by probes in strong magnetic fields with plasma flow. *Physical Review A*, 37(11):4358–4366, June 1988.

[28] J.P. Gunn et al. Edge flow measurements with gundestrup probes. *Physics of Plasmas*, 8(5), May 2001.

[29] K. S. Chung and I. H. Hutchinson. Kinetic theory of ion collection by probing objects in flowing strongly magnetized plasmas. *Physical Review A*, 38(9):4721–4731, March 1988.

[30] L. Oksuz and N. Hershkowitz. Understanding mach probes and langmuir probes in a drifting, unmagnetized, non-uniform plasma. *Plasma Sources Sci. Technol.*, 13:263–271, April 2004.

[31] I. D. Sudit and F. F. Chen. Rf compensated probes for high-density discharges. *Plasma Sources Sci. Technol.*, 3:162–168, November 1993.

[32] F. F. Chen. Lecture notes on langmuir probe diagnostics. Mini-Course on Plasma Diagnostics, IEEE-ICOPS Meeting, Jeju, Korea, June 2003.

[33] M. Celik. *Experimental and Computational Studies of Electric Thruster Plasma Radiation Emission*. Phd dissertation, Massachusetts Institute of Technology, Department of Aeronautics and Astronautics, May 2007.

[34] O. Batishchev and K. Molvig. Vasimr thruster operation with hydrogen and helium gas propellants. In *28th International Electric Propulsion Conference*, Toulouse, France, March 2003.

[35] O. Batishchev and K. Molvig. Numerical study of plasma production in the vasimr thruster. In *27th International Electric Propulsion Conference*, Pasadena, California, October 2001.

[36] O. Batishchev et al. Study of gas burn-out regime in the vasimr helicon plasma source. In *30th EPS Conference on Controlled Fusion and Plasma Physics*, St. Petersburg, Russia, July 2003.

[37] F. F. Chen. Physical mechanism of current-free double layers. *Physics of Plasmas*, 13:034502–1:3, March 2006.

[38] E. D. Erikson et al. Vacuum outgassing of various materials. *J. Vac. Sci. Technol.*, 2(2):206–210, January 1984.